Stability and Control of Grid-Friendly PV Systems

Peng, Qiao

Publication date:
2020

Document Version
Publisher's PDF, also known as Version of record

STABILITY AND CONTROL OF GRID-FRIENDLY PV SYSTEMS

BY
QIAO PENG

DISSERTATION SUBMITTED 2020

AALBORG UNIVERSITY
DENMARK

Stability and Control of Grid-Friendly PV Systems

Ph.D. Dissertation

Qiao Peng

Dissertation submitted October 12, 2020

Dissertation submitted: October 12, 2020

PhD supervisors: Assoc. Prof. Yongheng Yang
Aalborg University

Prof. Frede Blaabjerg
Aalborg University

Prof. Huai Wang
Aalborg University

PhD committee: Associate Professor Amjad Anvari-Moghaddam (chair)
Aalborg University

Professor Gabriela Hug-Glanzmann
Swiss Federal Institute of Tecnology (ETH)

Lecturer, Head of Department Martin Hill
Cork Institute of Technology (CIT)

PhD Series: Faculty of Engineering and Science, Aalborg University

Department: Faculty of Engineering and Science, Aalborg University

ISSN (online): 2446-1636
ISBN (online): 978-87-7210-825-4

Published by:
Aalborg University Press
Kroghstræde 3
DK – 9220 Aalborg Ø
Phone: +45 99407140
aauf@forlag.aau.dk
forlag.aau.dk

Printed in Denmark by Rosendahls, 2020

Abstract

To develop a more environment-friendly power grid, the traditional fossil fuel is being replaced by renewable energy sources, e.g., wind farms and solar photovoltaic (PV) systems. To integrate renewable energy into the power grid, more and more power electronics are demanded than ever before. It makes the power grid more flexible and controllable. However, it also brings challenges to the modern power grid. One of the crucial challenges is the frequency instability due to the reduction of mechanical inertia, which is conventionally provided by the rotors of synchronous generators (SG). When the SGs are replaced by renewable energy sources, the alternative inertia should be provided. Otherwise, the normal operation of SGs will be challenged, which further threatens the stability of the entire power grid. To deal with this issue, inertia characteristic analysis and inertia enhancement strategy should be addressed. The former requires a general analysis tool for various power generating units in the grid, while the latter demands flexible control of power converters and renewable energy sources.

For the stability evaluation as well as the inertia characteristic analysis, a universal modeling of power converters is proposed in this project. The main concept is to model the power converters with the same external interfaces, i.e., the power exchanged with the grid and the internal voltage, referring to as the power-internal voltage (PIV) characteristic. The PIV model is in analogy to the model of SGs, which can thus reflect the inertia characteristics of power converters, and then, the inertia analysis can be realized. Additionally, the PIV model is obtained in open-loop, which is independent of grid parameters. In this way, the model becomes more general and applicable for the grids consisting of multiple power converters. The proposed model is validated by simulations, and it is verified to be effective for stability analysis.

Besides the inertia characteristic analysis, the effective inertia enhancement strategy is required as well. The virtual inertia provision from DC-link capacitors is proven to be a viable and general solution for this issue. However, the proper design of the virtual inertia control (VIC) of DC-link capacitors with adequately considering the system stability has been rarely discussed. Aiming at this, the maximum virtual inertia analysis method is

proposed in this project. The foundation of the method is the multi-timescale PIV model, which is constructed by several submodels at different timescales. First, the system stability at concerned timescale is investigated based on the submodel at the corresponding timescale, where the VIC of DC-link capacitors can be properly designed. Then, the effective virtual inertia is identified in the submodel at the rotor motion timescale (RMT), which can effectively regulate the frequency as the SG rotors do. The simulation and experimental results show that the proposed method can identify the maximum virtual inertia that ensures system stability.

Notably, more vigorous inertia provision is demanded to help the power grid ride through severe incidents. In this case, the inertia emulation of PV systems requires exploration. The challenge is that the conventional maximum power point tracking (MPPT) strategy cannot ensure full-range frequency regulation, as the PV system is unable to release much power when the grid requires. The cost-effective solution is to reserve a certain amount of PV power in advance. Accordingly, a cost-effective and computation-efficient power reserve control (PRC) of PV systems is developed in this project. It executes the MPPT algorithm periodically to measure the real-time maximum available power (MAP), and then the power reserve reference can be determined accurately. A transient power impulse damping control (TPDC) is designed to buffer the transient power generated by the MPPT execution. Then, the PV output power to the grid is smoothed. Based on the PRC, the VIC of PV systems is achieved, where an event-triggering signal is designed to organize the control loops. The simulation results show that the proposed PRC can effectively achieve power reserve for PV systems, and the grid frequency can be adequately supported by the PRC-based VIC.

Apart from the inertia emulation, the frequency damping control (FDC) of PV systems is also explored in this project. The coordination strategy of VIC and FDC of PV systems is developed to adaptively employ the power reserve for optimal frequency support. The impacts of inertia and damping on frequency dynamic are analyzed at first. Then, considering the grid codes on frequency quality, the grid requirements on the VIC and FDC are obtained. Specifically, the large inertia is required at the early stage of the frequency incident to reduce the rate of change of frequency (RoCoF). Then, the large damping is desired to decrease the frequency deviation. The VIC and FDC coordination strategy of PV systems is designed accordingly. Comparison of different frequency regulation strategies of PV systems is carried out. The simulation results reveal that the proposed strategy can optimally utilize the power reserve, which performs effectively in supporting the grid frequency.

Danske Resumé

For at udvikle et mere miljø-venligt elnet erstattes de traditionelle fossile brændsler af vedvarende energikilder, f.eks. vindmølleparker og solcelleanlæg. For at integrere vedvarende energi i elnettet kræves der langt mere effektelektronik. Dette gør elnettet mere fleksibelt og kontrollerbart. Imidlertid giver det også udfordringer til moderne elnet. En af de afgørende udfordringer er frekvens-ustabilitet på grund af reduktionen af den mekanisk inerti, som traditionelt leveres af rotorerne i synkrongeneratorerne (SG). Når SG erstattes af vedvarende energikilder, bør alternativ inerti tilvejebringes til elnettet, idet ellers vil den normale drift af SG'er blive udfordret og dette kan true stabiliteten af hele elnettet. For at håndtere dette problem skal der udvikles nye strategier til forbedring af inerti forholdene, hvilket kræver et generelt analyseværktøj med forskellige effektelektroniske enheder tilsluttet elnettet, samt en fleksibel styring af effektomformerne i samspil med de vedvarende energikilder.

Til at vurdere stabilitet og nye inerti-løsninger foreslås en universel modellering af effektomformerne i dette projekt. Hovedkonceptet er at modellere effektomformerne til at have de samme eksterne grænseflader til elnettet, dvs. den effekt, der udveksles med nettet og den interne spænding i omformeren, som også henvises til at være PIV-karakteristikken. PIV-modellen er analog med modellen af en SG, som derved kan afspejle inertikarakteristika for effektomformerne, og derefter kan en analyse af systemets inerti realiseres. Derudover opnås PIV-modellen i åben sløjfe, som er uafhængig af elnet parametrene. På den måde bliver modellen mere generel og anvendelig for de elnet, der består af flere effektomformere. Den foreslåede model er valideret ved simuleringer, og den er vurderet til at være effektiv til også at udføre stabilitetsanalyser.

Udover den inerti-karakteristiske analyse kræves også effektive inertiforbedringer til at opnå et stabilt net. Den virtuelle inerti bestemmes af DC-link kondensatorerne i effektomformerne og en foreslået løsning viser sig at være farbar og generel anvendelig for dette problem. Til at gøre dette foreslås en maksimal virtuel inerti-analysemetode. Grundlaget for metoden er, at PIV-modellen har flere tidsskalaer, som er modelleret af flere sub-

modeller dækkende flere tidsskalaer. For det første undersøges systemstabiliteten ved den tidsskala, som er baseret på sub-modellen for den tidsskala, hvor VIC for DC-link-kondensatorer kan designes korrekt. Derefter identificeres den effektive virtuelle inerti i sub-modellen ved brug af rotorens tidsskala (RMT), som effektivt kan regulere frekvensen, ligesom SG-rotorerne gør. Simuleringer og eksperimentelle resultater viser, at den foreslåede metode kan identificere den maksimale virtuelle inerti, som kan være med til at sikre systemstabilitet.

Der kræves især et stort inerti for at hjælpe elnettet med at håndtere alvorlige hændelser og i projektet foretages inerti-emulering ved brug af solcelleanlæg. Udfordringen er, at den konventionelle MPPT-strategi (maximum power point tracking) i solcelle-anlæggene ikke altid kan sikre frekvensregulering, da PV-systemet ikke altid er i stand til at frigive så meget effekt, når el-nettet kræver det. En omkostningseffektiv løsning er at reservere en vis mængde PV-effekt på forhånd, som derfor altid er til rådighed. Der er udviklet i dette projekt en omkostningseffektiv og beregningseffektiv effektreserve kontrol-metode (PRC) til brug i solcelleanlæg. Den udfører MPPT-algoritmen med jævne mellemrum for at måle den reelle maksimale tilgængelige effekt (MAP), og derefter kan den ønskede effektreserve bestemmes. En dynamisk dæmpning af en derved opstået effekt impuls (TPDC) er udviklet til at lagre den ekstra effekt genereret af MPPT-algoritmen. Derfor udjævnes PV-udgangseffekten til el-nettet. Baseret på PRC opnås en VIC for PV-systemet, hvor et hændelses afhængigt signal er valgt til at aktivere kontrolsløjferne i styringen. Simuleringsresultaterne viser, at den foreslåede metode effektivt kan opnå en effektreserve til solcelleanlæggene, og net-frekvensen kan derfor understøttes tilstrækkeligt af den foreslåede PRC-baserede VIC.

Udover inerti-emuleringen undersøges også en frekvensdæmpningskontrol (FDC) udført af solcelleanlæggene. Koordinering af VIC og FDC for PV-systemerne udviklet ved adaptivt at anvende effektreserven til en optimal frekvensunderstøttelse. Virkningen på inerti og dæmpning af frekvensdynamikken er analyseret først. Derefter tages net-kravene til VIC og FDC i betragtning for at kunne opnå frekvenskvalitet. Specifikt kræves en stor inerti i det tidlige stadium af en frekvensforstyrrelse for at kunne reducere ændringen af frekvensen (RoCoF). En store dæmpning ønskes for at mindske frekvensafvigelsen. En VIC- og FDC-koordineringsstrategi for solcelleanlæg er designet i overensstemmelse hermed. Der er også udført en sammenligning af forskellige frekvensreguleringsstrategier for solcelleanlæg. Simuleringsresultaterne viser, at den foreslåede strategi kan udnytte effektreserven optimalt, og fungere effektivt til at understøtte netfrekvensen.

Contents

Preface

This dissertation is the summary of the Ph.D project "*Stability and Control of Grid-Friendly PV Systems*". This project is mainly supported by the Department of Energy Technology, Aalborg University, and the Chinese Scholarship Council. Moreover, some work was supported by THE VELUX FOUNDATIONS – REPEPS (No.: 00016591) and some conference participation was funded by Otto Mønsteds Fond, Denmark. I would like to thank the institutions for their supports.

First and foremost, I would like to give my sincere gratefulness to my supervisor, Assoc. Prof. Yongheng Yang, for his guidance and advice during my Ph.D. project. His encouragement and supports help me a lot. The guidance from my co-supervisors, Prof. Frede Blaabjerg and Prof. Huai Wang, is also of great importance for me during the study. I am very proud of being your student and working in our group.

I would like to extend my gratitude to Prof. Tianqi Liu and Dr. Jingyang Fang for the friendly cooperation and their kind advice to my work. I am also grateful to Dr. Zhongting Tang, Wenjie Liu, Xinrong Huang, Dr. Zhan Shen, Kamran Ali Khan Niazi, Jing Yuan, Assoc. Prof. Tamás Kerekes, Prof. Claus Leth Bak, Dr. Ariya Sangwongwanich, and all my lovely colleagues at the Department of Energy Technology, Aalborg University for their help.

Thanks to Kewei Liu, Jingyu He, and all my friends who are always believing in me. Special gratitude to Zixin Gao for the companion and encouragement during the writing of this thesis. Last but not least, my deepest gratitude to my family, especially my mother, for the exceptional love. This Ph.D. project cannot be done without them.

2020 is special. Please allow me to dedicate this dissertation to everyone who is living the life with bravery and toughness.

Qiao Peng
October 12, 2020

Report

Chapter 1

Introduction

1.1 Background and Motivation

Due to the shortage of fossil fuels, the sustainability of the environment, and also the declining cost, the energy system is being retrofitted across the globe, where renewable energy is much more demanded than ever before [1]. In this context, the electricity network is also hybridized by more renewable energy sources (RES), e.g., solar photovoltaic (PV), wind power, etc. By 2018, the renewable energy share in power generation is more than 25%, and is estimated to increase to 86% by 2050 [2]. To integrate the RESs into the power grid, power electronics converters are necessary and widely used [3, 4]. Consequently, the modern power grid is becoming more complicated than the conventional synchronous generators (SG)-based one with a high penetration of power electronics. The possible power grid with more RESs and power converters is shown in Fig. 1.1.

With the continuous installation of power electronics to cater for more renewable energy, the future power grid will be more efficient to some extent, as the power distribution can be flexibly regulated by the power converters. Additionally, asynchronous AC power grids can be connected by DC grids, where the power converters are the AC/DC interfaces. However, it also brings new challenges to the power grid, e.g., the intermittency in the solar and wind-based power generation, the coordination among power converters [5], and converter impedance interaction protection system design [4]. Besides, the frequency and voltage stability, especially the former, is also challenged, which is the foundation of the conventional power grids.

This can be explained in the following. The conventional power grid is formed by SGs. The frequency is governed by the SG rotors, of which the rotational speed determines the frequency of the SG output current [6]. Furthermore, the rotational speed varies according to the imbalance power

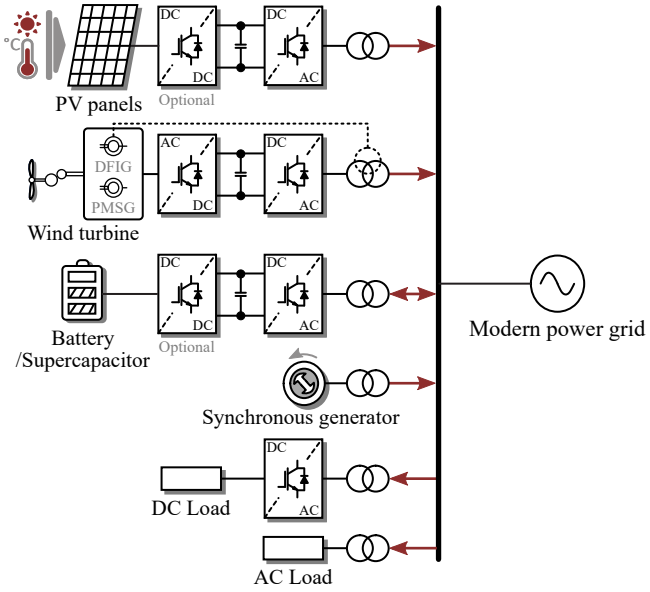

Fig. 1.1: Modern power grid with more RESs, where many power converters (DC-DC, DC-AC, AC-DC) are used.

through the SG. When the SG rotor suffers from a torque imbalance (caused by power imbalance), the rotor inertia and damping resist the change of the rotor motion state. That is, the kinetic energy stored in the rotor is applied to damp the impact from the power imbalance and make the rotor shift to a new motion state. The motion equation of the SG rotors is referred to as the swing equation, where the inherent inertia and damping are key for the power-frequency dynamic. Then, in the SG-based power grid, the inertia and damping of the SGs determine the grid frequency dynamic and further affect the rule-making of the operation, control, and protection of the entire power grid [7].

The RESs are generally integrated into the grid through power converters without mechanical inertia and frequency damping. In such a case, when the SGs are replaced by the RESs, an inertia-less and damping-less power grid is formed, as demonstrated in Fig. 1.1. Although new rules may be developed for a 100% power electronics-based system, before they are established, the swing equation-based rules should be complied with [8]. Generally, the power converters are integrated into the power grids without adequate frequency support, especially the inertia provision. In this case, the power grids are more sensitive to disturbance, which may further result in frequency incident or even collapse [9]. For instance, there are two serious blackout incidents caused by frequency collapse in Australia and the UK, in 2016 and

2019, respectively [10, 11]. Those frequency collapses might be caused by the insufficient fault ride-through capabilities of the RESs and also the inertialess of the power grids. Thus, the frequency stability analysis, especially the inertia analysis, of the power grid with increasing penetration of power electronics should be focused on. To realize the inertia analysis, the modeling of power converters is important. Then, the inertia characteristics of the power converters and further the grid can be identified. In turn, it can guide the control strategy design of the power converters and the grid-connected RESs to enhance the grid inertia.

Relevant strategies can then be developed to address this issue. The most popular solution is the inertia provision from the power converters by modifying the control strategies, where the energy for inertia emulation can be supported by energy storage systems (ESS). On the other hand, alternative inertia can be generated by RESs, i.e., wind turbines or PV systems. As aforementioned, PV systems are important in the modern power grid, and also contribute to the inertia reduction. Additionally, the installed capacity of PV systems is still growing with remarkable speed, which makes it become one of the most important power sources in some countries, such as Germany and China [12, 13]. The PV systems are becoming more important to the power grid than ever. In this context, ancillary functionalities, especially frequency support and inertia emulation, are required for PV systems to support the grid rather than being constant power feeding units, which is also demanded by more and more grid codes [14–16]. However, to achieve those ancillary functionalities, the control strategies of PV systems should be modified, based on which the flexible PV power generation can be realized [17]. Thus, how to modify the control strategies of PV systems to effectively support the grid should be explored. It is important for the stability and safety of the power electronics-based power grids.

1.1.1 Modeling of Grid-Connected Power Converters

Modeling is the basis of stability analysis and control strategy design. To analyze the inertia characteristics and further the frequency stability of the power systems, the proper model of power converters should be developed first. Currently, two basic modeling approaches are used for power converters, i.e., the frequency-domain and the time-domain modeling.

The frequency-domain model is usually represented by transfer functions, based on which the equivalent impedance of power converters can be obtained [18, 19]. Then, the stability of the system can be revealed in the frequency-domain, making it popular for harmonic resonance analysis [20, 21]. However, it is relatively difficult to clarify the relationship between the variables based on the impedance model. Moreover, if the equivalent impedance of the converter is obtained by measurement technology,

it may become inaccurate when the system topology or the operation state varies. Additionally, when scaling-up, the model becomes very complicated. The time-domain model is usually established in the state space [6]. This model is the most classical one in the control area, where the system dynamic can be represented by the states of the variables of interests [22]. In the state space model, the relationship between variables can be conveniently investigated. Then, the control strategy can be designed to achieve desired objectives. As for the frequency and inertia analysis, the system dynamic at the electromechanical timescale is more interested in rather than the harmonic characteristic. Moreover, the impacts of different state variables on the frequency stability is of importance. Thus, the state space model is more suitable for frequency stability analysis and inertia emulation strategy design of power electronics-based systems.

For example, the averaged model of the switching-power converters was proposed in [23] revealing the nonlinear dynamics of switching elements with simplicity. The model of power converters considering the grid stiffness was proposed in [24] to analyze the stability when the power converters were connected to a weak grid. The model of a DC grid with multiple power converters was proposed in [25] to tune the droop control coefficients. However, most of these methods do not model the power converter and the grid independently. Then, the grid parameters (e.g., the grid impedance) are coupled with the converter parameters (e.g., the control gains). With the power grid expanding, the number of converters increases, and the control system of converters becomes more complicated. In such a case, the model is difficult to resolve, increasing the computational burden.

To make the model applicable in large-scale systems, the sub-system open-loop modeling method emerged [26–28]. In this modeling method, the open-loop model of power converters is obtained first. Meanwhile, the open-loop model of the grid is derived without the power converters. Connecting the converter model to the grid model yields the closed-loop system model. The similar concept was demonstrated in [29] to analyze the interaction between the converters in a multi-terminal DC (MTDC) grid. The key of the method is defining the external interfaces, i.e., the connecting parameters, based on which the open-loop models of the power converters and the grids can be connected to obtain the closed-loop model of the system. For power converters of different control strategies, although their open-loop models are with varying complexity, they provide the same external interfaces to the grid. In such a case, the modeling becomes simpler, avoiding the over-coupling of the grid parameters and the converter parameters.

Except for the universal modeling of power converters with different control strategies, the balance between precision and simplicity should also be considered. When the model considers many details of the power converters, it will become over-complicated. Then, it will make the analysis more

difficult, especially when there are multiple converters to be analyzed, e.g., the electromagnetic model for switching transient analysis [30]. On the other hand, the model is over-simplified when ignoring most of the control loops. It is usually employed to address the system level analysis, e.g., the steady-state model for power flow optimization [31]. Thus, the simplicity of the model should be carefully considered, with the simplification rules being properly designed. Aiming at this issue, the timescale analysis method was proposed in [32, 33]. Specifically, three basic timescales were defined for the control systems of power converters. For different requirements, the model at different timescale can be adopted, where the system dynamics at faster timescales can be ignored. Then, the model can be properly simplified while remaining the desired system features.

Inspired by the sub-system open-loop modeling method and the timescale analysis method, the models of power converters that can reflect the power-frequency characteristics at different timescales have been developed [33–39], based on which the power converter can be modeled in analogy with the SG, as shown in Fig. 1.2. The connecting parameters of the open-loop converter model include the input and output parameters. Specifically, the input parameters are the active and reactive power at the AC side of the converter. The output of the converter model is defined as the AC voltage of the converter, being referred to as the internal voltage. After receiving the internal voltage information provided by the power converters, the power distribution of the grid can be naturally determined. Moreover, the power-frequency characteristics of power converters can be analyzed in this way. This modeling method was employed in [33] to address the transient stability of wind turbines at the rotor motion timescale (RMT), and it was used to assess the stability of power converters at voltage control timescale (VCT) when being connected to the weak grid [36, 37]. It was also applied for wind farms [38] or modular multilevel converters [39] to analyze the system stability at the VCT. However, the modeling method has not been adopted for inertia analysis and the inertia emulation strategy design of power converters, which still requires further investigation.

1.1.2 Inertia Emulation of Power Converters

Based on the model of power converters, the inertia characteristic of the system can be analyzed, and the inertia emulation strategies of power converters can also be investigated. In spite of the RESs, the inertia emulation can be directly achieved by power converters with modified control strategies, e.g., virtual synchronous generators (VSG) [40], virtual synchronous machine (VSM) [41, 42], and synchronverters [43], and grid-forming converters with second-order power-frequency droop characteristics [44, 45]. With these control strategies, the virtual inertia can be provided by electrical en-

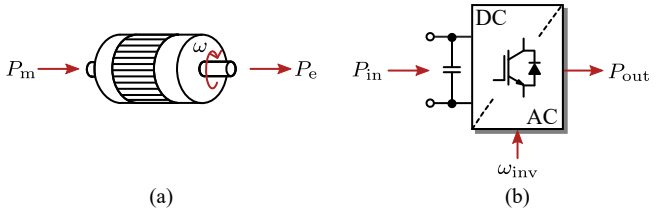

Fig. 1.2: Open-loop models of an SG and a grid-connected converter reflecting the power-frequency characteristics, where P_m and P_e are the mechanical power (input) and the electromagnetic power (output) of the SG, ω is the angular frequency of the rotor, P_{in} and P_{out} are the input power (from the DC source) and the output power of the converter, and ω_{inv} is the grid-synchronization frequency of the converter: (a) SG and (b) grid-connected converter.

ergy, instead of the kinetic energy in the SG. However, the energy for inertia provision comes from large-capacity ESSs, e.g., supercapacitors, or batteries, which inevitably increases the cost of the entire power generation.

For more universal inertia emulation solution, the virtual inertia control (VIC) of DC-link capacitors was reported in the literature. The virtual inertia can be naturally generated by the charging/discharging of the DC-link voltage in proportion to the frequency deviation [46–49]. That is, the electrical energy stored in the capacitor can be used to emulate inertia. This solution is independent of extra hardware, e.g., large capacity ESSs, and it is application-friendly without largely altering the basic control system. More importantly, the DC-link capacitor is one of the essential components in power converters, which makes it possible to become a universal inertia emulation solution in the power electronics-based systems, at least in emergency circumstances.

However, the systematic design of the VIC of DC-link capacitors has not been clearly discussed in the literature. For instance, in [46–49], the designed VIC of DC-link capacitors was designed according to the rated frequency, allowed DC-link voltage operation band, the capacity of DC-link capacitors, etc. Although with this consideration, the VIC can maintain the converter stability at a slower timescale, the stability at faster timescales, e.g., the VCT, is not considered, which is also important. To address this issue, the multi-timescale analysis of power converters should be conducted, where the dynamics of concerned timescales can be addressed. Then, the VIC can be properly tuned, and the optimal inertia that the DC-link capacitors can provide can be identified.

1.1.3 Flexible Power Control of PV Systems

Although the inertia provision of DC-link capacitors is a universal solution for inertia enhancement of the power electronics-based systems, the emulated inertia is limited by the capacitance. From a long-term perspective,

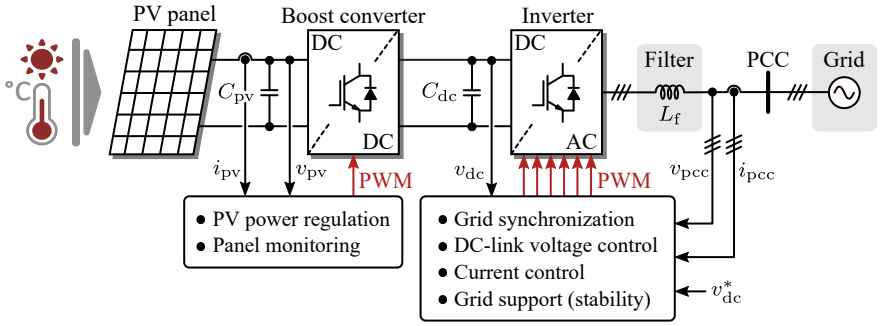

Fig. 1.3: Two-stage three-phase PV system, with C_{pv} and C_{dc} being the boost capacitor and the DC-link capacitor, L_f is the inverter filter inductance, i_{pv} and v_{pv} are the PV current and voltage, i_{pcc} and v_{pcc} are the current and voltage of the point of common coupling (PCC), and v_{dc} and v^*_{dc} are the DC-link voltage and its reference (PWM–pulse width modulation).

more vigorous inertia provision is expected. The grid-connected PV systems are potential as an effective solution. To achieve ancillary functionalities of PV systems, including frequency regulation and inertia emulation, the flexibly managing of the PV output power is necessary, which can be realized by flexible active power control.

A typical two-stage three-phase PV system is shown in Fig. 1.3. It can be seen in Fig. 1.3 that the PV system consists of a boost converter and an inverter. The boost converter usually regulates the PV output power, whereas the inverter is responsible for the DC-link voltage control and the grid synchronization [50]. Conventionally, the maximum power point tracking (MPPT) algorithm is adopted to maximize the energy yield of PV systems [51, 52]. However, when ancillary functionalities are required, the constant (maximum) power generation of PV systems should be altered to realize flexible power output. Then, the PV power regulation strategy should be modified as demanded. For instance, the PV power can be limited by a pre-set threshold, yielding the power limiting control of PV systems [53, 54]. Furthermore, the PV power can be limited adaptively according to requirements, e.g., overvoltage prevention [55]. The MPPT algorithm can be also modified to constrain the PV power ramp-rate [56, 57].

As for the frequency regulation and VIC of PV systems, the power reserve control (PRC) is necessary [58]. In some cases, e.g., for under-frequency issues, more PV power is demanded to balance the power shortage of the grid. One solution is to equip additional ESSs to the PV systems, which can release energy to tackle the under-frequency issues [59–61]. However, this increases the costs of the PV systems and also underutilizes the regulation potential of the PV systems. In addition, the lifetime of batteries is also challenging, compared to other components in the PV system [62], which also increases the cost. Independently on the ESSs, the PV system has no room to support the

grid by increasing output power at the maximum power point (MPP). Thus, to realize a cost-effective PV system, the PRC should be developed. When needed, the PV system can release the reserved power to support the grid.

In the PRC, the most important part is to measure the maximum available power (MAP), i.e., the maximum PV output power at the MPP. If the MAP is inaccurate, the power reserve point (PRP) cannot be properly identified. With different MAP measurement solutions, the PRC can be realized as follows.

- Use of sensors: This is the most accurate method to measure the MAP, where physical sensors are used to measure the solar irradiance and the ambient temperature [63, 64]. After that, the real-time P-V curve is identified, and the MPP is obtained. This method has been applied in [65, 66] for fast frequency response and VIC. However, this method inevitably increases the overall cost, which limits its application.

- Coordinated operation: To realize this method, the PV systems should contain at least two PV units (strings or panels, etc.) [58]. The PV unit(s) constantly operates in the MPPT mode as the master(s) to measure the real-time MAP. The rest operate with reduced output power, as the slaves. This method is popular for frequency regulation of PV systems [67, 68]. Nevertheless, the cautious selection of the master unit(s) and the backup strategy design make the application more complicated [69].

- Curve-fitting: By sampling several operation points, the P-V characteristic can be curve-fitted, which has been applied in [49, 70] to achieve inertia emulation. However, the accuracy of this method is based on the curve-fitting algorithms and the sample selection. Thus, although no additional hardware is required, the cumbersome workload caused by complicated algorithm design and cautious sample selection cannot be ignored [71].

- Empirical modeling: This method also estimates the MAP based on sampling. Different from the curve-fitting method, the empirical equations are adopted in this method to estimate the required information. For example, the MPP current can be estimated based on the short-circuit current [72]. Then, based on the Lambert-W function, the MPP and MAP can be estimated [73]. However, many variables in this method are estimations, based on which the results may lack accuracy to some extent.

In summary, there are various methods to measure the MAP and realize the PRC. However, most of them incur extra costs for the PV systems, e.g., the expenses for sensors, the increase of computational burden, or the decrease of accuracy. To avoid these deficiencies, a PRC method based on periodical

MPPT execution was proposed in [74]. In this method, the MAP is measured in real-time, and the result is accurate. Moreover, no extra hardware (e.g., sensors) is needed, while the computational burden in the curve-fitting-based method can be avoided. However, the application of this method in frequency regulation and VIC has not been thoroughly addressed, which requires further exploration.

Based on the PRC, the frequency control, including the VIC and the frequency damping control (FDC) can be achieved in PV systems. Typically, the main objective of VIC is to reduce the rate of change of frequency (RoCoF) [49, 70]. The FDC is mainly to damp the frequency deviation [65, 75]. Currently, the frequency regulation strategies of PV systems have not sufficiently considered the coordination of the VIC and the FDC in terms of the utilization of the power reserve. However, it is important to the control efficiency of PV systems. Thus, how to utilize power reserve to facilitate the optimal grid frequency support of PV systems should be considered.

1.1.4 Project Motivation

As presented in the above sections, there are several challenges regarding stability and control of the modern power grid with a high penetration degree of PV systems, where the frequency stability issue is of more concern than ever before. The frequency stability of the system is important. It can be enhanced by optimizing the contribution of PV systems to the frequency regulation. In this context, appropriate analysis methods and advanced control strategies should be explored. This motivates the Ph.D. project documented in this thesis.

Firstly, a proper modeling method of power converters should be developed. It should reflect the relationship of power, frequency, and inertia. Consequently, various power converters can be aggregated in the grid for the system-level analysis in terms of frequency stability. With the model, the impact of inertia emulation from DC-link capacitors on system stability can be investigated, as it has huge potential to be an essential function of power converters. This will help with the design of the VIC of the DC-link capacitors, and more importantly, the maximum virtual inertia that the DC-link capacitors can provide can be identified.

Secondly, to realize vigorous grid support, especially the frequency regulation, the flexible control of PV systems requires much exploration. To achieve the comprehensive frequency regulation, the power reserve of PV systems is demanded. In this context, a cost-effective and computation-efficient PRC method is of interest, while the optimal utilization of the power reserve should also be considered. Then, the modern power grid can be supported more adequately with smart PV systems. The comprehensive research activities in this Ph.D. project are summarized in Fig. 1.4.

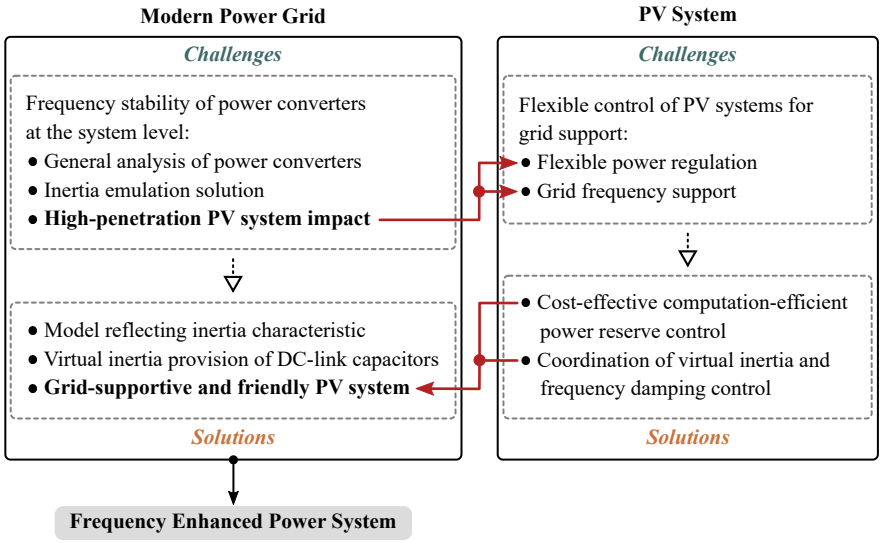

Fig. 1.4: Research activities in the Ph.D. project: *Stability and Control of Grid-Friendly PV Systems*.

1.2 Project Objectives and Limitations

As summarized in Fig. 1.4, the final goal of this project is to facilitate a frequency enhanced power system with high penetration of PV systems, which should be realized from two aspects:

i. The general analysis and control for frequency stability and regulation of power converters should be realized.

ii. The PV systems should be improved to provide sufficient support to the grid.

1.2.1 Research Questions and Objectives

Accordingly, a general research question emerges in this Ph.D. project:

- How to analyze and enhance the stability, especially the frequency stability, of the power electronics-based systems?

Starting from the general question, the following sub-questions are raised:

- How to model the power converters in a universal way for inertia analysis at the system level?
- Can the model be used to develop a universal inertia emulation solution of power converters?

- How to achieve a cost-effective and computation-efficient power reserve control of PV systems to facilitate flexible grid support?
- How to optimally utilize the power reserve to achieve the coordination of the VIC and FDC for more effective grid frequency support?

Considering these questions, the objectives (obj) of the Ph.D. project are summarized as follows.

Obj 1 – Universal modeling of power converters

For frequency stability and inertia characteristic analysis of the power electronics-based systems, a universal modeling method is demanded to take different power converters into consideration. Accordingly, this Ph.D. project will propose a modeling method for power converters, reflecting the power-internal-voltage (PIV) dynamics, based on which the characteristics of inertia, frequency, and active power can be addressed.

Obj 2 – Virtual inertia control of DC-link capacitors

The VIC of DC-link capacitors is one of the universal inertia emulation solutions in the power electronics-based systems. To fulfill it, this Ph.D. project will investigate the VIC of DC-link capacitors, which will be conducted based on the universal model of power converters (Obj 1). Specifically, the impact of the VIC on the system stability will be addressed based on the model. Then, the maximum virtual inertia that the DC-link capacitors can provide will be identified.

Obj 3 – Develop cost-effective power reserve control for frequency regulation

The PRC of PV systems independent of sensors, cumbersome computational workload, and unreliable estimations, will be developed in this Ph.D. project. Based on the PRC, the PV systems can participate more to support the grid without drastically raising the cost. Moreover, large-scale ESSs can be avoided in this solution. This will benefit the further development of PV systems in modern power systems.

Obj 4 – Coordinate the VIC and FDC

Based on the PRC (Obj 3), the flexible regulation of PV systems can be realized. From the perspective of the grid, the demands of the VIC and the FDC will vary in different stages of a frequency instability case. Accordingly, the coordination strategy of the VIC and the FDC of PV systems will be designed. With the adaptive VIC and FDC, the power reserve of the PV systems will be utilized more reasonably, leading to more adequate grid frequency support.

1.2.2 Project Limitations

The power converters in the power electronics-based systems may be with various configurations and distinct control strategies. When the power converter is with different topologies, the control system may differ significantly, where additional components may be required. In this Ph.D. project, the modeling method and the VIC of the DC-link capacitors are mainly based on the analysis at the converter level (and/or higher levels). Thus, the typical three-phase full-bridge two-level topology is applied. In addition, the dual-loop control strategy, i.e., the voltage/power outer controller and the current inner controller, is also popular in the control of power converters, and is widely applied in the industry. Hence, the discussion is exemplified in the power converter with the dual-loop control strategy. Moreover, although there are tremendous grid synchronization solutions, the phase-locked loop (PLL) is still the most popular one. Thus, the PLL is adopted to establish the synchronous reference frame. It should be mentioned that the modeling method can be expanded to power converters controlled by different strategies with necessary modifications. Then, the PIV characteristics of power converters can be obtained for system level analysis. Additionally, the converter dynamic at the current control timescale is usually analyzed for harmonic issues [32, 76], which is not the focus of this Ph.D. project. Thus, in the multi-timescale modeling and analysis in this Ph.D. project, the dynamics at the VCT will be concentrated.

As for the PV system, the topology is usually designed based on the power rating. For PV systems with different configurations, the basic control strategies may vary from each other. Then, the ancillary control strategies, e.g., the grid frequency regulation, may need to be realized in different ways. In this Ph.D. project, the residential two-stage three-phase PV systems are mainly focused on. Specifically, the string/multi-string configuration is adopted for PV panels. Additionally, the boost converter is applied as the DC-DC stage, while the three-phase two-level inverter is responsible for DC-AC conversion.

When addressing the model of the grid-connected converters, an infinite-bus system is adopted to represent the grid, based on which the model can be effectively validated. However, the infinite-bus system is not suitable to validate the frequency stability, where the power is balanced well, and it is then difficult to investigate the frequency dynamic. Thus, when the focus is the frequency stability of the power converters/PV systems, the grid is represented by a VSG, which can reflect the dynamic of an SG.

Finally, the research of this Ph.D. project is validated by simulations in MATLAB/Simulink or PSCAD/EMTDC. Although the simulation may not match the real system 100%, the converter level (and/or above) dynamic can be revealed appropriately. Moreover, the control system is modeled in the

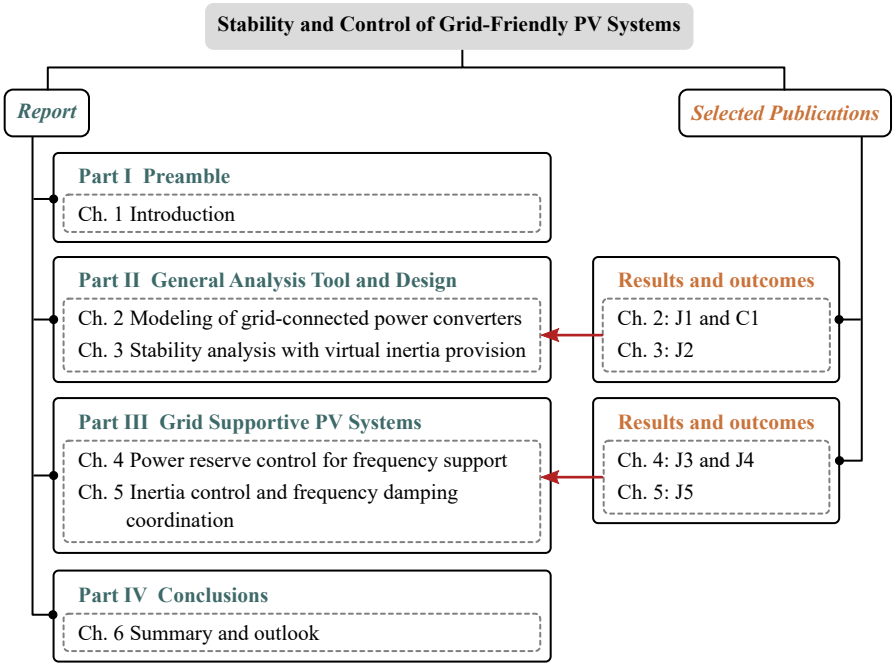

Fig. 1.5: Thesis structure of the Ph.D. project and the covered topics with respect to Fig. 1.4.

discrete-time domain, which makes it closer to a practical controller. In that case, the performance of the control strategies can be depicted clearly. Additionally, the VIC of the DC-link capacitors is further validated by an experimental setup, which is constructed by a real-time simulator (Plexim/RT-Box) and a digital control platform (dSPACE/MicroLabBox). Discretization and delays may affect the analysis, which is not considered in this project.

1.3 Thesis Outline

The outcomes of the Ph.D. project are summarized in the Ph.D. thesis, which is based on the collection of papers published during the study. The documented thesis consists of two parts: ***Report*** and ***Selected Publications***. Fig. 1.5 demonstrates the thesis structure and the topics with related publications. The details will be presented in Section 1.4.

In the ***Report***, the summary of the research in the Ph.D. project is presented. All of the contents are supported by the ***Selected Publications***. The ***Report*** consists of four parts, which are organized into six chapters:

- *Part I – Preamble* contains *Chapter 1 – Introduction*, which briefs the background, objectives, and the structure of this Ph.D. thesis.

- *Part II – General Analysis Tool and Design* includes two chapters. *Chapter 2 – Modeling of Grid-Connected Power Converters* presents the universal modeling of power converters, which reflects the power-internal-voltage characteristics of power converters. *Chapter 3 – Stability Analysis with Virtual Inertia Provision* mainly focuses on the VIC design of the DC-link capacitors. Based on the analysis, the maximum inertia provided by DC-link capacitors is identified.

- *Part III – Grid-Supportive PV Systems* incorporates two chapters. *Chapter 4 – Power Reserve Control for Frequency Support* presents an event-triggering PRC of PV systems. Then, the VIC of PV systems is realized based on the proposed PRC. *Chapter 5 – Inertia Control and Frequency Damping Coordination* addresses the coordination strategy design of the VIC and the FDC of PV systems, of which the objective is to optimally utilize the power reserve in terms of grid frequency support.

- *Part IV – Conclusions* are constructed by *Chapter 6 – Summary and Outlook*, where the concluding remarks and main contribution of this Ph.D. project are given. Additionally, future research perspectives are presented.

1.4 List of Publications

The outcomes of the Ph.D. study have been disseminated in journal papers and conference publications as listed in the following. Parts of them are indirectly used in the Ph.D. thesis.

Publications in Refereed Journals

J1. **Q. Peng**, Q. Jiang, Y. Yang, T. Liu, H. Wang, and F. Blaabjerg, "On the Stability of Power Electronics-Dominated Systems: Challenges and Potential Solutions," *IEEE Trans. Ind. App.*, vol. 55, no. 6, pp. 7657–7670, Nov.-Dec. 2019.

J2. **Q. Peng**, J. Fang, Y. Yang, T. Liu, and F. Blaabjerg, "Maximum Virtual Inertia from DC-Link Capacitors Considering System Stability at Voltage Control Timescale," *IEEE J. Emerg. Select. Topics Circuits Syst.*, Status: Under Review.

J3. **Q. Peng**, A. Sangwongwanich, Y. Yang, and F. Blaabjerg, "Grid-Friendly Power Control for Smart Photovoltaic Systems," *Solar Energy*, Status: In Press, DOI: 10.1016/j.solener.2020.05.001.

J4. **Q. Peng**, Z. Tang, Y. Yang, T. Liu, and F. Blaabjerg, "Event-Triggering Virtual Inertia Control of PV Systems with Power Reserve," *IEEE Trans. Ind. App.*, Status: Under Review.

J5. **Q. Peng**, Y. Yang, T. Liu, and F. Blaabjerg, "Coordination of Virtual Inertia Control and Frequency Damping in PV Systems for Optimal Frequency Support," *CPSS Trans. Power Electron. App.*, Status: Under Review.

Publications in Refereed Conferences

C1. **Q. Peng**, Y. Yang, and F. Blaabjerg, "State-Space Modeling of Grid-Connected Power Converters Considering Power-Internal Voltage Characteristics," in *Proc. IEEE ICPE 2019 - ECCE Asia*, Busan, Korea, May 2019, pp. 3047–3053.

Publications Excluded in This Thesis

C2. **Q. Peng**, J. Fang, Y. Yang, and F. Blaabjerg, "A Universal Model for Grid-Connected Converters Reflecting Power-Internal Voltage Characteristics," in *Proc. IEEE 4th SPEC*, Singapore, Dec. 2018, pp. 1–7.

C3. **Q. Peng**, Y. Yang, H. Wang, and F. Blaabjerg, "On Power Electronized Power Systems: Challenges and Solutions," in *Proc. IEEE IAS Annual Meeting*, Portland, OR, USA, Sep. 2018, pp. 1–9.

C4. **Q. Peng**, Z. Tang, Y. Yang, and F. Blaabjerg, "Event-Triggering Power Reserve Control for Grid-Connected PV Systems," in *Proc. IEEE APEC 2020*, Mar. 2020, pp. 417–423.

Chapter 2

Modeling of Grid-Connected Power Converters

This chapter will discuss the modeling of grid-connected power converters. The open-loop modeling method will be used to make the models of power converters independent of grid parameters. The model will reflect the PIV characteristics of power converters, which paves the way for inertia-related analysis.

2.1 Introduction

The power electronics-based system may consist of various power generating/consuming units, e.g., wind farms, PV systems, batteries, and electric vehicles. Many of the power units are integrated into the grid through power electronics converters. However, the control strategies of these converters may vary according to the features of power units. For instance, for the inverter in a PV system, the control aim is usually the DC-link voltage [77]. Then, the stable DC-link voltage can support steady PV power production. Nevertheless, in some cases, the PV systems are integrated into the AC grid through a multi-terminal DC grid, which consists of various power units [78]. In this case, the grid-connected converter may be controlled by the constant active power controller or the constant DC-link voltage controller, which may differ from the power converter integrating a single PV system. In addition, the power converters may be modified to achieve more functionalities or improve the control performance, i.e., the low-voltage ride-through controller of PV systems [79] according to the grid demands.

In this context, the dynamics of the power grids become different from the conventional SG-based systems, as these power generating units impact the

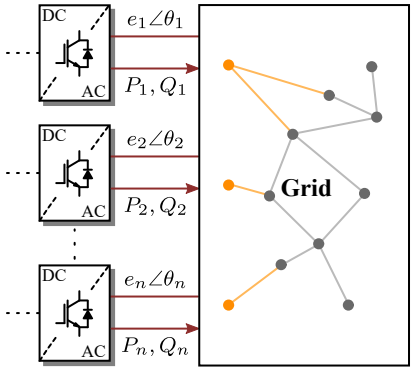

Fig. 2.1: Closed-loop model of a power electronics-based system employing the open-loop modeling method (n converters), where $e\angle\theta$ is the internal voltage, P and Q are the active and reactive power output from the power converter, respectively, and the subscript indicates the n^{th} converter. Source: [J1].

grid characteristics diversely. The stability analysis of power grids consisting of multiple power converters with different control strategies becomes difficult and cross-coupled. Furthermore, the control strategy design of power converters is also challenged due to the lack of proper stability criteria. Thus, a universal modeling method of power converters is demanded, which is the foundation of the stability analysis and control design of large-scale power electronics-based systems. In the literature, the modeling of grid-connected power converters usually did not consider the decoupling of the converter model and the grid model. Instead, the closed-loop model of the entire system was obtained as a whole, as demonstrated in [80, 81]. Those models are sufficient for analysis of the single converter. However, when multiple power converters are integrated into the same power grid, the modeling will become complicated, as the model of the entire grid with multiple converters will be obtained uniformly, which requires cumbersome computation. Moreover, when the system topology changes, the closed-loop system model should be modified with a non-negligible computational cost. To tackle these issues, it is suggested to model the power converters and the grid separately, and then, connect them to acquire the closed-loop model of the entire system. To achieve so, the converters should have the same external interfaces, based on which the models can be flexibly connected or disconnected to the grid model.

For different purposes, the external interface of the universal model can be modified. For instance, the input and output variables of the open-loop models of power converters in [26, 27] are the voltage and current, respectively. As aforementioned, with the penetration of power electronics, the inertia characteristics and further the frequency stability of the power grids

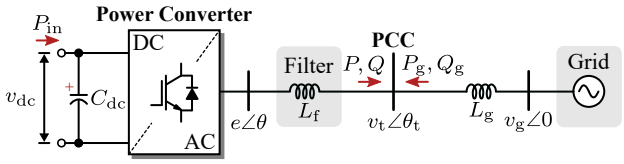

Fig. 2.2: Configuration of a grid-connected power converter, where $v_{\text{t}}\angle\theta_{\text{t}}$ is the terminal voltage (the voltage at the PCC), $v_g\angle 0$ is the grid voltage (as the reference), C_{dc} is the DC-link capacitor, v_{dc} is the DC-link voltage, L_{f} and L_{g} are the inductance of the converter filter and the grid, respectively, P_{g} and Q_{g} are the output power of the grid, and P_{in} is the DC source power (PCC – point of common coupling). Source: [C1].

become complicated, which requires adequate exploration. For a conventional SG, the inertia decides the characteristics of active power and internal voltage phase angle. Accordingly, the PIV relationship of a power converter can reflect its inertia characteristic.

Another issue is that the model should be appropriately simplified according to applications or adapted properly based on system topologies. Thus, precision and simplicity should be balanced in the modeling. According to the concept of timescale analysis method, for different objectives, the model at different timescales can be applied. In such a case, the dynamics at faster timescales can be neglected, and the model can be properly simplified with retaining required features.

To address the inertia characteristics of power converters as well as the stability analysis, the small-signal PIV model with the open-loop modeling method will be demonstrated in this chapter, where the focus will be on the VCT. For the open-loop model of each power converter, the input parameters are the converter output power. The output parameter is the internal voltage (amplitude and phase angle). By integrating the open-loop models of all the power converters to the grid, the closed-loop system model can be developed, as shown in Fig. 2.1. The inertia characteristic and the frequency stability of the grid can then be analyzed. Then, the global inertia placement optimization as demonstrated in [82, 83] can be improved with considering the converter stability. This will be conducted in future work.

The modeling is exemplified in a grid-connected power converter as shown in Fig. 2.2. In this configuration, the grid is represented by an infinite-bus system. In the following, the open-loop PIV model of the power converter at the VCT will be detailed in the state space.

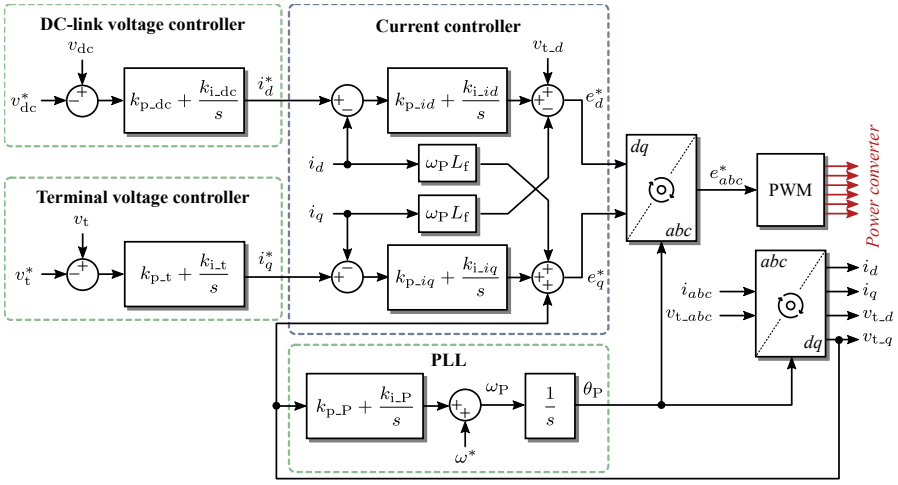

Fig. 2.3: Diagram of the dual-loop control strategy, where the DC-link voltage control and the terminal voltage control are the outer-loop controllers, "$*$" stands for the reference or the rated value, and the other parameters will be defined during the modeling (PLL – phase-locked loop; PWM – pulse width modulation). Source: [C1].

2.2 Control and Modeling of Power Converters

2.2.1 General Control of Power Converters

As introduced in the above, the key to the open-loop modeling is to have identical interfaces of power converters under different control strategies. Although there are tremendous control strategies in the literature, the most widely applied one, especially in the industry, is still the dual-loop control based on the rotating synchronous frame (*dq*-frame) [84, 85]. Thus, the dual-loop control strategy is adopted in this chapter.

The dual-loop control scheme is shown in Fig. 2.3. The outer-loop controllers (i.e., the DC-link voltage controller and the terminal voltage controller) generate the references of the inner-loop controller (current controller). Then, the reference of the internal voltage, e^*_{abc}, will be generated by the current controllers. Subsequently, it will be transferred to the modulation unit. In this chapter, the synchronous reference frame PLL (SRF-PLL) is implemented for grid synchronization, which is one of the most popular solutions. Based on the SRF-PLL, the variables can be transformed between the *abc*-frame and the *dq*-frame. Moreover, the grid frequency can be measured by the PLL as well, based on which the additional frequency control becomes possible. Thus, the PLL is of importance for the entire control system. The SRF-PLL can be modified or be replaced by other grid synchronization schemes, e.g., the decoupled double SRF-PLL [86] or the SG-emulated

synchronization method [87]. Moreover, the outer-loop controllers may be modified according to control objectives, e.g., the active power controller, the frequency controller, or the power-voltage (DC-link voltage) droop controller. When the control strategies are different from the one exemplified in this chapter, the concept of the open-loop PIV modeling for power converters can be also adopted, as long as the PIV relationship is obtained.

2.2.2 Open-Loop Power-Internal-Voltage Model

The small-signal open-loop PIV model of power converter regardless of the grid dynamic will be obtained. It will concentrate on the VCT. For simplicity, several assumptions are made before modeling [C1]:

- The dynamics of the current controllers and the faster control loops (e.g., the PWM) are ignored in this section. This is tenable by assuming that those control loops at faster timescales can track the references with negligible delays.
- The dynamic of the DC source is not considered in the modeling, i.e., $P_{\text{in}} = 0$ in Fig. 2.2. This is due to that the focus of this chapter is on the converter power exchange with the AC side, emulating the external characteristics of an SG.
- The resistances of the arms, the filter and the lines are ignored, as the resistances contribute more to the dynamics of the current controller, which barely affect the stability at the outer-loop control timescale [36].

With the above assumptions, the power converter can be universally modeled in the form of several modules as follows:

1) DC-link capacitor dynamic

The dynamic of the DC-link capacitor is affected by the relationship between the DC-link voltage and the active power. When ignoring the resistance in the system, it can be obtained that

$$C_{\text{dc}} v_{\text{dc}} \frac{dv_{\text{dc}}}{dt} = P_{\text{in}} - P. \tag{2.1}$$

When the DC source dynamic is neglected, its small signal model is

$$\frac{d\Delta v_{\text{dc}}}{dt} = -\frac{1}{C_{\text{dc}} v_{\text{dc0}}} \Delta P, \tag{2.2}$$

in which the subscript "0" being the equilibrium state and the prefix "Δ" being the small signal disturbance around the equilibrium state. When the small signal stability around the steady-state is focused, the steady-state is the equilibrium state.

2) DC-link voltage and terminal voltage control loops

The DC-link voltage controller regulates the DC-link voltage to follow the reference. It generates the d-axis current reference by a proportional-integral (PI) controller. Correspondingly, the terminal voltage controller generates the reference for the q-axis current. According to Fig. 2.3, their small signal models are

$$\begin{cases} \Delta i_{\mathrm{d}}^{*} = \Delta\varphi_{\mathrm{dc}} + k_{\mathrm{p\_dc}}(\Delta v_{\mathrm{dc}} - \Delta v_{\mathrm{dc}}^{*}) \\ \Delta i_{\mathrm{q}}^{*} = \Delta\varphi_{\mathrm{t}} + k_{\mathrm{p\_t}}(\Delta v_{\mathrm{t}} - \Delta v_{\mathrm{t}}^{*}) \end{cases}, \tag{2.3}$$

where $k_{\mathrm{p\_dc}}$ and $k_{\mathrm{p\_t}}$ are the proportional gains of the DC-link voltage controller and the terminal voltage controller, and φ_{dc} and φ_{t} are state variables. The small signal models of the state variables are given as

$$\begin{cases} \dfrac{d\Delta\varphi_{\mathrm{dc}}}{dt} = k_{\mathrm{i\_dc}}(\Delta v_{\mathrm{dc}} - \Delta v_{\mathrm{dc}}^{*}) \\ \dfrac{d\Delta\varphi_{\mathrm{t}}}{dt} = k_{\mathrm{i\_t}}(\Delta v_{\mathrm{t}} - \Delta v_{\mathrm{t}}^{*}) \end{cases}, \tag{2.4}$$

with $k_{\mathrm{i\_dc}}$ and $k_{\mathrm{i\_t}}$ being the integral gains of the DC-link voltage controller and the terminal voltage controller.

3) Phase-locked loop

The PLL is responsible for the measurement of the terminal voltage phase angle. In steady-state, the PLL tracks the terminal voltage phase angle steadily. The direction of the d-axis is consistent with the terminal voltage. However, when the system suffers from a disturbance, the tracking error emerges. In this case, the d-axis established by the PLL will deviate from the terminal voltage. Then, the performance of the control system will be affected. The impact of the PLL on the dq-decomposition of the internal and terminal voltages under disturbance is shown in Fig. 2.4. It can be seen in Fig. 2.4 that when the system is disturbed, the d-axis does not conform with the terminal voltage, which results in $\Delta\theta_{\mathrm{t}}^{\mathrm{P}}$.

According to Fig. 2.3, the small signal model of the SRF-PLL in the s-domain (complex frequency domain) is given as

$$\Delta\theta_{P} = v_{\mathrm{t0}}\Delta\theta_{\mathrm{t}}^{\mathrm{P}}(k_{\mathrm{p\_P}} + \frac{k_{\mathrm{i\_P}}}{s})\frac{1}{s}, \tag{2.5}$$

where $k_{\mathrm{p\_P}}$ and $k_{\mathrm{i\_P}}$ are the PI gains of the PLL. In steady-state, it can be considered that the terminal voltage amplitude is close to the grid voltage, i.e., $v_{\mathrm{t0}} \approx v_{\mathrm{g0}} = 1$. Thus, the small signal model of the SRF-PLL in the time domain is

$$\frac{d\Delta\theta_{\mathrm{P}}}{dt} = k_{\mathrm{p\_P}}\Delta\theta_{\mathrm{t}}^{\mathrm{P}} + k_{\mathrm{i\_P}}\Delta\varphi_{\mathrm{P}}, \tag{2.6}$$

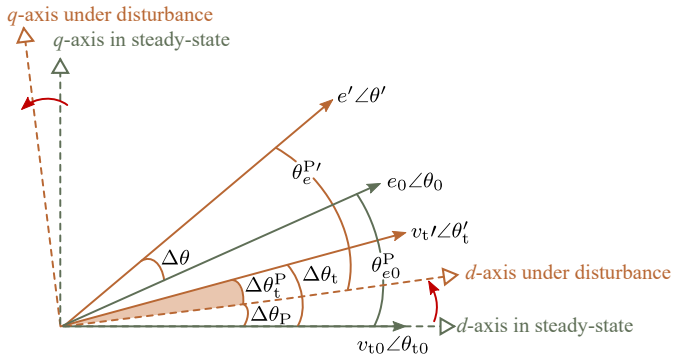

Fig. 2.4: Internal voltage and terminal voltage in the dq-frame in the steady-state and under disturbance, where θ_{P} is the phase angle tracked by the PLL, $\theta_{\mathrm{e}}^{\mathrm{P}}$ and $\theta_{\mathrm{t}}^{\mathrm{P}}$ are the phase angles of the internal and terminal voltages with respect to the d-axis, and the superscript "$\prime$" stands for the disturbed value. Source: [C1].

where φ_{P} is a state variable with its small signal model being

$$\frac{d\Delta\varphi_{\mathrm{P}}}{dt} = \Delta\theta_{\mathrm{t}}^{\mathrm{P}}. \tag{2.7}$$

4) Filter dynamic

The dynamic of the output filter is important for the open-loop power converter modeling. It contributes to express the converter output power without considering the grid parameters. As shown in Fig. 2.3, the dynamic of the filter is reflected by the characteristics of the internal voltage, the terminal voltage, and the converter output power. Specifically, the voltage drop on the filter inductance is described as

$$\begin{cases} e\cos\theta_e^{\mathrm{P}} = v_{\mathrm{t}}\cos\theta_{\mathrm{t}}^{\mathrm{P}} - X_{\mathrm{f}} i_q \\ e\sin\theta_e^{\mathrm{P}} = v_{\mathrm{t}}\sin\theta_{\mathrm{t}}^{\mathrm{P}} + X_{\mathrm{f}} i_d \end{cases}, \tag{2.8}$$

in which X_{f} is the reactance corresponding to L_{f}.

In steady-state, the d-axis complies with the terminal voltage, which yields $\theta_{\mathrm{t0}}^{\mathrm{P}} = 0$. Additionally, in steady-state, the phase angles of the internal and terminal voltages are usually smaller than 10°, of which the difference can be ignored. Thus, $\theta_{e0}^{\mathrm{P}} \approx \theta_{\mathrm{t0}}^{\mathrm{P}} = 0$ [34], and the linearization of (2.8) can be obtained as [C1]

$$\begin{cases} \Delta e = \Delta v_{\mathrm{t}} - X_{\mathrm{f}} i_q \\ \Delta\theta_e^{\mathrm{P}} = \dfrac{X_{\mathrm{f}}}{e_0}\Delta i_d + \dfrac{X_{\mathrm{f}}}{v_{\mathrm{t0}}}\Delta\theta_{\mathrm{t}}^{\mathrm{P}} \end{cases}. \tag{2.9}$$

The converter output power is determined by the relationship between the internal voltage and the terminal voltage. In turn, the interaction of the

voltages can be reflected by the converter output power characteristics, which is given as

$$\begin{cases} P = \dfrac{ev_{\mathrm{t}}\sin(\theta-\theta_{\mathrm{t}})}{X_{\mathrm{f}}} \\ Q = \dfrac{e^2 - ev_{\mathrm{t}}\cos(\theta-\theta_{\mathrm{t}})}{X_{\mathrm{f}}} \end{cases}. \tag{2.10}$$

which can be linearized as [34]

$$\begin{cases} \Delta\theta = \Delta\theta_{\mathrm{t}} + \dfrac{X_{\mathrm{f}}}{e_0 v_{\mathrm{t}0}}\Delta P \\ \Delta e = \dfrac{e_0}{2e_0 - v_{\mathrm{t}0}}\Delta v + \dfrac{X_{\mathrm{f}}}{2e_0 - v_{\mathrm{t}0}}\Delta Q \end{cases}. \tag{2.11}$$

Combining (2.9) and (2.11) results in the dynamic of the filter being described as [C1]

$$\begin{cases} \Delta\theta_{\mathrm{t}}^{\mathrm{P}} = \dfrac{X_{\mathrm{f}}}{e_0 - v_{\mathrm{t}0}}\Delta i_d - \dfrac{X_{\mathrm{f}}}{v_{\mathrm{t}0}(e_0 - v_{\mathrm{t}0})}\Delta P \\ \Delta\theta_{e}^{\mathrm{P}} = \dfrac{X_{\mathrm{f}}}{e_0 - v_{\mathrm{t}0}}\Delta i_d - \dfrac{X_{\mathrm{f}}}{e_0(e_0 - v_{\mathrm{t}0})}\Delta P \end{cases}, \tag{2.12}$$

$$\begin{cases} \Delta v_{\mathrm{t}} = \dfrac{(2e_0 - v_{\mathrm{t}0})X_{\mathrm{f}}}{e_0 - v_{\mathrm{t}0}}\Delta i_q + \dfrac{X_{\mathrm{f}}}{v_{\mathrm{t}0}(e_0 - v_{\mathrm{t}0})}\Delta Q \\ \Delta e = \dfrac{e_0 X_{\mathrm{f}}}{e_0 - v_{\mathrm{t}0}}\Delta i_q + \dfrac{X_{\mathrm{f}}}{v_{\mathrm{t}0}(e_0 - v_{\mathrm{t}0})}\Delta Q \end{cases}. \tag{2.13}$$

5) Current control loop

As aforementioned, the CCT and other timescales faster than the VCT are ignored. With this condition, the current controller can track the references immediately, i.e.,

$$\begin{cases} \Delta i_d = \Delta i_d^* \\ \Delta i_q = \Delta i_q^* \end{cases}. \tag{2.14}$$

With the modules demonstrated in the above, the open-loop model of the power converter can be obtained as [C1]

$$\begin{cases} \dfrac{d\Delta \boldsymbol{x}_{\mathrm{con}}}{dt} = \boldsymbol{A}_{\mathrm{con}}\Delta\boldsymbol{x}_{\mathrm{con}} + \boldsymbol{B}_{\mathrm{con}}^{*}\Delta\boldsymbol{u}^{*} + \boldsymbol{B}_{\mathrm{con}}^{\mathrm{g}}\Delta\boldsymbol{P}\boldsymbol{Q} \\ \Delta\boldsymbol{y}_{\mathrm{con}} = \boldsymbol{C}_{\mathrm{con}}\Delta\boldsymbol{x}_{\mathrm{con}} + \boldsymbol{D}_{\mathrm{con}}^{*}\Delta\boldsymbol{u}^{*} + \boldsymbol{D}_{\mathrm{con}}^{\mathrm{g}}\Delta\boldsymbol{P}\boldsymbol{Q} \end{cases}, \tag{2.15}$$

where $\Delta\boldsymbol{x}_{\mathrm{con}}$, $\Delta\boldsymbol{u}^{*}$, $\Delta\boldsymbol{P}\boldsymbol{Q}$, and $\Delta\boldsymbol{y}_{\mathrm{con}}$ are the matrices of the state variables, reference (input) variables, power (input) variables, and the output variables,

respectively. Those are defined as [C1]

$$\begin{cases} \Delta \boldsymbol{x}_{\text{con}} = \begin{bmatrix} \Delta\varphi_{\text{dc}} & \Delta\varphi_{\text{t}} & \Delta\varphi_{\text{P}} & \Delta\theta_{\text{P}} & \Delta v_{\text{dc}} \end{bmatrix}^{-1} \\ \Delta \boldsymbol{u}^* = \begin{bmatrix} \Delta v_{\text{dc}}^* & \Delta v_{\text{t}}^* \end{bmatrix}^{-1} \\ \Delta \boldsymbol{PQ} = \begin{bmatrix} \Delta P & \Delta Q \end{bmatrix}^{-1} \\ \Delta \boldsymbol{y}_{con} = \begin{bmatrix} \Delta\theta & \Delta e \end{bmatrix}^{-1} \end{cases}, \tag{2.16}$$

The state matrices are given in the following [C1]:

$$\boldsymbol{A}_{\text{con}} = \begin{bmatrix} 0 & 0 & 0 \\ 0 & k_{\text{i\_t}} K (2e_0 - v_{\text{t0}}) X_{\text{f}} & 0 \\ k_{\text{i\_P}} X_{\text{f}} / (e_0 - v_{\text{t0}}) & 0 & k_{\text{i\_dc}} \\ k_{\text{p\_P}} X_{\text{f}} / (e_0 - v_{\text{t0}}) & 0 & 0 \\ 0 & 0 & k_{\text{p\_P}} X_{\text{f}} k_{\text{p\_dc}} / (e_0 - v_{\text{t0}}) \\ 0 & 0 & 0 \end{bmatrix}, \tag{2.17}$$

$$\boldsymbol{B}_{\text{con}}^* = \begin{bmatrix} -k_{\text{i\_dc}} & 0 \\ 0 & -[k_{\text{i\_t}} K (2e_0 - v_{\text{t0}}) X_{\text{f}} k_{\text{p\_t}} + k_{\text{i\_t}}] \\ -k_{\text{i\_P}} X_{\text{f}} k_{\text{p\_dc}} / (e_0 - v_{\text{t0}}) & 0 \\ -k_{\text{p\_P}} X_{\text{f}} k_{\text{p\_dc}} / (e_0 - v_{\text{t0}}) & 0 \\ 0 & 0 \end{bmatrix}, \tag{2.18}$$

$$\boldsymbol{B}_{\text{con}}^{\text{g}} = \begin{bmatrix} 0 & 0 \\ 0 & k_{\text{i\_t}} K X_{\text{f}} \\ -k_{\text{i\_P}} X_{\text{f}} / [v_{\text{t0}} (e_0 - v_{\text{t0}})] & 0 \\ -k_{\text{p\_P}} X_{\text{f}} / [v_{\text{t0}} (e_0 - v_{\text{t0}})] & 0 \\ -1 / (C_{\text{dc}} v_{\text{dc0}}) & 0 \end{bmatrix}, \tag{2.19}$$

$$\boldsymbol{C}_{\text{con}} = \begin{bmatrix} X_{\text{f}} / (e_0 - v_{\text{t0}}) & 0 & 0 & 1 & X_{\text{f}} k_{\text{p\_dc}} / (e_0 - v_{\text{t0}}) \\ 0 & e_0 K X_{\text{f}} & 0 & 0 & 0 \end{bmatrix}, \tag{2.20}$$

$$\boldsymbol{D}_{\text{con}}^* = \begin{bmatrix} -X_{\text{f}} k_{\text{p\_dc}} / (e_0 - v_{\text{t0}}) & 0 \\ 0 & -e_0 K X_{\text{f}} k_{\text{p\_t}} \end{bmatrix}, \tag{2.21}$$

$$\boldsymbol{D}_{\text{con}}^{\text{g}} = \begin{bmatrix} -X_{\text{f}} / [e_0 (e_0 - v_{\text{t0}})] & 0 \\ 0 & (e_0 K X_{\text{f}} + X_{\text{f}}) / (2e_0 - v_{\text{t0}}) \end{bmatrix}, \tag{2.22}$$

where

$$K = 1 / [(e_0 - v_{\text{t0}}) - (2e_0 - v_{\text{t0}}) X_{\text{f}} k_{\text{p\_t}}]. \tag{2.23}$$

It can be seen in (2.15) that despite the reference matrix, the power matrix is also the input of the open-loop model of the power converter. The outputs of the open-loop model are the phase angle and amplitude of the internal voltage. Thus, the relationship between the power and the internal voltage, i.e., the PIV characteristic, has been obtained.

2.2.3 Closed-Loop Model

The closed-loop system model can be obtained by connecting the open-loop models of the power converter and the grid. For the open-loop grid model, the input is the internal voltage of the power converter, whereas the output is the power at the PCC. This is given as

$$\begin{cases} P = \dfrac{ev_{\mathrm{g}}sin\theta}{X_{\mathrm{f}} + X_{\mathrm{g}}} \\ Q = \dfrac{e^2 - ev_{\mathrm{g}}cos\theta}{X_{\mathrm{f}} + X_{\mathrm{g}}} \end{cases}, \tag{2.24}$$

with X_{g} being the reactance corresponding to L_g.

As aforementioned, the phase angle of the internal voltage can be assumed to be zero in steady-state, i.e., $\theta_0 \approx 0$. Additionally, the grid voltage is considered to be ideal (without any disturbances). Thus, linearizing (2.24) yields the small signal model of the grid as

$$\Delta \boldsymbol{PQ} = \boldsymbol{G}\Delta \boldsymbol{y}_{\mathrm{con}}, \tag{2.25}$$

with

$$\boldsymbol{G} = \begin{bmatrix} e_0 v_{\mathrm{g}0} cos\theta_0 / (X_{\mathrm{f}} + X_{\mathrm{g}}) & 0 \\ 0 & (2e_0 - v_{\mathrm{g}0} cos\theta_0)/(X_{\mathrm{f}} + X_{\mathrm{g}}) \end{bmatrix}. \tag{2.26}$$

Substituting (2.25) into (2.15) obtains the closed-loop system model as [C1]

$$\begin{cases} \dfrac{d\Delta \boldsymbol{x}_{\mathrm{con}}}{dt} = \boldsymbol{A}_{\mathrm{cl}}\Delta \boldsymbol{x}_{\mathrm{con}} + \boldsymbol{B}_{\mathrm{cl}}\Delta \boldsymbol{u}^* \\ \Delta \boldsymbol{y}_{\mathrm{con}} = \boldsymbol{C}_{\mathrm{cl}}\Delta \boldsymbol{x}_{\mathrm{con}} + \boldsymbol{D}_{\mathrm{cl}}\Delta \boldsymbol{u}^* \end{cases}, \tag{2.27}$$

with the state matrices given as [C1]

$$\begin{aligned} \boldsymbol{A}_{cl} &= \boldsymbol{A}_{\mathrm{con}} + \boldsymbol{B}^g_{\mathrm{con}}(\boldsymbol{G}^{-1} - \boldsymbol{D}^{\mathrm{g}}_{con})^{-1}\boldsymbol{C}_{\mathrm{con}}, \\ \boldsymbol{B}_{cl} &= \boldsymbol{B}^*_{\mathrm{con}} + \boldsymbol{B}^g_{\mathrm{con}}(\boldsymbol{G}^{-1} - \boldsymbol{D}^{\mathrm{g}}_{\mathrm{con}})^{-1}\boldsymbol{D}^*_{\mathrm{con}}, \\ \boldsymbol{C}_{cl} &= \boldsymbol{C}_{\mathrm{con}} + \boldsymbol{D}^g_{\mathrm{con}}(\boldsymbol{G}^{-1} - \boldsymbol{D}^{\mathrm{g}}_{\mathrm{con}})^{-1}\boldsymbol{C}_{\mathrm{con}}, \\ \boldsymbol{D}_{cl} &= \boldsymbol{D}^*_{\mathrm{con}} + \boldsymbol{D}^g_{\mathrm{con}}(\boldsymbol{G}^{-1} - \boldsymbol{D}^{\mathrm{g}}_{\mathrm{con}})^{-1}\boldsymbol{D}^*_{\mathrm{con}}. \end{aligned}$$

The closed-loop system model corresponding to Fig. 2.2 is shown in Fig. 2.5.

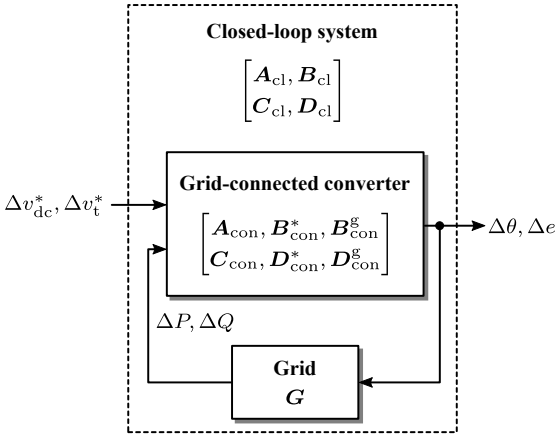

Fig. 2.5: Closed-loop system model of the grid-connected power converter, of which the input includes the references of the outer controllers and the output is the converter internal voltage.

2.3 Model Verification

The proposed model is validated in the system as shown in Fig. 2.2 by simulations in PSCAD/EMTDC. The system parameters are given in Table 2.1. At t = 2 s, the DC-link voltage reference increases by 10%. The dynamic of the proposed model and the time-domain simulation results are shown in Fig. 2.6. It can be seen in Fig. 2.6 that the dynamic of the proposed model matches the time-domain simulation results. It shows that the proposed model is accurate.

Based on the model, the system stability can be analyzed. The closed-loop system eigenvalues when the proportional gain of the PLL ($k_{\mathrm{p\_P}}$) increases from 0.01 to 2 are shown in Fig. 2.7. When $k_{\mathrm{p\_P}}$ increases, the closed-loop eigenvalues move from the right half-plane to the left half-plane. It implies that the system becomes more stable with the increasing $k_{\mathrm{p\_P}}$. To further validate the eigenvalue analysis, the system dynamics when the grid voltage phase angle steps by 45° with $k_{\mathrm{p\_P}}$ = 0.01 and 2 are shown in Fig. 2.8. It shows that the system oscillates after the disturbance. When $k_{\mathrm{p\_P}}$ = 2, the oscillation is damped and the system returns to steady-state after several oscillation periods. However, when $k_{\mathrm{p\_P}}$ = 0.01, the oscillation cannot be damped, which finally becomes divergent. Additionally, the three-phase currents and voltages of the converter under the disturbance when $k_{\mathrm{p\_P}}$ = 2 and 0.01 are shown in Figs. 2.9 and 2.10. It can be observed in Figs. 2.9 that the current and voltage fluctuate with the phase angle change. When $k_{\mathrm{p\_P}}$ = 2, the current and voltage return to the steady-state after a few hundred milliseconds. When $k_{\mathrm{p\_P}}$ = 0.01, the oscillations of the current and voltage cannot be suppressed. Then, periodical oscillations emerge, and the system becomes unstable.

Table 2.1: Parameters of the Grid-Connected Power Converter System in Fig. 2.2. Source: [C1].

Parameter	Description	Value
P_{rated}	Rated PV power	20 kW
v_{dc}^*	Rated DC-link voltage	780 V
v_{t}^*	Rated line to line AC voltage	400 V
C_{dc}	DC-link capacitor	10 mF
L_{f}	Converter filter inductance	2.53 mH
L_{g}	Grid inductance	2.53 mH
f^*	Rated frequency	50 Hz
$(k_{\text{p\_dc}},\ k_{\text{i\_dc}})$	PI coefficients for DC-link voltage controller	(0.5, 50)
$(k_{\text{p\_t}},\ k_{\text{i\_t}})$	PI coefficients for terminal voltage controller	(0.5, 50)
$(k_{\text{p\_P}},\ k_{\text{i\_P}})$	PI coefficients for PLL	(50, 10000)

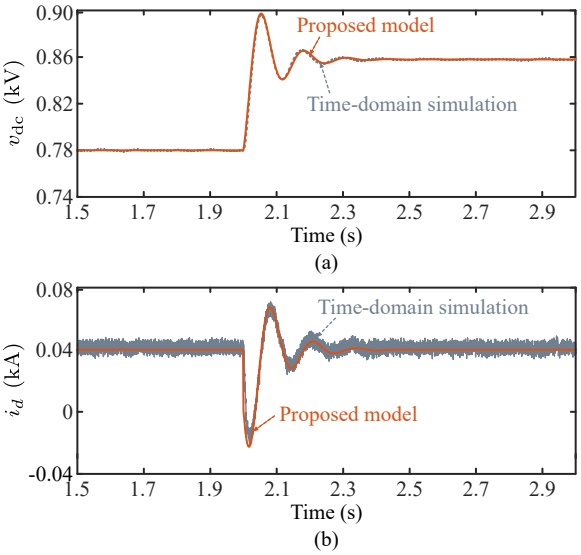

Fig. 2.6: Dynamic of the proposed model and the time-domain simulation results with a DC-link voltage reference step at t = 2 s: (a) DC-link voltage and (b) d-axis current. Source: [C1].

The simulation results indicate that the system is unstable with $k_{\text{p\_P}} = 0.01$. The results agree with the eigenvalue analysis and further the proposed model. Thus, the model can properly reflect the PIV characteristics. In turn, it is effective to evaluate the stability of the grid-connected power converter and further the entire system.

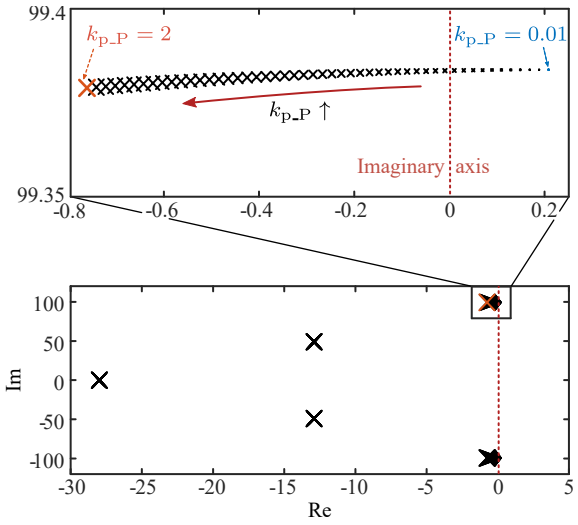

Fig. 2.7: Closed-loop eigenvalues of the system when $k_{\text{p\_P}}$ increases from 0.01 to 2. Source: [C1].

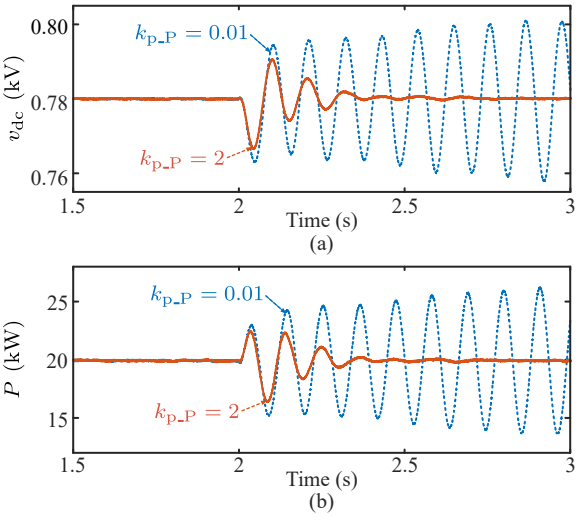

Fig. 2.8: Dynamics of the system with a phase angle change of 45° at t = 2 s when $k_{\text{p\_P}}$ = 0.01 and 2. Source: [C1].

2.4 Summary

In this chapter, the PIV model of grid-connected power converters based on the open-loop modeling method is discussed. The basic concept is to model the power converters with identical external interfaces, which can provide the same information to the grid without incorporating the grid pa-

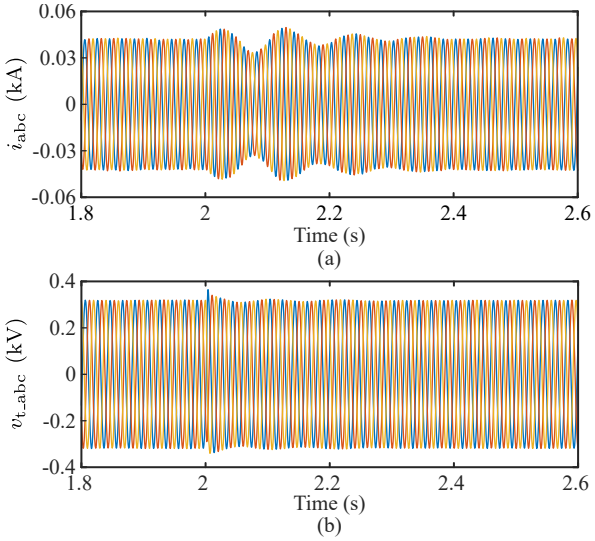

Fig. 2.9: Three-phase current and voltage of the converter with a phase angle change of 45° at t = 2 s when k_{p_P} = 2: (a) three-phase current and (b) three-phase voltage.

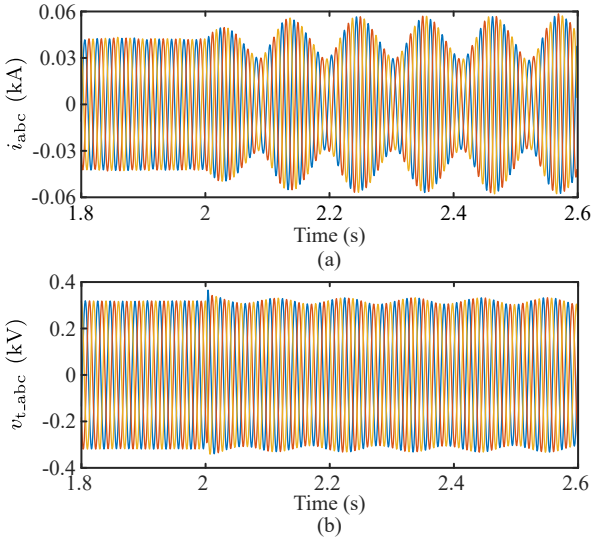

Fig. 2.10: Three-phase current and voltage of the converter with a phase angle change of 45° at t = 2 s when k_{p_P} = 0.01: (a) three-phase current and (b) three-phase voltage.

rameters into the converter model. Specifically, regardless of the controller reference, the input of the open-loop models of the power converters is the power at the PCC. The output is the internal voltages of power converters.

As for the grid, the input and the output are the opposite. In this way, the open-loop models of the power converters and the grid are decoupled. Aggregating the open-loop models with identical external interfaces obtains the closed-loop system model. Moreover, the model can reflect the PIV characteristics of power converters. It provides possibilities for further inertia analysis. The proposed model has been validated by time-domain simulation results, where the system stability is analyzed.

Related Publications

J1. **Q. Peng**, Q. Jiang, Y. Yang, T. Liu, H. Wang, and F. Blaabjerg, "On the Stability of Power Electronics-Dominated Systems: Challenges and Potential Solutions," *IEEE Trans. Ind. App.*, vol. 55, no. 6, pp. 7657–7670, Nov.-Dec. 2019.

C1. **Q. Peng**, Y. Yang, and F. Blaabjerg, "State-Space Modeling of Grid-Connected Power Converters Considering Power-Internal Voltage Characteristics," in *Proc. IEEE ICPE 2019 - ECCE Asia*, Busan, Korea, May 2019, pp. 3047–3053.

Chapter 3

Stability Analysis with Virtual Inertia Provision

This chapter will discuss the impact of virtual inertia provision from DC-link capacitors on system stability. In turn, the virtual inertia control will be properly designed. Subsequently, the maximum virtual inertia from the DC-link capacitor with maintaining system stability can be identified.

3.1 Introduction

In Chapter 2, the PIV model of grid-connected power converters is presented. Based on the model, the inertia characteristics of power converters can be revealed. However, the effective inertia that can support the grid frequency should be particularly discussed. In other words, the generalized inertia can be obtained according to the relationship between the power and the internal voltage. However, it may not contribute significantly to the frequency regulation if the frequency-power regulation strategy is not properly modified at the RMT. In this case, seen from the perspective of the grid, the virtual inertia provided by the power converter is weak. To effectively enhance the inertia of the power electronics-based systems, the inertia emulation strategies should be developed.

In conventional SGs, the mechanical inertia of the rotors decides the power-frequency relationship. When the grid frequency is governed by the SG, the motion of the rotors can be expressed by the swing equation as [6]

$$\begin{cases} P_{\mathrm{m}} - P_{\mathrm{e}} = 2H\dfrac{d\omega_{\mathrm{g}}}{dt} + D(\omega_{\mathrm{g}} - \omega^*) \\ \dfrac{d\theta_{\mathrm{g}}}{dt} = \omega_{\mathrm{g}} - \omega^* \end{cases}, \tag{3.1}$$

where P_e and P_m are the electromagnetic power and the mechanical power, ω_g and ω^* are the SG frequency and the rated frequency, θ_g is the internal voltage phase angle of the SG, and H and D are the inertia constant and the damping gain of the rotor, respectively.

It can be seen in (3.1) that the power and the frequency have a second-order droop relationship due to the rotor inertia. Thus, to emulate the inertia by power electronics, the regulated power should be proportional to the frequency deviation. In the literature, one popular solution is to modify the control strategies of power converters to achieve second-order power-frequency droop characteristics, including the VSG [40], VSM [41], and the electronic synchronous machine (eSM) [88], etc. The power converters with those control methods can provide considerable inertia to the grid. However, they are highly dependent on the large-capacity ESSs. Inspired by this, the inertia emulation from the DC-link capacitors emerges, which can become a universal solution for grid inertia enhancement. Notably, as a universal solution, it preferably decouples with the basic control strategies of the power converters; otherwise, the general application in large-scale power grids may be limited. For instance, a virtual synchronous control of power converters was proposed in [87] to emulate inertia by DC-link capacitors. However, the DC-link capacitor is also used for grid-synchronization. Thus, in this control strategy, the inertia emulation cannot be a plug-in function for general applications. The universal inertia emulation solution from the DC-link capacitors is demonstrated in [46–49], where the VIC is an addition to the basic control strategies of power converters. However, the proper design of the VIC of DC-link capacitors considering the system stability has been barely discussed. It is usually designed according to the steady-state condition of the power converter, including the DC-link capacitor size, the rated DC-link voltage, and the frequency deviation limitation. The dynamics of control loops, e.g., the DC-link voltage controller and the PLL, have not been considered.

The mechanical inertia of rotors is generally 2$\sim$10 s [6]. Thus, the mechanical inertia of rotors regulates the frequency at a relatively large timescale, referring to as the RMT. Consequently, the effective virtual inertia of power converters that can profitably support the grid frequency should be identified at the RMT. However, the VIC of DC-link capacitors inevitably affects the dynamics of the power converter at the timescales faster than the RMT, e.g., the VCT, where the DC-link voltage controller and the PLL are at. If the VIC is designed without considering the dynamics at those timescales, it may result in an unstable system. In turn, in a pre-designed power converter, the dynamic of the basic control system constrains the maximum inertia that the DC-link capacitor can provide. In such a case, the VIC design issue becomes the maximum inertia identification of the DC-link capacitor under given operation conditions. More specifically, the VIC should be designed at the VCT or the CCT, and the inertia is then identified at the RMT.

To tackle this issue, the analysis at multiple timescales is demanded, which requires proper modeling and analysis methods. The PIV model proposed in Chapter 2 can be adopted by additionally considering the multi-timescale characteristics of power converters. On one hand, the PIV model can provide the inertia information of a power converter to the grid, based on which the effective inertia at the RMT can be conveniently identified. On the other hand, the PIV models at different timescales (as submodels) can be conveniently connected to each other, as they have identical external characteristics. For various purposes, different submodels can be adopted. For instance, the stability analysis can be carried out by the submodel at the VCT, based on which the VIC of the DC-link capacitor can be designed. Then, the maximum inertia provision from the DC-link capacitor is identified by the submodel at the RMT.

Considering the above, the multi-timescale PIV model of power converters and the maximum inertia identification method of DC-link capacitors are developed in this chapter. In this chapter, the stability at the VCT will be concentrated on to properly design the VIC of DC-link capacitors.

3.2 Inertia Provision from DC-Link Capacitors

As aforementioned, when the inertia emulation is required for a power generating unit, its output power should be regulated in proportion to the derivative of the frequency (RoCoF). For a DC-link capacitor, the relationship between its voltage and power is given as

$$P_{\text{in}} - P = C_{\text{dc}} v_{\text{dc}} \frac{dv_{\text{dc}}}{dt}, \tag{3.2}$$

where v_{dc} is the DC-link voltage, C_{dc} is the DC-link capacitance, and P_{in} and P are the active power from the DC side and flowing to the converter after the DC-link capacitor. Without considering the power loss of the converter, P is the converter output power to the grid. It can be seen in (3.2) that the DC-link voltage and the active power absorbed/released by the DC-link capacitor have the second-order droop relationship. Thus, if the DC-link voltage can be regulated to be proportional to the frequency, the second-order power-frequency droop relationship can be established. Consequently, the virtual inertia can be emulated. To achieve so, the VIC should be added on the basic DC-link voltage controller as [J2]

$$v_{\text{dc}}^{f} = k_{\omega v} \omega, \tag{3.3}$$

with ω being the grid frequency, v_{dc}^{f} being the additional DC-link voltage reference, and $k_{\omega v}$ being the frequency-voltage (DC-link voltage) droop gain.

When the RMT is focused on, the dynamic of the DC-link voltage controller can be ignored, i.e., it is assumed that it can track the reference immediately. In this case, the relationship between the active power flowing through the converter and the grid frequency can be obtained as [J2]

$$P_{\text{in}} - P = C_{\text{dc}} v_{\text{dc}}^{*} k_{\omega v} \frac{d\omega}{dt}, \tag{3.4}$$

with v_{dc}^{*} being the rated DC-link voltage. Accordingly, inertia emulated by the DC-link capacitor is

$$H_v = \frac{1}{2} C_{\text{dc}} v_{\text{dc}}^{*} k_{\omega v}. \tag{3.5}$$

For a pre-designed power converter, C_{dc} and v_{dc}^{*} are settled already. Then, the virtual inertia from the DC-link capacitor is determined by $k_{\omega v}$. When considering the converter stability at the RMT, the design of $k_{\omega v}$ is constrained by the steady-state deviation limits of the DC-link voltage and the grid frequency, according to (3.3). However, when considering the converter stability at the VCT, the dynamics of the basic control loops also constrain the design of $k_{\omega v}$. First, the DC-link voltage does not immediately follow v_{dc}^{f} in (3.3) at this timescale. Moreover, the frequency for the VIC in (3.3) is measured by the PLL. Hence, tuning $k_{\omega v}$ should consider the dynamics of the DC-link voltage controller and the PLL.

To identify the maximum virtual inertia from the DC-link capacitor considering the system stability at the VCT, a multi-timescale model is required, which should contain two submodels at the VCT and the RMT, respectively. The submodel at the VCT is applied to tune $k_{\omega v}$, which maintains the converter stability at the VCT. The maximum effective virtual inertia from the DC-link capacitor can then be identified by the submodel at the RMT.

3.3 Maximum Virtual Inertia Design

3.3.1 Multi-Timescale Model

The multi-timescale PIV model of power converters will be proposed in this section to design the VIC and further identify the maximum virtual inertia from the DC-link capacitor. As the dynamic of the CCT is not considered in this chapter, the multi-timescale will include the submodels at the VCT and the RMT. To achieve so, the PI loops at the faster timescale can be ignored, as seen from the perspective of the slower timescale, they are considered to be sufficiently fast to track the references. Furthermore, the submodels at different timescales have identical external interfaces. In this way, the concerned features of the submodels can be maintained when the submodel is simplified to a slower timescale.

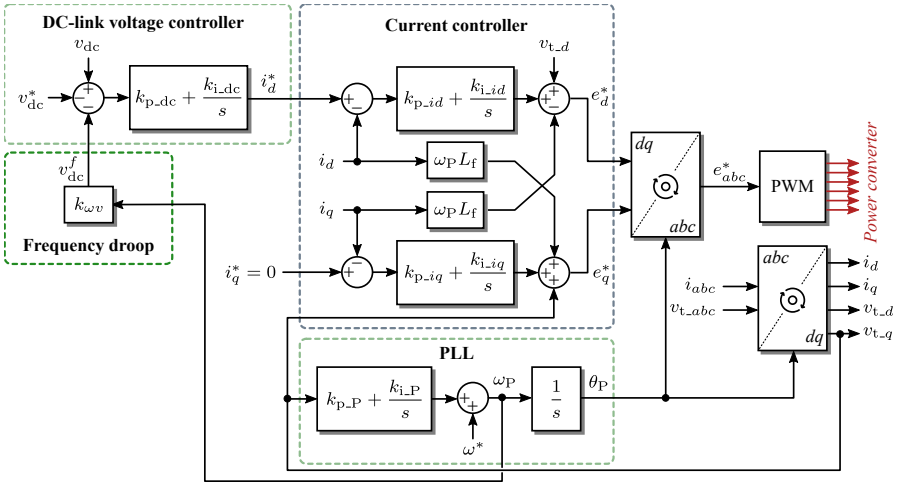

Fig. 3.1: Dual-loop current control of a grid-connected power converter with VIC of the DC-link capacitor, where the definitions of variables are identical with those in Chapter 2. Source: [J2].

The dual-loop control strategy introduced in Chapter 2 is also implemented in this chapter as the basic control. As this chapter focuses on the inertia emulation, the terminal voltage controller is ignored, where the q-axis current reference is zero. Additionally, the VIC of the DC-link capacitor, i.e., the frequency-voltage droop loop is implemented. The control system is shown in Fig. 3.1.

The converter sub-model at the VCT is the same as that illustrated in Chapter 2. Notably, the VIC of the DC-link capacitor is added while the reactive power control loop is removed. The small signal model of the VIC of the DC-link capacitor, i.e., the frequency-voltage droop loop, is obtained according to (3.3) as

$$\Delta v_{\mathrm{dc}}^{f} = k_{\omega v} \Delta \omega_{\mathrm{P}}. \tag{3.6}$$

With the VIC and without the terminal voltage controller, the small signal models of the outer-loop controllers in (2.3) become

$$\begin{cases} \Delta i_d^* = \Delta \varphi_{\mathrm{dc}} + k_{\mathrm{p\_dc}} (\Delta v_{\mathrm{dc}} - \Delta v_{\mathrm{dc}}^* - \Delta v_{\mathrm{dc}}^{\mathrm{f}}) \\ \Delta i_q^* = 0 \end{cases}, \tag{3.7}$$

with the small signal model of the state variable $\Delta \varphi_{\mathrm{dc}}$ becoming

$$\frac{d \Delta \varphi_{\mathrm{dc}}}{dt} = k_{\mathrm{i\_dc}} (\Delta v_{\mathrm{dc}} - \Delta v_{\mathrm{dc}}^* - \Delta v_{\mathrm{dc}}^{\mathrm{f}}). \tag{3.8}$$

The converter open-loop PIV model at the CCT is shown in Fig. 3.2, with respect to Fig. 3.1. In Fig. 3.2, k_{Pv} denotes the gain from the power to the

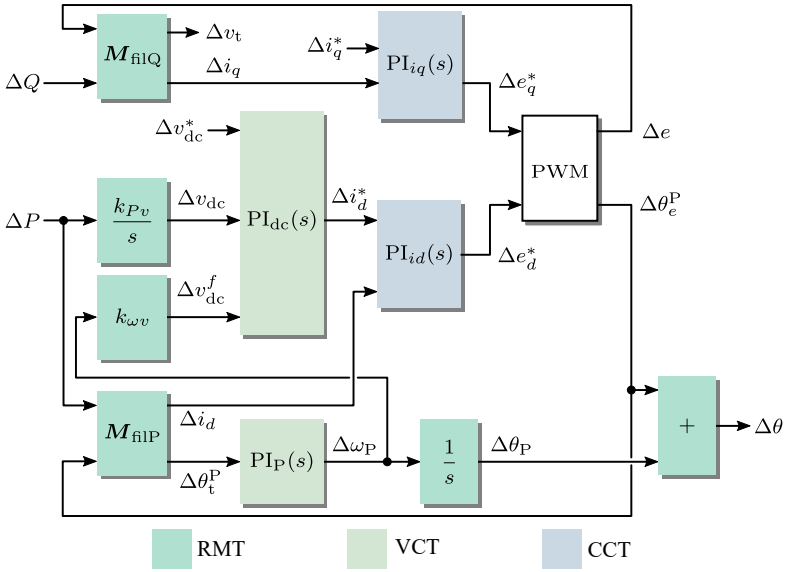

Fig. 3.2: Open-loop PIV model at the CCT of the power converter with respect to Fig. 3.1, where the subscripts of "PI" (i.e., "dc", "P", "*id*" and "*iq*") imply the PI controllers for the corresponding variables. Source: [J2].

DC-link voltage in (2.2) as

$$k_{Pv} = -\frac{1}{C_{\text{dc}} v_{\text{dc0}}}. \tag{3.9}$$

Additionally, in Fig. 3.2, $\boldsymbol{M}_{\text{filP}}$ and $\boldsymbol{M}_{\text{filQ}}$ reveal the filter dynamic, which can be obtained from (2.12) and (2.13) as [J2]

$$\begin{cases} \boldsymbol{M}_{\text{filP}} = \begin{bmatrix} 1 & -\dfrac{X_{\text{f}}}{e_0 v_{\text{t0}}} \\ \dfrac{e_0 - v_{\text{t0}}}{X_{\text{f}}} & \dfrac{1}{e_0} \end{bmatrix} \\ \boldsymbol{M}_{\text{filQ}} = \begin{bmatrix} \dfrac{2e_0 - v_{\text{t0}}}{e_0} & -\dfrac{X_{\text{f}}}{e_0} \\ \dfrac{e_0 - v_{\text{t0}}}{e_0 X_{\text{f}}} & -\dfrac{1}{e_0} \end{bmatrix} \end{cases}. \tag{3.10}$$

Notably, although the current controllers and the modulation loop are presented in Fig. 3.2, the small signal models of them are not detailed, as their dynamics are not the focus of this chapter.

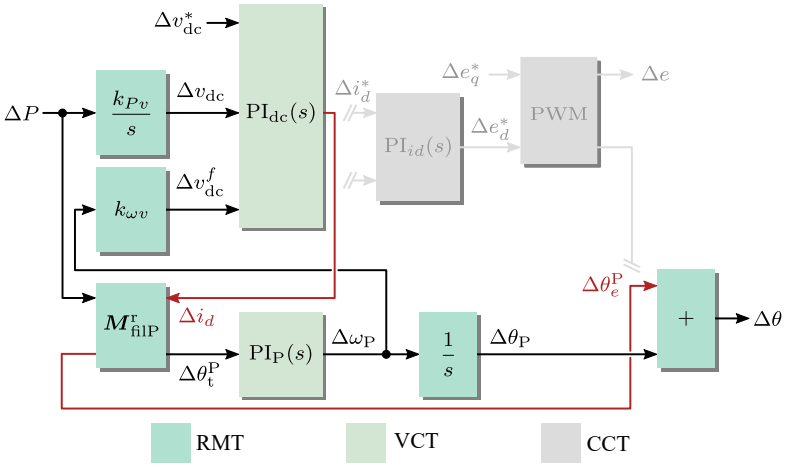

Fig. 3.3: Open-loop PIV model at the VCT of the power converter simplified from Fig. 3.2, where the superscript "r" stands for the changes of inputs and outputs of the module. Source: [J2].

3.3.2 Frequency-Voltage Droop Gain Design at the VCT

As aforementioned, the frequency-voltage droop gain k_{Pv} determines the maximum virtual inertia from the DC-link capacitor in a pre-designed power converter. To identify the maximum inertia with considering the converter stability at the VCT, k_{Pv} should be designed based on the submodel at the VCT. The submodel at the VCT can be simplified from the submodel at the CCT in Fig. 3.2 by ignoring the modules at the CCT, i.e., the current controllers and the modulation loop. To achieve so, it is assumed that the current controllers can track the references immediately, as exemplified in (2.14). When the current controllers are ignored, the inputs and outputs of $\boldsymbol{M}_{\mathrm{filP}}$ will be changed. The open-loop PIV model at the VCT is obtained as shown in Fig. 3.3. Based on the submodel at the VCT, the impact of the inertia emulation from the DC-link capacitor on the system stability can be analyzed. In turn, k_{Pv} can be properly designed considering the system stability.

3.3.3 Virtual Inertia Identification at the RMT

After k_{Pv} is properly designed, the maximum virtual inertia that the DC-link capacitor can provide under certain operation conditions is determined. As the inertia effectively supports the grid frequency at the RMT, it should be identified at the RMT. The submodel at the RMT can be simplified from the one at the VCT as shown in Fig. 3.3 by ignoring the modules at the VCT, i.e., the DC-link voltage controller and the PLL. To achieve so, the DC-link voltage controller is assumed to follow the reference immediately, and the PLL can track the terminal voltage phase angle sufficiently fast. The submodel at the

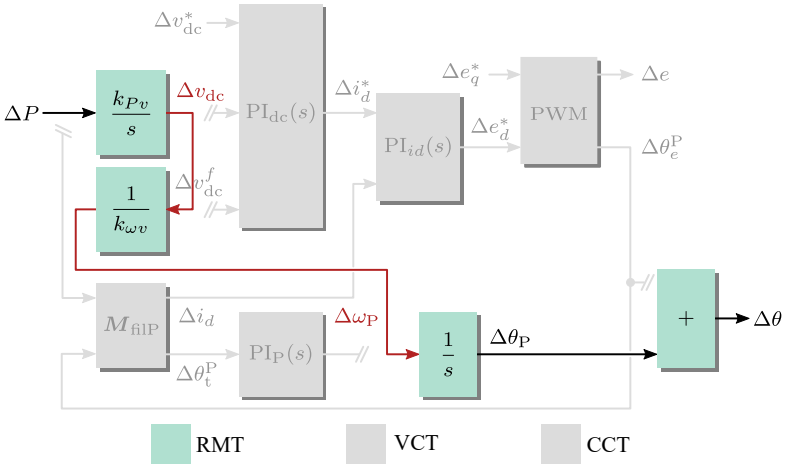

Fig. 3.4: Open-loop PIV model at the RMT of the power converter simplified from Fig. 3.3. Source: [J2].

RMT is obtained as shown in Fig. 3.4. Notably, the module corresponding to the filter dynamic ($\boldsymbol{M}_{\mathrm{filP}}$) is ignored in Fig. 3.4 as well, since its two inputs are invalid in this case. Accordingly, the virtual swing equation of the DC-link capacitor can be formed as [J2]

$$\begin{cases} \Delta P = \dfrac{k_{\omega v}}{k_{Pv}} \cdot \dfrac{d\Delta\omega_{\mathrm{P}}}{dt} \\ \dfrac{d\Delta\theta}{dt} = \Delta\omega_{\mathrm{P}} \end{cases}, \tag{3.11}$$

where ω_{P} equals to the grid frequency, as the dynamic of the PLL is ignored at the RMT. The virtual inertia obtained from (3.11) is identical to the one presented in (3.5), which is the effective virtual inertia that the grid demands.

3.4 Case Study

The proposed multi-timescale model and further the maximum virtual inertia analysis method will be validated in this section. The simulation results in MATLAB/Simulink and experimental results will be given. The configuration of the case-study system is shown in Fig. 3.5. The grid is represented by a VSG to emphasize the frequency dynamic. The system parameters are given in Table 3.1.

3.4.1 Model Validation

First, the model at the VCT will be validated. In this case, the grid in Fig. 2.2 is represented by an infinite-bus system to avoid the effect of the

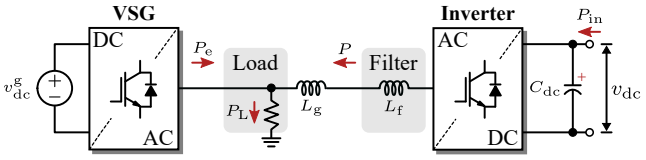

Fig. 3.5: System for stability analysis and frequency regulation, where P_e and P_L are the VSG output power and the load power, and v_{dc}^{g} is the DC-link voltage of the VSG. Source: [J2].

Table 3.1: Parameters of the Grid-Connected Power Converter System in Fig. 3.5. Source: [J2].

Parameter	Description	Value
	VSG	
P_{rated}^{g}	Rated power	2 kW
v_{rated}^{g}	Rated line-to-line grid voltage	400 V
v_{dc}^{g}	Rated DC-link voltage	800 V
R	Speed regulation gain	0.05 p.u.
T_G	Governor time constant	0.2 s
T_T	Turbine time constant	0.3 s
H	Inertia constant	5 s
D	Damping coefficient	1 p.u.
f^*	Rated frequency	50 Hz
L_f^{inv}	Converter-side filter inductance	4.8 mH
L_f^{g}	Grid-side filter inductance	2 mH
C_f^{g}	Filter capacitance	10 μF
L_g	Grid inductance	2 mH
	Inverter	
P_{rated}	Rated power	2 kW
P_{in}	Power from DC source	0 p.u.
v_{dc}^{*}	DC-link voltage reference	800 V
L_f	Filter inductance	5 mH
C_{dc}	DC-link capacitance	2.8 mF
(k_{p_dc}, k_{i_dc})	PI coefficients for DC-link voltage controller	(0.5, 20)
(k_{p_P}, k_{i_P})	PI coefficients for PLL	(0.5, 5)

VSG. The open-loop model of the grid is illustrated in Chapter 2. Connecting the open-loop models of the converter and the grid obtains the closed-loop system model. At t =2 s, the DC-link voltage reference steps by 5%. The dynamics of the mathematical model and the time-domain simulation are

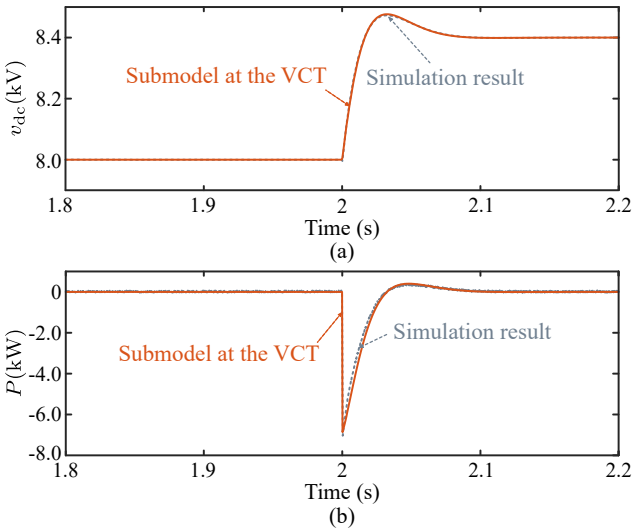

Fig. 3.6: Dynamics of the proposed model at the VCT and the time-domain simulation results, where the system experiences a DC-link voltage reference step of 5%. Source: [J2].

shown in Fig. 3.6. It shows that the proposed model conforms with the simulation results, meaning that the proposed model is accurate.

3.4.2 Maximum Virtual Inertia Identification

Then, the impact of the VIC of the DC-link capacitor on the system stability will be analyzed, based on which $k_{\omega v}$ can be properly designed. To conduct the frequency stability analysis and the frequency regulation, a VSG is implemented to represent the grid. Correspondingly, the system configuration is shown in Fig. 3.5.

Before the stability analysis, the closed-loop system model should be developed. The open-loop model of the grid should be replaced by the open-loop model of the VSG, of which the model is exemplified in (3.1). To obtain the closed-loop system model, the grid model should be developed to aggregate the open-loop models of the inverter and the VSG. The grid small signal model is given as [J2]

$$\begin{bmatrix} \Delta P \\ \Delta P_e \end{bmatrix} = \begin{bmatrix} 0 \\ 1 \end{bmatrix} \Delta P_L + \begin{bmatrix} \dfrac{e_0 v_{g0}}{X_f + X_g} & -\dfrac{e_0 v_{g0}}{X_f + X_g} \\ -\dfrac{e_0 v_{g0}}{X_f + X_g} & \dfrac{e_0 v_{g0}}{X_f + X_g} \end{bmatrix} \begin{bmatrix} \Delta\theta \\ \Delta\theta_g \end{bmatrix}. \tag{3.12}$$

with v_g being the terminal voltage of the VSG and $X_g = 2\pi f_0 L_g$.

Connecting the open-loop models of the inverter and the VSG to the grid model yields the closed-loop system model. Based on the model, the system

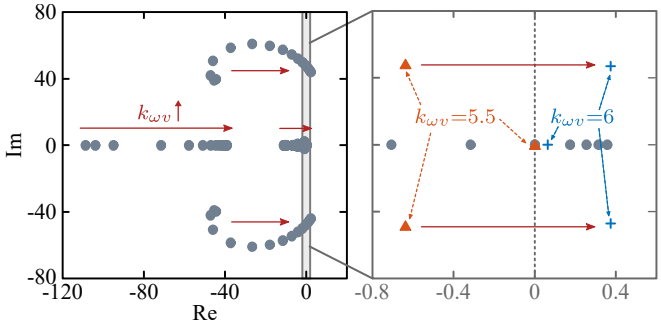

Fig. 3.7: Closed-loop eigenvalues of the system with $k_{\omega v}$ increasing from 0 to 8. Source: [J2].

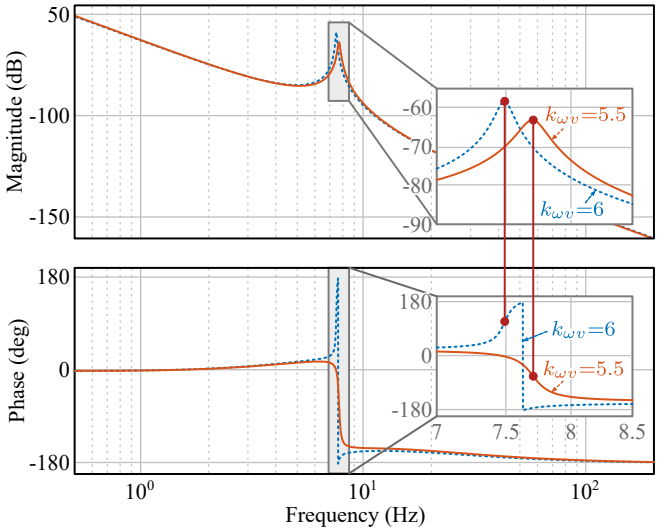

Fig. 3.8: Closed-loop eigenvalues of the system with $k_{\omega v}$ increasing from 0 to 8. Source: [J2].

stability will be analyzed by the eigenvalue analysis and Bode diagrams. The closed-loop eigenvalues of the system when $k_{\omega v}$ increases from 0 to 8 can be obtained, which are shown in Fig. 3.7. It shows that the eigenvalues move across imaginary axis from the left-half plane with increasing $k_{\omega v}$, implying that the system is being more unstable. Notably, when $k_{\omega v}$ increases from 5.5 to 6, the eigenvalues move across the imaginary axis, indicating that $k_{\omega v}$ should not exceed 5.5 to maintain system stability. Additionally, the Bode diagrams when $k_{\omega v}$ = 5.5 and 6 are presented in Fig. 3.8. It shows that there is a resonance peak around 7.5 Hz when $k_{\omega v}$ = 5.5 or 6. When $k_{\omega v}$ = 5.5, the phase margin of the resonance peak is positive, whereas it becomes negative when $k_{\omega v}$ = 6. This is in accordance with the eigenvalue analysis results, i.e., the maximum $k_{\omega v}$ that can maintain the system stability is 5.5.

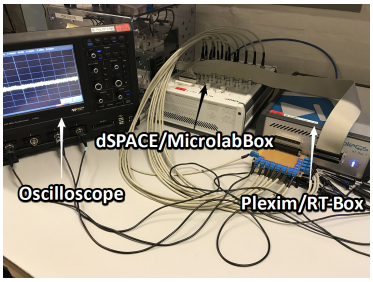

Fig. 3.9: Experimental setup of the grid-connected converter.

To further validate the stability analysis, the experiments are carried out. The experimental setup consists of a real-time simulator (Plexim/RT-Box) and a digital control platform (dSPACE/MicroLabBox), as shown in Fig. 3.9. The dynamics of the system under a 10%-load step with $k_{\omega v}$ being 0, 5.5, and 6 are shown in Fig. 3.10. It shows that when the load step occurs, the grid frequency starts to decrease. When $k_{\omega v} = 0$, the DC-link capacitor barely responds to the disturbance to support the grid frequency. When $k_{\omega v} = 5.5$, the DC-link capacitor releases power in response to the decreasing grid frequency. When $k_{\omega v} = 6$, the DC-link capacitor also releases power under the disturbance. However, the system oscillates after the disturbance in this case, indicating an unstable system. The experimental results verify the eigenvalue analysis results and the Bode diagram. That is, $k_{\omega v} = 5.5$ is the limit of the VIC of the DC-link capacitor considering the system stability.

With the properly designed $k_{\omega v}$, the maximum virtual inertia can be identified. According to (3.5), the virtual inertia when $k_{\omega v} = 5.5$ is 2.47 s. The dynamics of the systems where the inertia (2.47 s) is provided by the inverter or the VSG are shown in Fig. 3.11, where a 10%-load step is applied. It shows that the system dynamics agree with each other. Thus, the identified virtual inertia is accurate.

3.5 Summary

In this chapter, the analysis method of the VIC of the DC-link capacitors in pre-designed power converters is proposed. The analysis is based on a multi-timescale PIV model of power converters. It consists of several submodels at different timescales, which can be flexibly adopted for various purposes. First, the submodel at the VCT is employed for stability analysis of the power converter with the VIC of the DC-link capacitor. The frequency-voltage (DC-link voltage) droop gain ($k_{\omega v}$), which determines the effective virtual inertia, is properly designed according to the stability analysis. Then, the effective virtual inertia is identified based on the submodel at the RMT. The identified

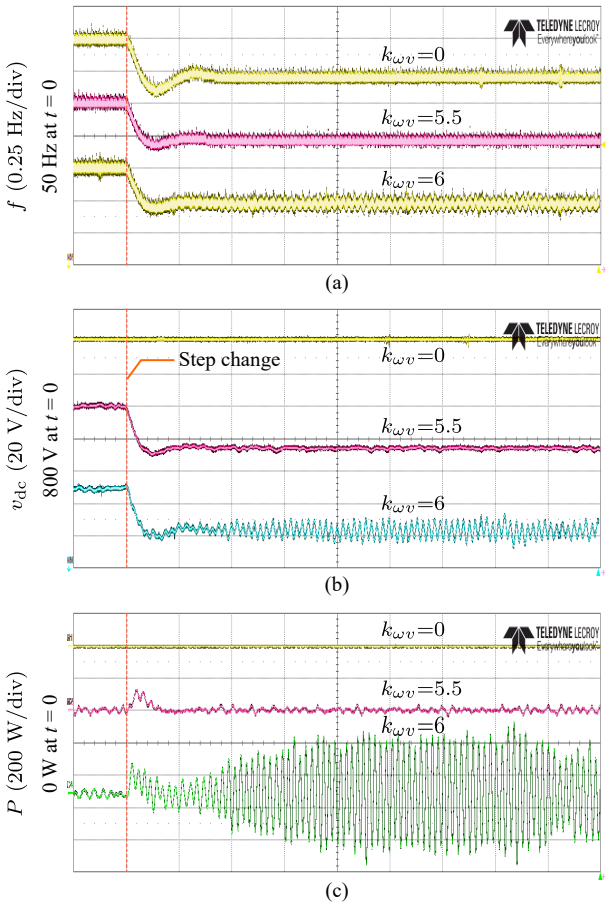

Fig. 3.10: Experimental results under a 10%-load step with $k_{\omega v}$ being 0, 5.5, and 6 (time [2 s/div]): (a) frequency, (b) inverter DC-link voltage, and (c) inverter output power. Source: [J2].

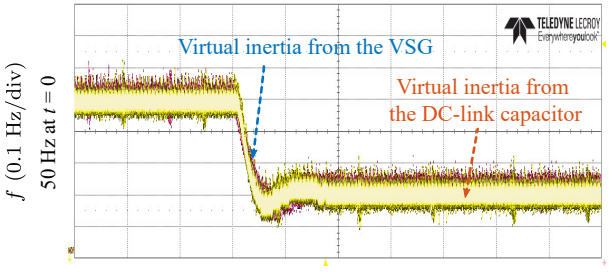

Fig. 3.11: Experimental results for inertia validation (time [2 s/div]). Source: [J2].

maximum virtual inertia clarifies the grid frequency support capability of the power converter. It can be beneficial to the inertia enhancement and optimization in power systems in the planning and operation phases.

Related Publications

J2. **Q. Peng**, J. Fang, Y. Yang, T. Liu, and F. Blaabjerg, "Maximum Virtual Inertia from DC-Link Capacitors Considering System Stability at Voltage Control Timescale," *IEEE J. Emerg. Select. Topics Circuits Syst.*, Status: Under Review.

Chapter 4

Power Reserve Control for Frequency Support

This chapter will address the PRC of PV systems. The periodical control strategy will be designed to measure MAP and achieve the power reserve. The control signals will be designed to coordinate the PRC and VIC of PV systems.

4.1 Introduction

In previous chapters, the general analysis and control tools in power electronics-based systems have been introduced. With the general tools, the method to emulate inertia from the DC-link capacitors can become an effective and universal solution for inertia enhancement of the system. However, the virtual inertia is limited by the DC-link capacitance, which is not sufficient in certain cases. For instance, when the system suffers from very severe disturbances, much support will be demanded. In this regard, inertia emulation from large-scale power generating units, e.g., RESs should be explored.

The PV system with flexible power regulation capability is a potential virtual inertia supplier. When the frequency support is demanded by the grid, the PV power can be flexibly regulated to attenuate the power imbalance and stabilize the grid frequency. Conventionally, operating at the MPP is expected by the PV systems. The power-voltage (P-V) characteristic of a PV panel is shown in Fig. 4.1. It shows that the P-V curve is non-monotonic with a peak, i.e., the MPP. Thus, to maximize the energy yield, the PV system is usually controlled to operate at the MPP. The Perturb & Observe (P&O) MPPT is the most widely-applied algorithm [89]. By applying a perturbation to the PV system and then observing the PV power change, the reference

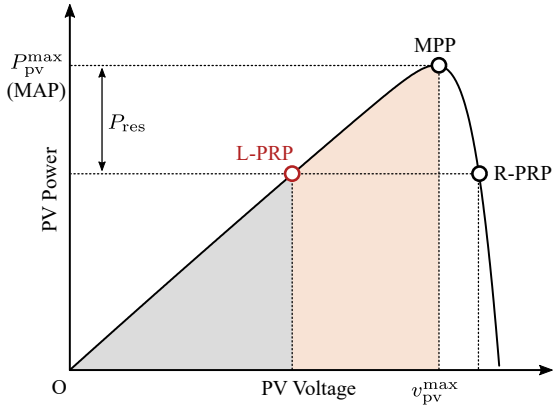

Fig. 4.1: P-V curve of a PV panel with power reserve, with $P_{\mathrm{pv}}^{\max}$ being the maximum PV power, $v_{\mathrm{pv}}^{\max}$ being the corresponding PV voltage, and P_{res} is the power reserve. Source: [J4].

direction for the next MPPT period can be corrected. After several periods, the MPP can be tracked, and the PV output power is accordingly maximized.

When the PV system operates at the MPP, it can reduce the output power when needed. However, it cannot release more power when the power generation is not sufficient to supply the load. Thus, to achieve full-range frequency support to the grid, including the under-frequency and over-frequency supports, the PV system should not constantly operate at the MPP. Instead, the power reserve is desired for a more grid-friendly PV system. In such a case, the PV system will operate at the power reserve point (PRP), as shown in Fig. 4.1. It shows that the PV system may operate at the left-PRP (L-PRP) or the right-PRP (R-PRP) due to the non-monotonic P-V characteristic. To avoid sudden PV power loss due to the more sensitive P-V relationship, the L-PRP is usually selected for PV systems with power reserve [50, 74]. Notably, in two-stage configuration of PV systems, the boost converter will accelerate the PV voltage to reach the DC-link voltage requirement. Thus, the lower PV voltage (corresponding to L-PRP) is allowable [54].

Notably, before controlling the PV system to operate at the L-PRP, the MAP should be measured at first. Then, the L-PRP can be located based on the MAP. However, the MAP is changing during operation, as the environmental condition is varying, as shown in Fig. 4.2. More specifically, when the irradiance decreases, the MAP and the corresponding PV voltage will reduce. When the temperature increases, the MAP will have similar movement. In this context, the MAP measurement becomes a challenge. Currently, there are several solutions to this issue. Some of them depend on environmental sensors or particular PV system configurations (e.g., master-slave configuration). Some have requirements on computation (e.g., curve-fitting methods), or they are highly model-dependent. Those MAP measurement methods in-

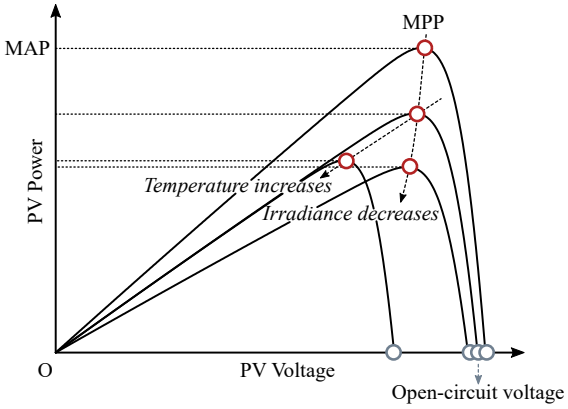

Fig. 4.2: MAP movement of a PV system when irrandiance or temperature changes. Source: [J3].

troduce additional costs to the PV system, or may not accurately obtain the MAP considering system degradation. which requires other attempts.

Aiming at this issue, an event-triggering PRC of PV systems is introduced in this chapter to achieve frequency support. It is independent of additional hardware and it is not computation-heavy. The MAP will be measured in real-time by an MPPT algorithm, where the estimation error can be minimized. The coordination of the PRC and VIC of PV systems will be developed, which is barely addressed in the literature.

4.2 Power Reserve Control

4.2.1 Control Principle

The PRC is periodical, where the MPPT algorithm (P&O-MPPT is adopted in this chapter) is executed at the beginning of every PRC cycle to measure the MAP. Thus, this is also referred to as the MPPT-PRC. Once the MAP is measured, the PV system turns to the power reserve mode. The operation point will move from the MPP to the PRP (L-PRP is preferable). In this way, the real-time MAP can be measured. The principle of the PRC is demonstrated in Fig. 4.3, where two sequential PRC cycles with decreasing irradiance are presented. As shown in Fig. 4.3, the PV system starts to operate at A (i.e., the MPP under this environmental condition). Considering the power reserve, the PV system moves to B (i.e., the L-PRP in this cycle), which is located according to the measured MAP. Then, the next PRC cycle begins. The operation point changes to C due to the irradiance decrease. Meanwhile, the MPPT is applied again. It makes the PV system move to D, i.e., the MPP under this environmental condition. Once the MAP is measured, the operation

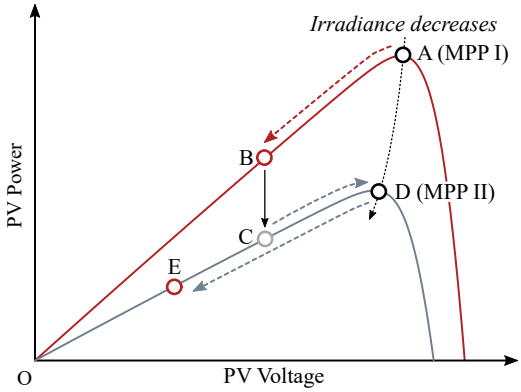

Fig. 4.3: Principle of the MPPT-PRC in two sequential control cycles with decreasing irradiance. Source: [J4].

changes to the power reserve mode again, and the operation point moves to E, where the PV system will wait for the next PRC cycle. It should be mentioned that the PRC frequency, i.e., how often the MPPT is executed, affects the performance of the PRC, as the measured MAP will be used to locate the PRP within the entire PRC cycle, even when the irradiance has changed. Thus, the PRC frequency should be carefully designed, which should take the environment condition and the PV system scale, etc., into account. Another attention is that the significant MPP changes due to seldom passing clouds are usually for short duration [90]. Thus, the irradiance and temperature are assumed to be approximately invariable during the PRC operation, which is viable in practice.

4.2.2 Transient Power Damping Control

In the periodical execution of the MPPT algorithm, an issue emerges, i.e., the inevitable transient power generated by the MPPT, as shown in Fig. 4.4. It shows that the execution of the MPPT algorithm makes the PV power increase until the MAP is measured. Moreover, after the MAP is measured, the operation point cannot move to the PRP immediately, which also generates transient power. Consequently, the PV power quality will become poor, and the grid stability may be challenged.

To solve this problem, the transient power should be damped, and the DC-link capacitor can be a solution. Specifically, a transient power damping control (TPDC) can be implemented to the basic DC-link voltage controller. When the PV power exceeds the reference, i.e., the reserved PV power of the last PRC cycle, the DC-link voltage will increase to absorb the excess energy. Then, the stored energy will be gradually released to the grid, which

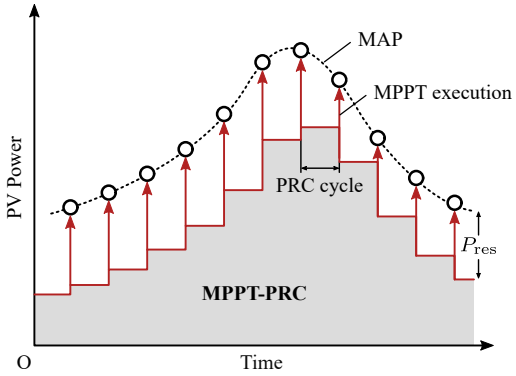

Fig. 4.4: PV system output power under the MPPT-PRC. Source: [J4].

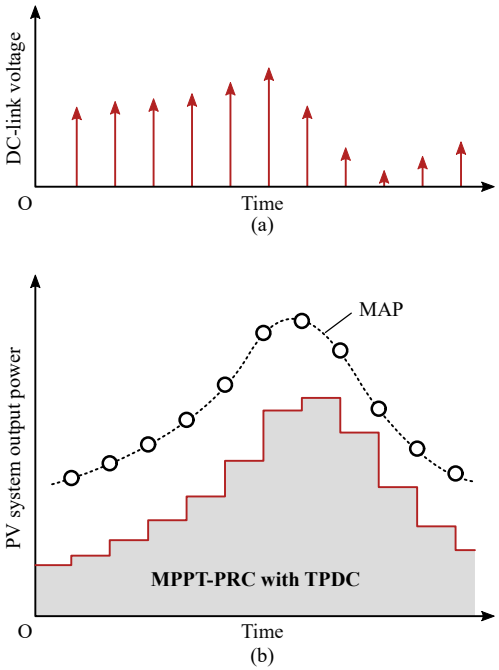

Fig. 4.5: PV system dynamic with the TPDC in the MPPT-PRC: (a) DC-link voltage and (b) PV system output power. Source: [J4].

will not significantly impact the grid stability. The principle of the TPDC is shown in Fig. 4.5. With the TPDC, the DC-link voltage increases during the execution of the MPPT algorithm. That is, the DC-link capacitor stores the excess power generated by the MPP tracking. In this way, although the transient power pulses of the PV power still exist, the PV system output power is much smoothed.

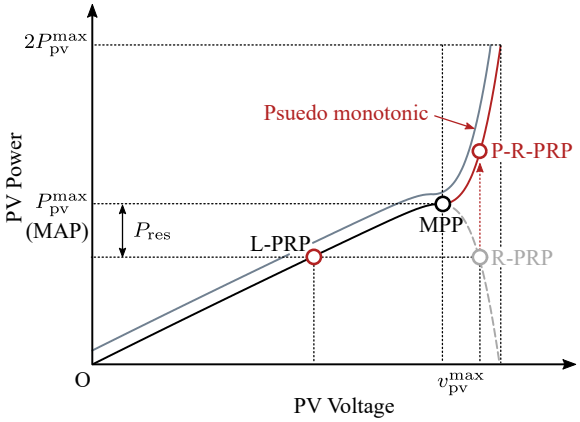

Fig. 4.6: Pseudo monotonic P-V curve in the MPPT-PRC, where P-R-PRP stands for the pseudo R-PRP. Source: [J4].

4.2.3 Monotonic Power-Voltage Curve

As aforementioned, the P-V curve of a PV system is non-monotonic. Thus, there are two PRPs corresponding to the same PV power. It becomes difficult to control the PV system to operate at the L-PRP by setting the PV power reference. If no action is taken for the PV power controller, the PV system may oscillate between the L-PRP and the R-PRP. To make the PV system steadily operate at the L-PRP, a pseudo-monotonic P-V curve is designed, as shown in Fig. 4.6. The main concept is to give the PI controller of the boost converter the pseudo information about the PV power. Then, a power reserve reference will map only one operation point. For instance, when the PV system operates at the R-PRP, the PV power controller will think that the PV system operates at the P-R-PRP. As a result, the controller will move the PV system to the L-PRP.

4.3 Virtual Inertia Control

4.3.1 Basic Concept

Based on the PRC, the PV systems can support the grid frequency in full-range. Thus, the VIC of PV systems is developed in this section, and its coordination with the MPPT-PRC will be demonstrated. As discussed in Chapter 3, to provide virtual inertia, the PV power should be regulated in proportion to the derivative of the frequency (RoCoF). Accordingly, the VIC

of the PV system is designed as [J4]

$$P_{\mathrm{pv}}^{\mathrm{VIC}} = 2H_{\mathrm{pv}}\frac{d\omega}{dt}, \tag{4.1}$$

with $P_{\mathrm{pv}}^{\mathrm{VIC}}$ being the additional PV power reference for VIC and H_{pv} being the virtual inertia provided by the PV system. Notably, the RoCoF for the VIC implementation is directly acquired from the system operator. Thus, the RoCoF measurement will not be illustrated in this chapter. Additionally, the maximum virtual inertia should be constrained by the RoCoF limitation and the power reserve of the PV system [J4], i.e.,

$$H_{\mathrm{pv}}^{\max} = \frac{P_{\mathrm{res}}/P_{\mathrm{rated}}}{2\frac{d\omega_{\mathrm{t}}}{dt}/\omega_0}, \tag{4.2}$$

in which $\frac{d\omega_{\mathrm{t}}}{dt}$ is the RoCoF threshold according to the grid code, ω_0 and P_{rated} are the rated frequency and PV power.

4.3.2 Control Logic Design

To reasonably coordinate the PRC and the VIC of the PV systems, the event-triggering signal should be properly designed. It controls the PV system to switch between the MPPT mode and the power reserve mode. It includes the VIC enabling signal, the MPPT execution signal, and the MAP detection signal. Those are defined as follows [J4].

- VIC enabling signal: This signal is to decide if the VIC should be activated. In steady-state, the VIC enabling signal is "0", which turns to "1" when the grid frequency exceeds the pre-set limit. Once the frequency is detected to be back to the nominal state, the VIC enabling signal turns to "0", disabling the VIC loop.
- MPPT execution signal: It controls the execution of the MPPT algorithm at the beginning of each PRC cycle. When the signal is "1", the MPPT algorithm is activated to measure the MAP. When the signal is "0", the MPPT algorithm is disabled. The MPPT execution signal is a square waveform, of which the frequency equals to the PRC frequency.
- MAP detection signal: This signal is to detect if the MAP is measured. When the signal is "0", it denotes that the MAP has not been measured. When the MAP is measured, the signal becomes "1". Once the MAP detection signal changes from "0" to "1", the MPPT algorithm will be deactivated and the PV system will switch to the power reserve mode.

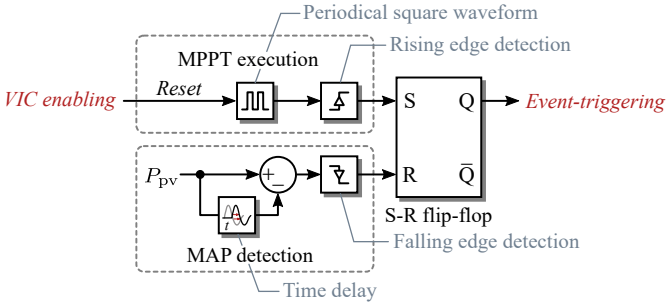

Fig. 4.7: Formation of the event-triggering signal. Source: [J4].

Notably, the VIC enabling signal governs the MPPT execution. To avoid conflict, the MPPT-PRC (including the TPDC) is disabled when the VIC is active. Furthermore, the negative MPPT execution signal resets the MAP detection signal ensure it can successfully generate a falling edge when the MAP is measured. The formation of the event-triggering signal is shown in Fig. 4.7. It shows that the signal is produced by an S-R flip-flop. When the MPPT execution signal turns from "0" to "1", the event-triggering signal is "1", switching the PV system to the MPPT mode. Once the MAP is detected, the MAP detection signal turns from "1" to "0", which makes the PV system change to the power reserve mode.

4.3.3 Entire Control System

The entire control system of the PV system, including the MPPT-PRC and the VIC, is shown in Fig. 4.8, where the VIC loop is constructed by (4.1). Moreover, the DC-link controller with the TPDC is given as [J4]

$$i_d^* = [v_{\mathrm{dc}}^* - v_{\mathrm{dc}} - k_{Pv}(v_{\mathrm{pcc}} i_{\mathrm{pcc}} - P_{\mathrm{pv}}^{\mathrm{PRC}})](k_{\mathrm{p\_dc}} + \frac{k_{\mathrm{i\_dc}}}{s}), \tag{4.3}$$

in which the definitions of variables are identical with those in Chapter 2, and k_{Pv} being the power-voltage droop gain for the TPDC. Additionally, the maximum k_{Pv} is constrained by

$$k_{Pv}^{\max} = \frac{v_{\mathrm{dc}}^{\max} - v_{\mathrm{dc}}^*}{P_{\mathrm{res}}} \cdot \frac{1}{k_{\mathrm{p\_dc}}}, \tag{4.4}$$

where $v_{\mathrm{dc}}^{\max}$ represents the maximum allowable DC-link voltage.

4.4 Case Study

The PRC and the VIC methods will be validated in this section, where the simulation results in MATLAB/Simulink will be given. The configuration of

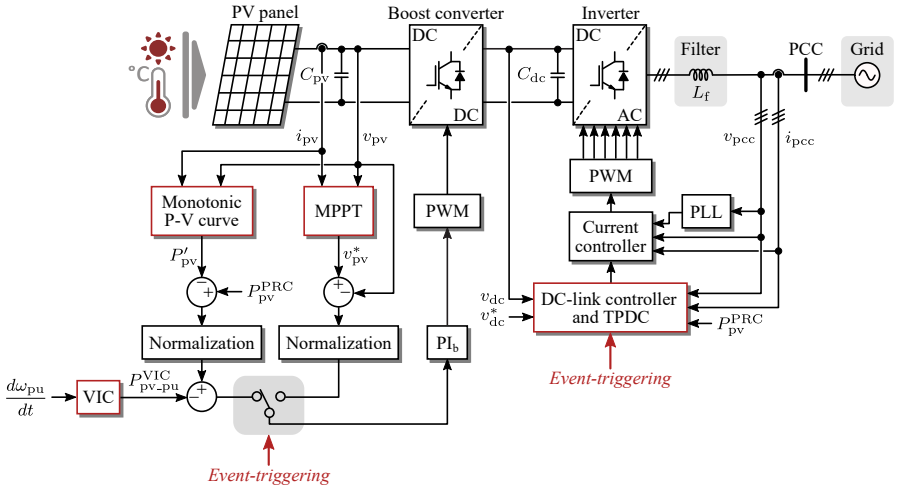

Fig. 4.8: Control system of a PV system with the MPPT-PRC and the VIC, where the definition of variables are identical with those in Chapter 2, P'_{pv} denotes the PV power generated by the pseudo monotonic P-V curve, and $P^{PRC}_{pv} = P^{max}_{pv} - P_{res}$. Source: [J4].

the case-study system is shown in Fig. 4.8. The grid is represented by a VSG. The parameters are given in Table 4.1.

4.4.1 MPPT-PRC Performance

The MPPT-PRC is validated at first. The solar irradiance and the temperature are 1000 W/m^2 and 25 °C, respectively. The simulation results of the MPPT-PRC are shown in Fig. 4.9, in which the system dynamics with and without the TPDC are presented. It shows that the MPPT-PRC can effectively achieve PV power reserve. Specifically, the MPPT algorithm accurately measures the MAP, based on which the PRP can be identified. Moreover, the event-triggering signal effectively regulates the PV system to switch between the MPPT mode and the power reserve mode. At the beginning of each PRC cycle, the event-triggering signal makes the PV system turn to the MPPT mode. Once the MAP is measured, the PV system is switched to the power reserve mode rapidly. Moreover, it can be observed in Fig. 4.9 that the TPDC can adequately damp the transient power pulses. Then, the PV system output power is smoothed.

To further validate the MPPT-PRC, the simulation under decreasing irradiance (from 1000 W/m^2 to 700 W/m^2) is carried out. The simulation results are shown in Fig. 4.10. It shows that the MPPT-PRC performs well when the irradiance changes. The MAP is accurately measured, and the transient power pulses are significantly suppressed.

Table 4.1: Parameters of the Two-Stage Three-Phase PV System. Source: [J4].

Parameter	Description	Value
	Grid	
f^*	Rated grid frequency	50 Hz
$v^{\mathrm{g}}_{\mathrm{rated}}$	Rated line-to-line grid voltage	400 V
	VSG	
P_{VSG}	Steady-state output power	2 kW
$v^{\mathrm{g}}_{\mathrm{dc}}$	Rated DC-link voltage	800 V
R	Speed regulation gain of governor	0.05 p.u.
T_{G}	Governor time constant	0.2 s
T_{T}	Turbine time constant	0.3 s
H	Inertia constant	5 s
D	Damping gain	1 p.u.
$L^{\mathrm{inv}}_{\mathrm{f}}$	Converter-side filter inductance	4.8 mH
$L^{\mathrm{g}}_{\mathrm{f}}$	Grid-side filter inductance	2 mH
$C^{\mathrm{g}}_{\mathrm{f}}$	Filter capacitance	10 μF
L_{g}	Grid inductance	2 mH
	PV System	
v^*_{dc}	DC-link voltage reference	650 V
f_{b}	Boost converter switching frequency	16 kHz
f_{inv}	Inverter switching frequency	8 kHz
f_{MPPT}	MPPT sampling frequency	100 Hz
L_{pv}	Boost converter inductance	0.5 mH
L_{f}	Inverter filter inductance	3.5 mH
C_{pv}	Boost converter capacitor	100 μF
C_{dc}	DC-link capacitor	2800 μF
$(k_{\mathrm{p\_b}}, k_{\mathrm{i\_b}})$	PI coefficients for boost converter, $\mathrm{PI_b}$	(0.2, 20)
$(k_{\mathrm{p\_dc}}, k_{\mathrm{i\_dc}})$	PI coefficients for DC-link voltage controller, $\mathrm{PI_{dc}}$	(0.2, 10)

4.4.2 VIC Performance

The VIC based on the MPPT-PRC is then validated. The VSG is adopted to represent the grid shown in Fig. 4.8, which can make the grid frequency

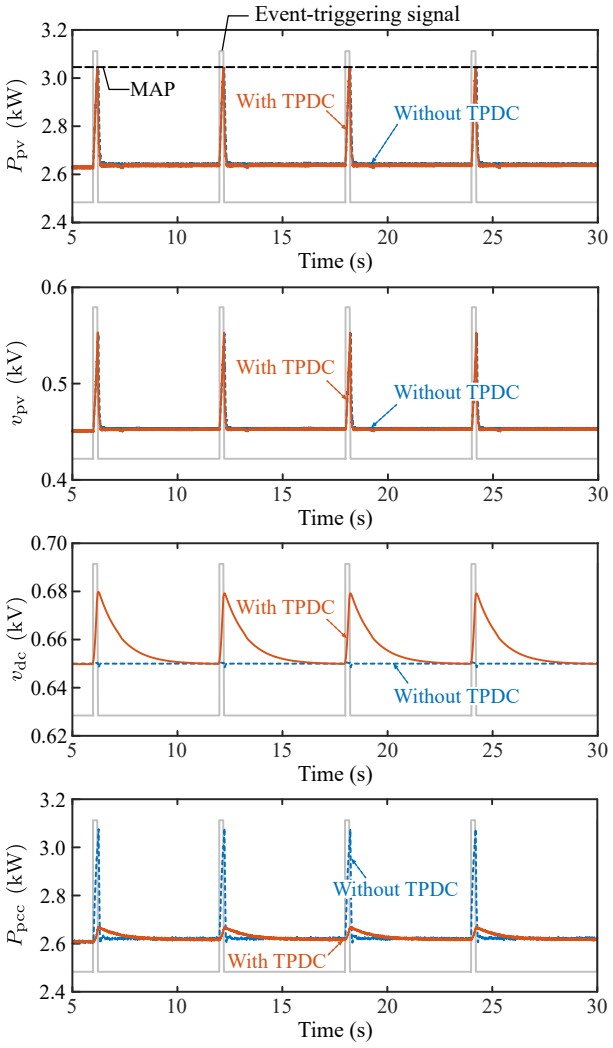

Fig. 4.9: Simulation results of the system referring to Fig. 4.8 under the MPPT-PRC with and without the TPDC, where P_{pcc} is the PV system output power at the PCC. Source: [J4].

performance more obvious. The VSG parameters are given in Table 4.1 in Appendix **??**. The control signals when the load steps by 0.45 kW and turns back to the initial are shown in Fig. 4.11. It shows that the event-triggering signal is generated reasonably. At the beginning of each PRC cycle, the event-triggering signal is enabled by the MPPT execution signal. Once the MAP is measured, the MAP detection signal disables the event-triggering signal. Additionally, the VIC enabling signal effectively deactivates the MPPT-PRC when the frequency support is enabled.

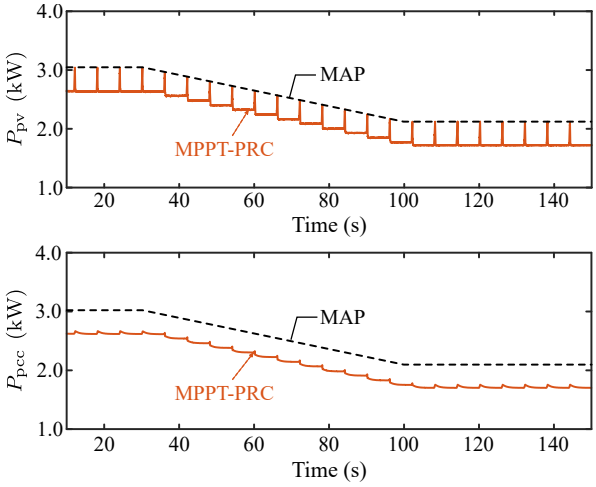

Fig. 4.10: Simulation results of the system referring to Fig. 4.8 under the MPPT-PRC when irradiance decreases. Source: [J4].

The system dynamics under the load changes are shown in Fig. 4.12. It shows that the event-triggering signal coordinates the PV system to switch between the PRC and the VIC. When the frequency is within the steady-state range, the MPPT-PRC runs normally. When the frequency deviation is detected, the VIC enabling signal turns to "1", which disables the MPPT-PRC. When the frequency returns the steady-state, the VIC enabling signal changes back to "0", and the MPPT-PRC is reactivated. Furthermore, Fig. 4.12 shows that the power reserve is released when the frequency drops due to the load step. Then, the grid frequency is effectively supported. With the VIC of the PV system, the frequency deviation, as well as the RoCoF, is reduced.

4.5 Summary

In this chapter, the VIC of PV systems based on the MPPT-PRC is proposed. First, the MPPT-PRC is demonstrated to achieve power reserve of PV systems without dependency on additional costs, including those for extra hardware and computational burden. The PRC is realized by periodically running the MPPT algorithm until the MAP is measured. Then, the PV system turns to the power reserve mode. The TPDC scheme is designed to damp the transient power generated by the MPPT execution. Additionally, to avoid oscillation between the PRPs corresponding to the same PV power reference, the pseudo monotonic P-V curve is implemented, which can make the PV system operate at the L-PRP. By properly designing the event-triggering signal, the PRC and the VIC can be coordinated effectively. When the inertia

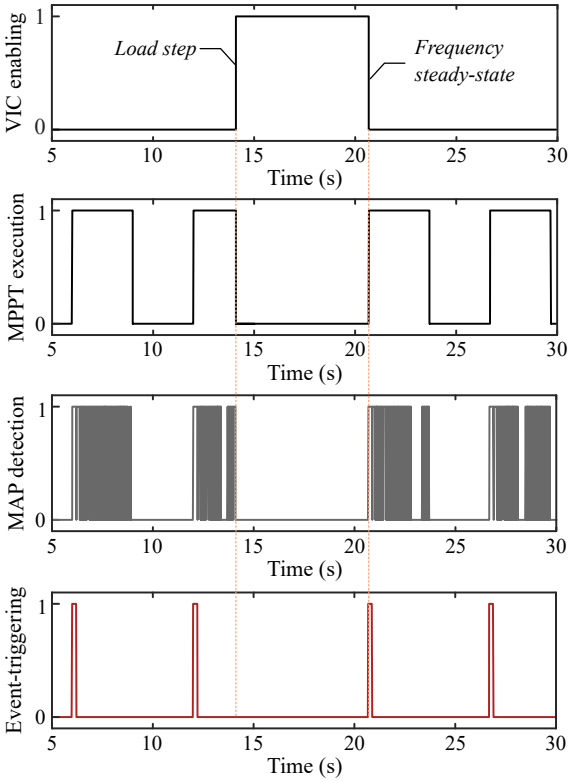

Fig. 4.11: Control signals of the MPPT-PRC and the VIC when the load changes. Source: [J4].

emulation is required, the VIC is activated, whereas the MPPT-PRC is disabled provisionally. After the frequency incident, the VIC is disabled, and the MPPT-PRC is reactivated to achieve power reserve for PV systems.

Related Publications

J3. **Q. Peng**, A. Sangwongwanich, Y. Yang, and F. Blaabjerg, "Grid-Friendly Power Control for Smart Photovoltaic Systems," *Solar Energy*, Status: In Press, DOI: 10.1016/j.solener.2020.05.001.

J4. **Q. Peng**, Z. Tang, Y. Yang, T. Liu, and F. Blaabjerg, "Event-Triggering Virtual Inertia Control of PV Systems with Power Reserve," *IEEE Trans. Ind. App.*, Status: Under Review.

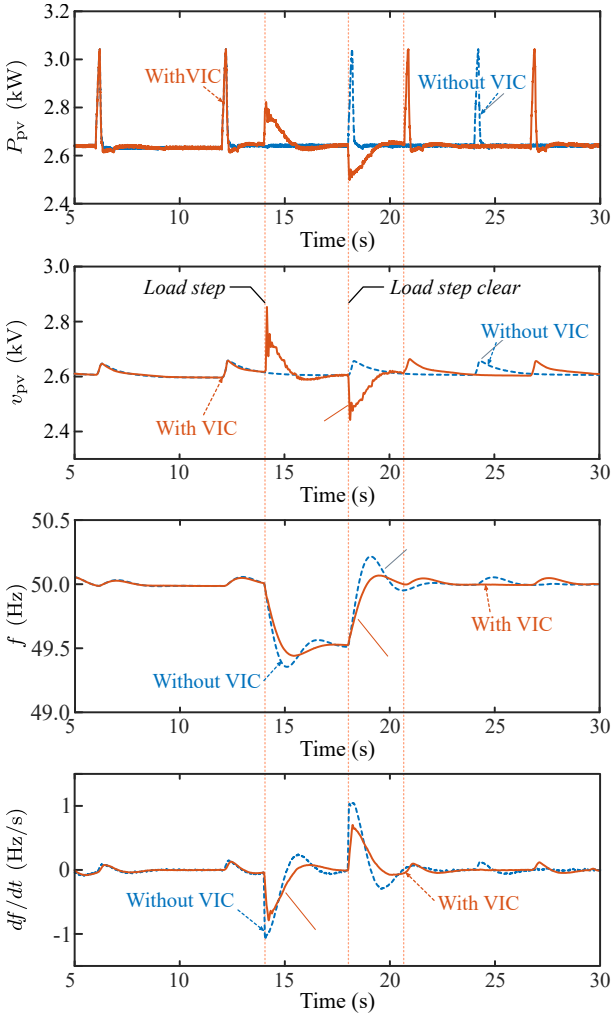

Fig. 4.12: Simulation results of the system referring to Fig. 4.8 under the MPPT-PRC-based VIC when the load changes. Here, the grid is represented by a VSG. Source: [J4].

Chapter 5

Inertia Control and Frequency Damping Coordination

This chapter will investigate the coordination of virtual inertia and frequency damping control loops of PV systems with power reserve. The impacts of inertia constant and damping gain on the frequency quality will be analyzed. Accordingly, the coordination control will be properly designed to achieve optimal frequency support.

5.1 Introduction

In Chapter 4, the MPPT-PRC of PV system is developed, based on which the VIC is realized. However, the focus of Chapter 4 is to demonstrate the coordination of the MPPT-PRC and the frequency regulation. Thus, the proposed VIC in Chapter 4 is relatively simple. It may be insufficient in some cases to adequately support the grid frequency adequately. On one hand, the frequency damping control (FDC) is also important for grid frequency stability, which is not considered in Chapter 4. On the other hand, the designed virtual inertia constant is fixed. It does not make the most of the flexible regulation capability of PV systems to some extent. A typical underfrequency incident is shown in Fig. 5.1. It shows that there are three stages, i.e., before the nadir, from the nadir to new steady-state (recovery), and from steady-state to the normal operation band (restoration). Several indices are important to reflect the frequency stability, including the nadir (determines the instantaneous frequency deviation), the recovery frequency (determines the steady-state frequency deviation), and more importantly, the RoCoF. Ac-

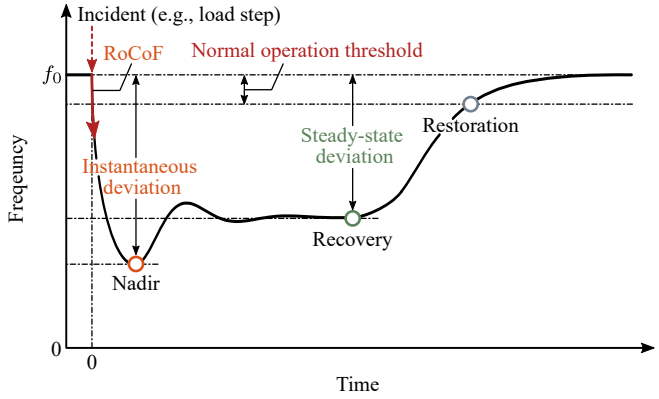

Fig. 5.1: Frequency dynamic in an under-frequency issue, where f_0 is the rated frequency. Source: [J5].

cordingly, in different stages of an incident, the requirements for frequency regulation may vary. For example, at the early stage of the incident, the RoCoF is the most important. After that, the frequency deviation is more concerned. For varying requirements, the virtual inertia constant and frequency damping gain can be adaptively regulated, by which the frequency quality can be improved, and the PV power can be used more efficiently. The main challenge is to coordinate a certain amount of the reserved power of PV systems to provide virtual inertia and frequency damping, i.e., to properly design the adaptive VIC and FDC.

The focus of the literature is usually on the realization of the PRC and the frequency regulation strategies, where the adaptive tuning of the VIC and the FDC, as well as the coordination of them, are insufficiently discussed. Consequently, the power reserve of PV systems cannot be optimally utilized, which, however, is important for next-generation smarter PV systems. To deal with this issue, the practices from the ESS-based power converters, i.e., the VSG and the VSM, etc., can be referenced, as the inertia constant and damping gain in the VSG and the VSM are usually flexibly adjusted to meet different requirements. For instance, the inertia constant can be decreased when the frequency turns back to the rated value in the oscillation, which can attenuate the transient frequency deviation [91]. Based on this, the virtual inertia and the damping gain can be adjusted collectively [92, 93]. More specifically, when the frequency is moving away from the rated value, large inertia constant can be chosen, which effectively reduce the RoCoF. When the frequency is returning to the rated value, large damping gain can be set, and then, the frequency will recover more rapidly. Other attempts are to explore the real-time tuning of virtual inertia and damping gain, based on which the energy consumption can be reduced without deteriorating the frequency sta-

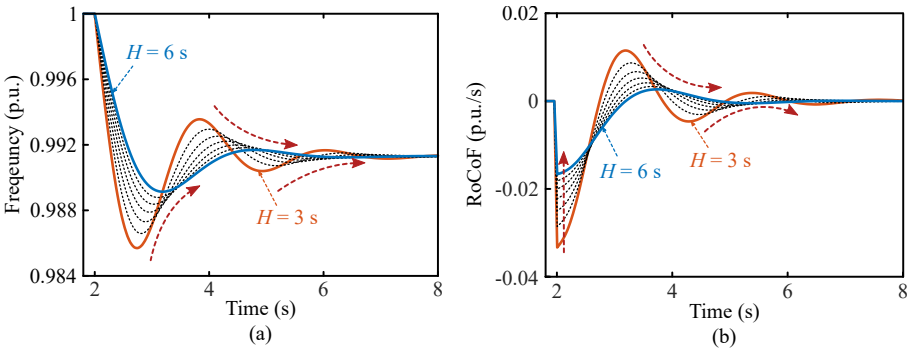

Fig. 5.2: Frequency dynamics under a load step with different inertia constants: (a) frequency and (b) RoCoF. Source: [J5].

bility [42, 94]. However, those strategies have only been implemented in grid-forming power generating units. The application in grid-feeding PV systems stills requires exploration. Additionally, the coordination of the available regulation power has not been addressed, which requires further exploration.

This chapter will address the grid frequency regulation control of PV systems, including the VIC and the FDC. The focus will be on the coordination of VIC and FDC, and the optimal utilization of PV power reserve. Notably, as the PRC has been illustrated in Chapter 4, it will not be detailed in this chapter. In addition, the frequency dynamic analysis and control strategy design will be exemplified by under-frequency incidents, which is also feasible for over-frequency incidents.

5.2 Requirements of Inertia control and Frequency Damping

As shown in (3.1), in the conventional SGs, the inertia constant and damping gain jointly decide the frequency dynamic. Accordingly, not only the VIC but also the FDC should be developed for PV systems to facilitate stronger grid support. Before that, the respective contribution of inertia constant and damping gain to the frequency stability should be clarified. Then, the VIC and the FDC can be properly designed, especially for the PV systems whose available power for frequency regulation is limited (i.e., the power reserve). Accordingly, the impacts of inertia constant and damping gain on grid frequency dynamic will be analyzed in this section, and the grid requirements for frequency quality will then be discussed.

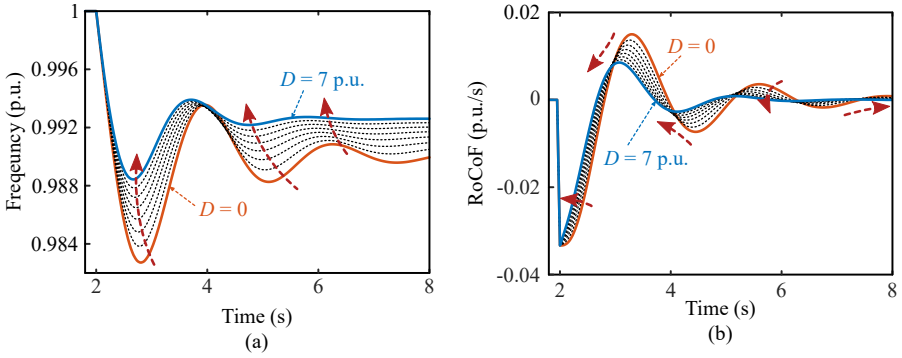

Fig. 5.3: Frequency dynamics under a load step with different damping gains: (a) frequency and (b) RoCoF. Source: [J5].

5.2.1 Impact of Inertia and Damping on Frequency Dynamic

It can be observed in (3.1) that the damping gain mainly determines the first-order droop relationship between frequency and active power. The inertia constant affects more the second-order frequency-power droop relationship. Thus, the inertia constant decides the RoCoF more, and the damping gain largely affects the frequency deviation in a frequency incident.

More specifically, the frequency dynamics under a load step with different inertia constants are shown in Fig. 5.2. It shows that when the inertia constant increases, the frequency deviation is reduced. Then, the frequency moves to the steady-state more quickly. More importantly, the RoCoF in the first oscillation period, which is the most concerned part in a frequency incident, is significantly reduced.

Similarly, the frequency dynamics under a load step with different damping gains are given in Fig. 5.3, where it can be seen that the large damping gain effectively suppresses the frequency deviation, based on which the frequency recovery time is shortened. Notably, the contribution of increasing the damping gain to the frequency deviation reduction is more conspicuous than increasing the inertia constant. However, although the overall RoCoF is reduced by increasing the damping gain, the RoCoF in the first oscillation part is barely reduced. Seen from this point of view, the grid frequency is almost not supported.

Comprehensively speaking, the inertia constant supports the grid frequency more to reduce the RoCoF, while the damping gain contributes more to decrease the steady-state frequency deviation. In turn, the RoCoF is more determined by the inertia constant, and the recovery frequency is mainly affected by the damping gain.

5.2.2 Grid Frequency Quality Requirement

The grid requirements on the frequency quality should be defined, and the requirements on the inertia constant and damping gain are clear. Then, the demands of the VIC and FDC of the PV systems can be further obtained.

The frequency quality requirements are usually defined by the system operators. For instance, the Northern Europe Grid Code [95] requires the maximum instantaneous frequency deviation and the maximum steady-state frequency deviation being $\pm$ 1 Hz and $\pm$ 0.5 Hz, respectively. Moreover, according to the Danish power grid code, the RoCoF withstanding capability of power plants is $\pm$ 2.5 Hz/s (the grid codes regarding the RoCoF specially for RESs will be developed in the future). Thus, considering the grid codes on frequency quality, the inertia constant is expected to be large at the early stage of the incident, which can effectively reduce the RoCoF. After the nadir, the RoCoF is attenuated, and the frequency deviation becomes more concerned, which should be reduced by a large damping gain.

5.3 Coordination of Inertia Control and Frequency Damping

According to the grid requirements on the frequency supports, the VIC and the FDC coordination strategy can be designed, which will be illustrated in this section.

First, the basic VIC and FDC are introduced. In analogy to (3.1), the VIC and the FDC are controlling the PV power in response to the frequency as

$$\begin{cases} P_{\mathrm{pv}}^{\mathrm{VIC}} = 2H_{\mathrm{pv}}\dfrac{d\omega}{dt} \\ P_{\mathrm{pv}}^{\mathrm{FDC}} = D_{\mathrm{pv}}(\omega - \omega^*) \end{cases}, \tag{5.1}$$

where H_{pv} and D_{pv} are the inertia constant and the damping gain emulated by the PV systems, respectively, and $P_{\mathrm{pv}}^{\mathrm{VIC}}$ and $P_{\mathrm{pv}}^{\mathrm{FDC}}$ are the PV power used for the VIC and FDC realization.

When the power reserve of PV system is applied only to provide virtual inertia, the maximum virtual inertia can be obtained as

$$H_{\mathrm{pv}}^{\max} = \frac{P_{\mathrm{res}}^{\mathrm{VIC}}}{2\dfrac{d\omega_{\mathrm{t}}}{dt}}, \tag{5.2}$$

with $\dfrac{d\omega_{\mathrm{t}}}{dt}$ being the RoCoF threshold from the grid code and $P_{\mathrm{res}}^{\mathrm{VIC}}$ being part of the power reserve for the VIC.

Table 5.1: Strategy of the Proposed Control Method. Source: [J5].

Stage	Inertia constant	Damping gain	Power reserve Utilization
Before the nadir	$H_{\mathrm{pv}}^{\max}$	0	$P_{\mathrm{pv}}^{\mathrm{VIC}} = P_{\mathrm{res}}$
After the nadir	$H_{\mathrm{pv}}^{\max} \Rightarrow 0$	$0 \Rightarrow D_{\mathrm{pv}}^{\max}$	$P_{\mathrm{pv}}^{\mathrm{FDC}} = P_{\mathrm{res}}$

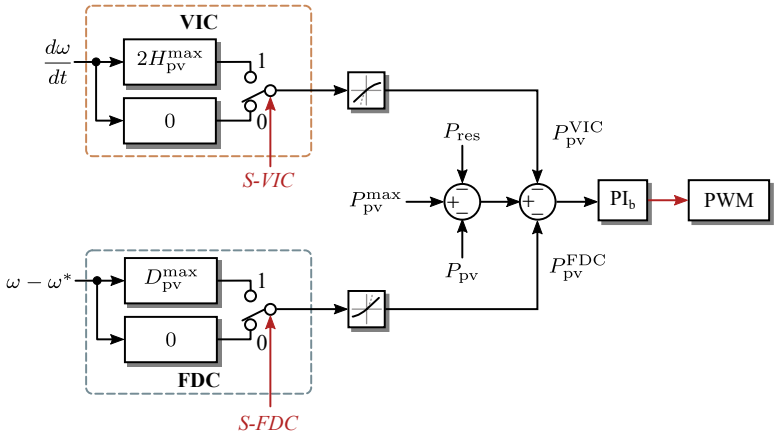

Fig. 5.4: Control scheme of the proposed VIC and FDC coordination strategy in the boost converter, where S-VIC and S-FDC are the signals for the control mode switching of the VIC and the FDC, respectively. Source: [J5].

Similarly, when the power reserve is adopted solely to provide frequency damping, the maximum damping gain can be achieved as

$$D_{\mathrm{pv}}^{\max} = \frac{P_{\mathrm{res}}^{\mathrm{FDC}}}{\omega_{\mathrm{t}} - \omega^*}, \tag{5.3}$$

in which ω_{t} is the frequency limit set by the grid code and $P_{\mathrm{res}}^{\mathrm{FDC}}$ is part of the power reserve for the FDC.

The VIC and FDC coordination strategy is aiming to support the frequency by optimally utilizing the power reserve of PV systems, i.e., to reduce the RoCoF and the frequency deviation. More specifically, the power reserve is fully used to emulate inertia before the nadir to decrease the RoCoF, where it is employed to generate frequency damping after the nadir to damp the frequency deviation. The control strategy is illustrated in Table 5.1. The control system is similar to the one as shown in Fig. 4.8. Notably, the control scheme in the boost converter is modified as shown in Fig. 5.4, where the control signals (S-VIC and S-FDC) are important for control mode switching. The generation of the control signals is shown in Fig. 5.5. Specifically, when

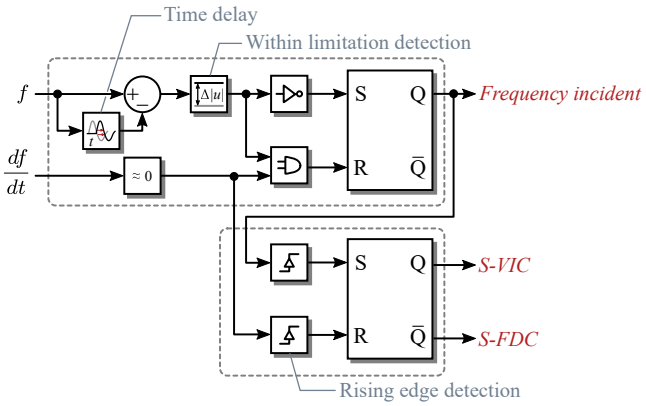

Fig. 5.5: Generation of the control signals (S-VIC and S-FDC) in Fig. 5.4. Source: [J5].

the frequency moves beyond the limit, the frequency incident signal will turn to "1" from "0", which will return "0" when the frequency moves back to the steady-state. Each rising edge of the frequency incident signal makes S-VIC turn to "1" from "0". Then, once the RoCoF equals 0, i.e., the nadir is reached, S-VIC returns "0". S-FDC is the inverse of S-VIC.

5.4 Case Study

The proposed VIC and FDC coordination strategy is validated in this section. The configuration of the case-study system is identical with the one shown in Fig. 4.8, whereas the boost converter control is shown in Fig. 5.4. The system parameters are also given in Table 4.1. For comparison, four different frequency regulation strategies of PV systems are performed on the same case-study system. The comparative control strategies are described as follows [J5].

- *Strategy I*: Single VIC strategy. In this strategy, the virtual inertia constant is fixed as $H_{\text{pv}}^{\text{max}}$, whereas the damping gain is zero.
- *Strategy II*: Single FDC strategy. In this strategy, the damping gain is fixed as $D_{\text{pv}}^{\text{max}}$, whereas the virtual inertia constant is zero.
- *Strategy III*: Fixed VIC&FDC strategy. In this strategy, the power reserve of the PV systems is evenly divided to simultaneously realize the VIC and FDC. The virtual inertia constant and the damping gain are set to be constant.
- *Strategy IV*: Alternating inertia strategy. This is proposed in [91], where the virtual inertia is switched to be small (0 in this chapter) when the

frequency is moving back to the steady-state. As demonstrated in [91], the frequency recovery speed will be faster while the energy consumption can be reduced.

First, the proposed coordination strategy is compared with two basic frequency regulation strategies, i.e., Strategy I and Strategy II. The system dynamics under a load step are shown in Fig. 5.6. It shows that with Strategy I, the RoCoF under the load step is effectively reduced, and the frequency goes back to steady-state more quickly. However, as there is no damping support, the steady-state frequency deviation has not been decreased. With Strategy II, the steady-state frequency deviation is reduced, but the RoCoF is not damped. With the proposed control strategy, the RoCoF as well as the steady-state frequency deviation can be effectively reduced. More importantly, compared with Strategy II, the steady-state frequency deviation under the proposed strategy is smaller. This is due to that the damping gain in Strategy II is limited by the maximum instantaneous frequency deviation in the grid code, whereas the damping gain in the proposed strategy is limited by the maximum steady-state frequency deviation [J5]. Therefore, the proposed control performs much better than Strategy I and Strategy II.

Then, the proposed control strategy is compared with advanced grid frequency regulation strategies, i.e., Strategy III and Strategy IV. The system dynamics under a load step and the changes of inertia constants and damping gains are shown in Figs. 5.7 to 5.8. It is observed in Fig. 5.7 that Strategy III and the proposed strategy can reduce the RoCoF and the steady-state frequency deviation. However, as only half of the power reserve is utilized to generate frequency damping in Strategy III, it contributes less to decrease the steady-state frequency deviation than the proposed strategy. Moreover, the virtual inertia provided by Strategy III is also smaller than the proposed strategy due to the insufficient utilization of the power reserve. As for Strategy IV, it successfully provides virtual inertia to the grid and reduces the RoCoF. Notably, as pointed out in [91], the advantage of Strategy IV is that the frequency recovery speed can be promoted. However, it has not been observed in Fig. 5.7. The reason may be that a strong grid is adopted in [91], in which the frequency will return to the nominal state after oscillations caused by an incident. The PV system in this chapter is integrated to a weak grid (represented by a VSG). In such a case, the frequency will move to a new steady-state after a load step. Then, instead of accelerating the frequency recovery, the control strategy proposed in [91] takes more time to make the frequency reach the new steady-state. Considering the above, the proposed strategy can effectively reduce the RoCoF and steady-state frequency deviation, while the power reserve can be optimally utilized.

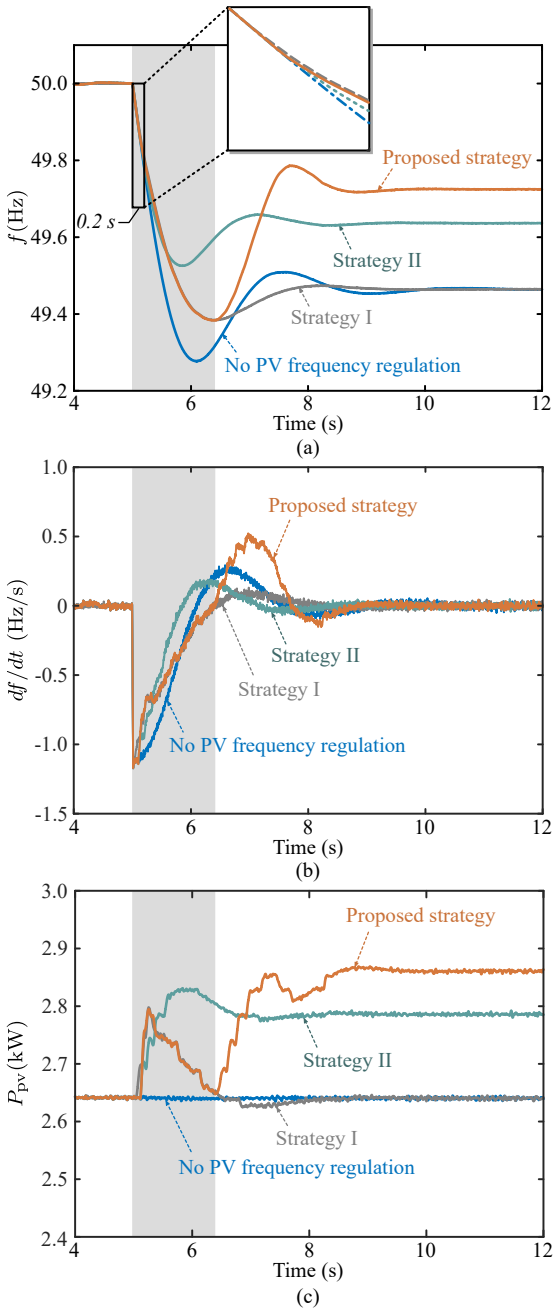

Fig. 5.6: Simulation results of the proposed control strategy, Strategy I, and Strategy II under a load step: (a) grid frequency, (b) RoCoF, and (c) PV power. Source: [J5].

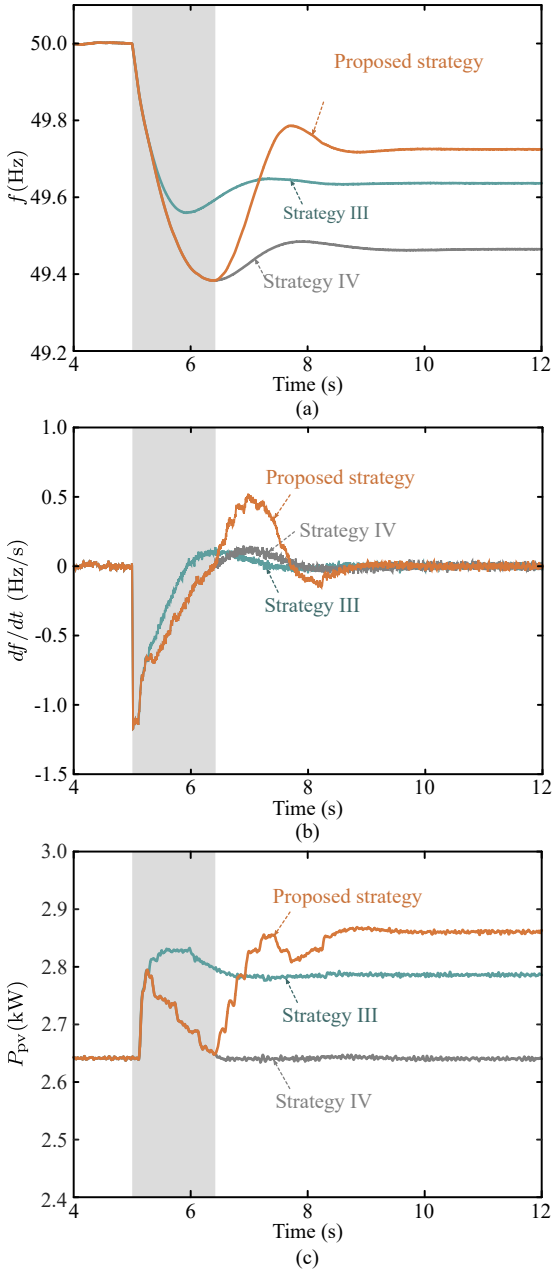

Fig. 5.7: Simulation results of the proposed control strategy, Strategy III, and Strategy IV under a load step: (a) grid frequency, (b) RoCoF, and (c) PV power. Source: [J5].

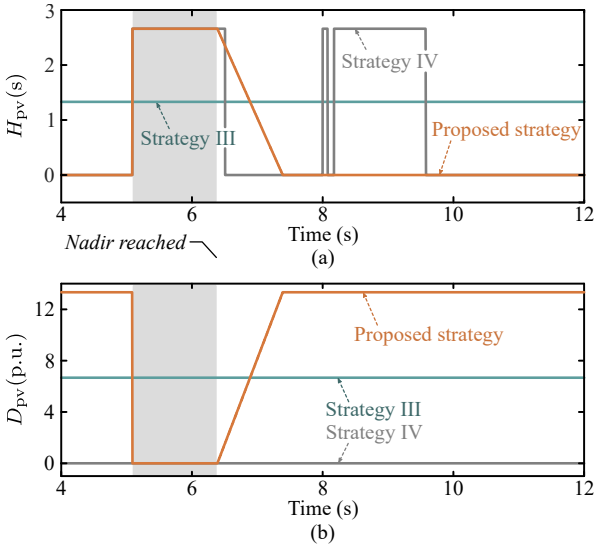

Fig. 5.8: Changes of inertia constants and damping gains corresponding to the case study in Fig. 5.7. Source: [J5].

5.5 Summary

A VIC and FDC coordination strategy of PV systems with power reserve is proposed in this chapter. First, the impacts of inertia constant and damping gain on frequency dynamics are discussed. Accordingly, the requirements of VIC and FDC are clarified with respect to the grid code on frequency quality. Then, the VIC and the FDC of PV systems are coordinated to achieve optimal frequency support, where the power reserve is utilized to facilitate VIC before the nadir of a frequency incident, devoting to reduce the RoCoF. Once the nadir is reached, the power reserve is used to realize the FDC, which contributes to decrease the steady-state frequency deviation. Based on the proposed strategy, the power reserve of PV systems can be optimally utilized to support the grid frequency more adequately.

Related Publications

J5. **Q. Peng**, Y. Yang, T. Liu, and F. Blaabjerg, "Coordination of Virtual Inertia Control and Frequency Damping in PV Systems for Optimal Frequency Support," *CPSS Trans. Power Electron. App.*, Status: Under Review.

Chapter 6

Summary and Outlook

This chapter will summarize the research during the Ph.D. study - *Stability and Control of Grid-Friendly PV Systems*. The results, outcomes, and contributions, will be highlighted. The outlook and perspective will be demonstrated at the end of this chapter.

6.1 Conclusion

In this Ph.D. project, the main objective is to develop a stronger power system supported by grid-friendly PV systems. Several stability and control challenges of power electronics-based systems have been discussed. Aiming to address those challenges, the potential solutions to enhancing the system stability are reported, including the approaches from the power converters and the PV systems. This Ph.D. project is summarized as follows.

First, the background of the entire Ph.D. project was addressed in *Chapter 1*, where the stability and control challenges of modern power grids were summarized, based on which the motivation of this Ph.D. project was demonstrated. In the modern power grid, one of the dominant challenges is the frequency instability due to the lack of inertia, which is conventionally provided by the SGs. With the SGs being replaced by power electronics and RESs, the mechanical inertia is continuously decreasing, and the stability of the modern power grid is being threatened. Consequently, the power grid analysis in terms of the inertia characteristic and frequency stability becomes important. Moreover, the frequency regulation strategies from power electronics and RESs are also demanded.

Aiming at the inertia characteristic analysis, a universal modeling method of power converters was proposed in *Chapter 2*. According to the swing equation of SG rotors, the inertia characteristic can be reflected by the relationship between the active power and the internal voltage phase angle. Inspired by

this, the PIV model of power converters was developed to reveal the power and internal voltage relationship of power converters. The model takes various control loops into account. According to the multi-timescale analysis concept, the current controllers and other control loops at faster timescale were ignored for simplicity. At the end of *Chapter 2*, the model was validated by simulations, and it was proven to be effective for the converter stability analysis.

Although the inertia characteristics of power converters can be addressed by the PIV model, the effective inertia that can enhance the grid frequency stability should be provided by specially designed VIC strategies. As discussed in *Chapter 1*, the virtual inertia provision from DC-link capacitors can be a universal solution for inertia enhancement of the modern power grid. However, the proper design of the VIC of DC-link capacitors with addressing the system stability still requires further exploration. Considering this issue, the PIV models at different timescales were aggregated into a multi-timescale model in *Chapter 3*. Then, the maximum virtual inertia of DC-link capacitors was identified while maintaining system stability. The multi-timescale PIV model contains several submodels at different timescales, which can be adopted for different applications. First, the system stability was analyzed based on the submodel at the VCT, and the VIC of DC-link capacitors was properly tuned. Then, the effective virtual inertia was identified based on the submodel at the RMT. The multi-timescale model and the maximum inertia of the DC-link capacitor were validated by simulations and experiments.

Further concerns should be addressed that the virtual inertia from DC-link capacitors is limited by its capacitance. It is not sufficient in some cases. Thus, the inertia emulation solution from stronger power sources is demanded. As introduced in *Chapter 1*, the PV systems are being more and more important in the modern power grid than ever before. Additionally, the PV power is flexible for regulation, which makes the PV systems viable for inertia emulation. To achieve so, the power reserve was demanded for the PV systems. Accordingly, the flexible power control of PV systems was discussed in *Chapter 4*. A novel PRC was introduced at first, which was independent of extra sensors and complicated computations. The PRC and VIC coordination strategy was then realized based on the PRC. The design of the event-triggering signal that coordinates the control loops was introduced in detail. The proposed PRC and VIC were validated to be effective to enhance the system inertia by simulations.

Apart from the virtual inertia, the frequency damping is also demanded by the grid. For the next-generation smart PV systems, the frequency damping provision is as important as the inertia emulation. However, for the PV systems with limited power reserve, the inertia emulation and frequency damping provision should be properly coordinated. Accordingly, the VIC and FDC coordinated strategy was addressed in *Chapter 5*. The impacts of

inertia constant and damping gain on the frequency dynamics were investigated. Meanwhile, the frequency regulation demands were analyzed according to the grid codes on frequency quality. In light of the above, the demands for the VIC, the FDC and the coordination of them were clarified. The allocation of the power reserve for VIC and FDC realization were depicted for optimal frequency support performance. The simulation verifies the control strategy.

6.2 Main Contributions

The main contributions of this Ph.D. project are summarized as follows:

Universal modeling method of power converters

A universal modeling reflecting the power and internal voltage relationship of power converters has been proposed in this Ph.D. project. The model can not only facilitate the stability analysis of the grid-connected power converters, but also reveal their virtual inertia characteristics. The uniform external interfaces of the model make the analysis of multiple converters more intuitional. Then, the PIV model can become a general tool for the power electronic-based systems to conduct the inertia evaluation as well as the stability analysis.

Maximum virtual inertia provision from DC-link capacitors

The maximum virtual inertia identification method of DC-link capacitors has been investigated in this project. The PIV models at different timescales are aggregated into a multi-timescale PIV model, based on which two main objectives can be achieved as follows:

- System stability analysis at the concerned timescale
- Maximum effective inertia identification at the RMT

The maximum virtual inertia analysis is beneficial to the system-level inertia placement and optimization. It is also important for the stability of the future power system.

Power reserve control of PV systems for frequency support

A cost-effective and computation-efficient PRC method and its coordination with the VIC are realized. The PRC is independent of environment sensors and cumbersome computations. Additionally, in the proposed method, the MAP is measured in real-time, which minimize the estimation error. With

the properly designed control signals, the PRC and VIC of PV systems can be effectively coordinated. The outcome is of importance for flexible frequency regulation of PV systems.

Comprehensive frequency regulation strategy of PV systems

The coordination strategy of the VIC and FDC of PV systems has been developed in this Ph.D. project, yielding comprehensive frequency support to the grid. The control strategy takes the effects of inertia and frequency damping to the frequency dynamic and the grid requirements on frequency quality into account. In this way, the frequency regulation strategy can optimally employ the power reserve of PV systems, and the grid frequency can be effectively supported by the PV systems.

6.3 Research Outlook

Several issues and solutions regarding the stability and control of power electronic-based systems considering a high-penetration level of PV systems have been investigated in this Ph.D. project. However, there are still challenges to be tackled for a more stable power system with various RESs.

- The universal modeling method can be validated by power converters with different control strategies. For example, the model predictive control, the fuzzy control, or the self-synchronization control can be considered. In this way, the general modeling methodology can be clarified, based on which the modeling of more complicated systems may become possible. Moreover, the interaction among power converters can be addressed, and the system stability enhancement strategy can be designed accordingly.
- The VIC of the DC-link capacitors can be also applied in power converters with different basic control strategies, as it is essentially an additional control loop with respect to the basic control system. In this way, the inertia emulated DC-link capacitors can be verified to be a universal solution for inertia enhancement of the power electronics-based systems.
- The multi-timescale PIV model and the maximum inertia identification method can be further applied for other virtual inertia sources, e.g., the PV systems and the wind farms with the VIC. In this way, the inertia provision capability of each power unit can be identified, and the system-level inertia placement and optimization can be achieved.

- When addressing the effects of virtual inertia provision on the system in this project, the small signal stability is focused. However, the system dynamic under large disturbances is also important. Thus, the transient model and stability analysis method may be required for more reasonable maximum inertia identification, which comprehensively considers the system stability in different situations.
- The PRC and the frequency regulation control of PV systems can be further developed to deal with more complicated issues. For example, cascaded frequency incidents or PV power drop due to sudden environmental changes with extreme weather conditions can be addressed.
- The grid frequency support strategies of PV systems proposed in this Ph.D. are independent of ESSs. However, with the development of energy storage technology, the cost of ESS will largely reduce. How to coordinate the PV power regulation and the ESSs to support the grid better is an interesting topic.
- The inertia emulation in grid-feeding converters is addressed in this Ph.D. project. Apart from this, the virtual inertia provided by grid-forming converters also accounts for a great proportion. Thus, the analysis and control of grid-forming converters, e.g., the VSG, the VSM, or the frequency-power droop-controlled converters, can be addressed.
- The RESs are continuously penetrating the modern power grid. In the future, the power electronics may account for most of the power transmission in the grid. In such a case, if the virtual inertia is still required should be considered. How to coordinate all the power generating units and achieve global stability in the future power grid demands further exploration.

Apart from the above-mentioned, an important issue should be noted that the power electronics technology is rapidly developing. For instance, various control strategies and topologies of power converters are emerging day by day. In this context, the modeling method, analysis method, and the additional frequency support strategies proposed in this Ph.D. project may need modifications to fulfill the demands of the future power grid consisting of smarter PV systems.

Bibliography

References

[1] M. Child, O. Koskinen, L. Linnanen, and C. Breyer, "Sustainability Guardrails for Energy Scenarios of the Global Energy Transition," *Renewable and Sustainable Energy Reviews*, vol. 91, pp. 321–334, Aug. 2018.

[2] IRENA, "Global Eergy Transformation: A Roadmap to 2050 (2019 Edition)," Abu Dhabi, UAE, Tech. Rep. ISBN: 978-92-9260-121-8, Apr. 2019.

[3] F. Blaabjerg and K. Ma, "Wind Energy Systems," *Proc. IEEE*, vol. 105, no. 11, pp. 2116–2131, Nov. 2017.

[4] F. Blaabjerg, Y. Yang, D. Yang, and X. Wang, "Distributed Power-Generation Systems and Protection," *Proc. IEEE*, vol. 105, no. 7, pp. 1311–1331, Jul. 2017.

[5] Y. Khayat, Q. Shafiee, R. Heydari, M. Naderi, T. Dragičević, J. W. Simpson-Porco, F. Dörfler, M. Fathi, F. Blaabjerg, J. M. Guerrero, and H. Bevrani, "On the Secondary Control Architectures of AC Microgrids: An Overview," *IEEE Trans. Power Electron.*, vol. 35, no. 6, pp. 6482–6500, Jun. 2020.

[6] P. Kundur, N. J. Balu, and M. G. Lauby, *Power System Stability and Control*. New York, NY, USA: McGraw-hill, 1994.

[7] P. Tielens and D. Van Hertem, "The Relevance of Inertia in Power Systems," *Renew. Sustain. Energy Rev.*, vol. 55, pp. 999–1009, Mar. 2016.

[8] H. Golpîra, H. Seifi, A. R. Messina, and M. Haghifam, "Maximum Penetration Level of Micro-Grids in Large-Scale Power Systems: Frequency Stability Viewpoint," *IEEE Trans. Power Syst.*, vol. 31, no. 6, pp. 5163–5171, Nov. 2016.

[9] J. Fang, H. Li, Y. Tang, and F. Blaabjerg, "On the Inertia of Future More-Electronics Power Systems," *IEEE J. Emerg. Sel. Top. Power Electron.*, vol. 7, no. 4, pp. 2130–2146, Dec. 2019.

[10] AEMO, "Black System South Australia 28 September 2016 - Final Report," Tech. Rep., Mar. 2017.

[11] National Grid ESO, "Technical Report on the Events of 9 August 2019," Wokingham, UK, Tech. Rep., Sep. 2019.

[12] C. Breyer, D. Bogdanov, A. Gulagi, A. Aghahosseini, L. S. Barbosa, O. Koskinen, M. Barasa, U. Caldera, S. Afanasyeva, M. Child, J. Farfan, and P. Vainikka, "On the Role of Solar Photovoltaics in Global Energy Transition Scenarios," *Prog. Photovolt: Res. Appl.*, vol. 25, no. 8, pp. 727–745, Aug. 2017.

[13] SolarPower Europe, "Global Market Outlook for Solar Power 2020-2024," Brussels, Belgium, Tech. Rep., Jun. 2020.

[14] E. Tröster and E. GmbH, "New German Grid Codes for Connecting PV Systems to the Medium Voltage Power Grid," in *Proc. 2nd Int. Workshop Concentrating Photovoltaic Power Plants: Optical Design, Production, Grid Connection*, Darmstadt, Germany, Mar. 2009, pp. 1–4.

[15] IEEE Std 1547-2018 Revis. IEEE Std 1547-2003, *IEEE Standard for Interconnection and Interoperability of Distributed Energy Resources with Associated Electric Power Systems Interfaces*. New York, NY, USA: IEEE, Apr. 2018.

[16] Hydro-Quebéc, "Technical Requirements for the Connection of Generating Stations to the Hydro-Québec Transmission System," Montréal, QC, Canada, Tech. Rep. Decision D-2018-145, Jan. 2019.

[17] Y. Yang, F. Blaabjerg, H. Wang, and M. G. Simões, "Power Control Flexibilities for Grid-Connected Multi-Functional Photovoltaic Inverters," *IET Renew. Power Gener.*, vol. 10, no. 4, pp. 504–513, 2016.

[18] J. Sun, "Impedance-Based Stability Criterion for Grid-Connected Inverters," *IEEE Trans. Power Electron.*, vol. 26, no. 11, pp. 3075–3078, Nov. 2011.

[19] W. Cao, Y. Ma, and F. Wang, "Sequence-Impedance-Based Harmonic Stability Analysis and Controller Parameter Design of Three-Phase Inverter-Based Multibus AC Power Systems," *IEEE Trans. Power Electron.*, vol. 32, no. 10, pp. 7674–7693, Oct. 2017.

[20] X. Wang, F. Blaabjerg, and W. Wu, "Modeling and Analysis of Harmonic Stability in an AC Power-Electronics-Based Power System," *IEEE Trans. Power Electron.*, vol. 29, no. 12, pp. 6421–6432, Dec. 2014.

[21] X. Wang and F. Blaabjerg, "Harmonic Stability in Power Electronic-Based Power Systems: Concept, Modeling, and Analysis," *IEEE Trans. Smart Grid*, vol. 10, no. 3, pp. 2858–2870, May 2019.

[22] Katsuhiko Ogata, *Modern Control Engineering - 3rd Edition*. Upper Saddle River, NJ, USA: Prentice-Hall, 1997.

[23] R. D. Middlebrook and S. Cuk, "A General Unified Approach to Modelling Switching-Converter Power Stages," in *Proc. IEEE Power Electron. Spec. Conf.*, Cleveland, OH, USA, Jun. 1976, pp. 18–34.

[24] J. Z. Zhou, H. Ding, S. Fan, Y. Zhang, and A. M. Gole, "Impact of Short-Circuit Ratio and Phase-Locked-Loop Parameters on the Small-Signal Behavior of a VSC-HVDC Converter," *IEEE Trans. Power Deliv.*, vol. 29, no. 5, pp. 2287–2296, Oct. 2014.

[25] E. Prieto-Araujo, F. D. Bianchi, A. Junyent-Ferre, and O. Gomis-Bellmunt, "Methodology for Droop Control Dynamic Analysis of Multiterminal VSC-HVDC Grids for Offshore Wind Farms," *IEEE Trans. Power Deliv.*, vol. 26, no. 4, pp. 2476–2485, Oct. 2011.

[26] N. Pogaku, M. Prodanović, and T. C. Green, "Modeling, Analysis and Testing of Autonomous Operation of An Inverter-Based Microgrid," *IEEE Trans. Power Electron.*, vol. 22, no. 2, pp. 613–625, Mar. 2007.

[27] A. Rodríguez-Cabero, M. Prodanovic, and J. Roldán-Pérez, "Analysis of Dynamic Properties of VSCs Connected to Weak Grids Including the Effects of Dead Time and Time Delays," *IEEE Trans. Sustain. Energy*, vol. 10, no. 3, pp. 1066–1075, Jul. 2019.

[28] A. Rodríguez-Cabero, J. Roldán-Pérez, and M. Prodanovic, "Virtual Impedance Design Considerations for Virtual Synchronous Machines in Weak Grids," *IEEE J. Emerg. Sel. Top. Power Electron.*, vol. 8, no. 2, pp. 1477–1489, Jun. 2020.

[29] W. Du, Q. Fu, and H. Wang, "Small-Signal Stability of an AC/MTDC Power System as Affected by Open-Loop Modal Coupling Between the VSCs," *IEEE Trans. Power Syst.*, vol. 33, no. 3, pp. 3143–3152, May 2018.

[30] M. Jin and M. Weiming, "Power Converter EMI Analysis Including IGBT Nonlinear Switching Transient Model," *IEEE Trans. Ind. Electron.*, vol. 53, no. 5, pp. 1577–1583, Oct. 2006.

[31] K. Rouzbehi, A. Miranian, A. Luna, and P. Rodriguez, "DC Voltage Control and Power Sharing in Multiterminal DC Grids Based on Optimal DC Power Flow and Voltage-Droop Strategy," *IEEE J. Emerg. Sel. Top. Power Electron.*, vol. 2, no. 4, pp. 1171–1180, Dec. 2014.

[32] M. Zhao, X. Yuan, J. Hu, and Y. Yan, "Voltage Dynamics of Current Control Time-Scale in a VSC-Connected Weak Grid," *IEEE Trans. Power Syst.*, vol. 31, no. 4, pp. 2925–2937, Jul. 2016.

[33] W. Tang, J. Hu, Y. Chang, and F. Liu, "Modeling of DFIG-Based Wind Turbine for Power System Transient Response Analysis in Rotor Speed Control Timescale," *IEEE Trans. Power Syst.*, vol. 33, no. 6, pp. 6795–6805, Nov. 2018.

[34] H. Yuan, X. Yuan, and J. Hu, "Modeling of Grid-Connected VSCs for Power System Small-Signal Stability Analysis in DC-Link Voltage Control Timescale," *IEEE Trans. Power Syst.*, vol. 32, no. 5, pp. 3981–3991, Sep. 2017.

[35] Y. Huang, X. Zhai, J. Hu, D. Liu, and C. Lin, "Modeling and Stability Analysis of VSC Internal Voltage in DC-Link Voltage Control Timescale," *IEEE J. Emerg. Sel. Top. Power Electron.*, vol. 6, no. 1, pp. 16–28, Mar. 2018.

[36] Y. Huang, X. Yuan, J. Hu, and P. Zhou, "Modeling of VSC Connected to Weak Grid for Stability Analysis of DC-Link Voltage Control," *IEEE J. Emerg. Sel. Top. Power Electron.*, vol. 3, no. 4, pp. 1193–1204, Dec. 2015.

[37] Y. Huang, X. Yuan, J. Hu, P. Zhou, and D. Wang, "DC-Bus Voltage Control Stability Affected by AC-Bus Voltage Control in VSCs Connected to Weak AC Grids," *IEEE J. Emerg. Sel. Top. Power Electron.*, vol. 4, no. 2, pp. 445–458, Jun. 2016.

[38] J. Hu, H. Yuan, and X. Yuan, "Modeling of DFIG-Based WTs for Small-Signal Stability Analysis in DVC Timescale in Power Electronized Power Systems," *IEEE Trans. Energy Convers.*, vol. 32, no. 3, pp. 1151–1165, Sep. 2017.

[39] J. Hu, J. Zhu, and M. Wan, "Modeling and Analysis of Modular Multilevel Converter in DC Voltage Control Timescale," *IEEE Trans. Ind. Electron.*, vol. 66, no. 8, pp. 6449–6459, Aug. 2019.

[40] J. Driesen and K. Visscher, "Virtual Synchronous Generators," in *Proc. IEEE Power Energy Soc. (PES) Gen. Meeting*, Pittsburgh, PA, USA, Jul. 2008, pp. 1–3.

[41] H. Beck and R. Hesse, "Virtual Synchronous Machine," in *Proc. 9th Ind. Conf. EPQU*, Barcelona, Spain, Oct. 2007, pp. 1–6.

[42] U. Markovic, Z. Chu, P. Aristidou, and G. Hug, "LQR-Based Adaptive Virtual Synchronous Machine for Power Systems With High Inverter Penetration," *IEEE Trans. Sustain. Energy*, vol. 10, no. 3, pp. 1501–1512, Jul. 2019.

[43] Q.-C. Zhong and G. Weiss, "Synchronverters: Inverters That Mimic Synchronous Generators," *IEEE Trans. Ind. Electron.*, vol. 58, no. 4, pp. 1259–1267, Apr. 2011.

[44] O. Stanojev, U. Markovic, P. Aristidou, G. Hug, D. S. Callaway, and E. Vrettos, "MPC-Based Fast Frequency Control of Voltage Source Converters in Low-Inertia Power Systems," *IEEE Trans. Power Syst.*, 2020, early access, doi: 10.1109/TPWRS.2020.2999652.

[45] A. Tayyebi, D. Groß, A. Anta, F. Kupzog, and F. Dörfler, "Frequency Stability of Synchronous Machines and Grid-Forming Power Converters," *IEEE J. Emerg. Sel. Top. Power Electron.*, vol. 8, no. 2, pp. 1004–1018, Jun. 2020.

[46] J. Zhu, C. D. Booth, G. P. Adam, A. J. Roscoe, and C. G. Bright, "Inertia Emulation Control Strategy for VSC-HVDC Transmission Systems," *IEEE Trans. Power Syst.*, vol. 28, no. 2, pp. 1277–1287, May 2013.

[47] J. Fang, H. Li, Y. Tang, and F. Blaabjerg, "Distributed Power System Virtual Inertia Implemented by Grid-Connected Power Converters," *IEEE Trans. Power Electron.*, vol. 33, no. 10, pp. 8488–8499, Oct. 2018.

[48] J. Fang, P. Lin, H. Li, Y. Yang, and Y. Tang, "An Improved Virtual Inertia Control for Three-Phase Voltage Source Converters Connected to a Weak Grid," *IEEE Trans. Power Electron.*, vol. 34, no. 9, pp. 8660–8670, Sep. 2019.

[49] X. Huang, K. Wang, G. Li, and H. Zhang, "Virtual Inertia-Based Control Strategy of Two-Stage Photovoltaic Inverters for Frequency Support in Islanded Micro-Grid," *Electronics*, vol. 7, no. 11, p. 340, Nov. 2018.

[50] Y. Yang, K. A. Kim, F. Blaabjerg, and A. Sangwongwanich, *Advances in Grid-Connected Photovoltaic Power Conversion Systems*. Woodhead Publishing, 2018.

[51] E. Koutroulis, K. Kalaitzakis, and N. Voulgaris, "Development of A Microcontroller-Based, Photovoltaic Maximum Power Point Tracking Control System," *IEEE Trans. Power Electron.*, vol. 16, no. 1, pp. 46–54, Jan. 2001.

[52] T. Esram and P. L. Chapman, "Comparison of Photovoltaic Array Maximum Power Point Tracking Techniques," *IEEE Trans. Energy Convers.*, vol. 22, no. 2, pp. 439–449, Jun. 2007.

[53] A. Sangwongwanich, Y. Yang, and F. Blaabjerg, "High-Performance Constant Power Generation in Grid-Connected PV Systems," *IEEE Trans. Power Electron.*, vol. 31, no. 3, pp. 1822–1825, Mar. 2016.

[54] A. Sangwongwanich, Y. Yang, F. Blaabjerg, and H. Wang, "Benchmarking of Constant Power Generation Strategies for Single-Phase Grid-Connected Photovoltaic Systems," *IEEE Trans. Ind. Appl.*, vol. 54, no. 1, pp. 447–457, Jan. 2018.

[55] R. Tonkoski, L. A. C. Lopes, and T. H. M. El-Fouly, "Coordinated Active Power Curtailment of Grid Connected PV Inverters for Overvoltage Prevention," *IEEE Trans. Sustain. Energy*, vol. 2, no. 2, pp. 139–147, Apr. 2011.

[56] A. Sangwongwanich, Y. Yang, and F. Blaabjerg, "A Cost-Effective Power Ramp-Rate Control Strategy for Single-Phase Two-Stage Grid-Connected Photovoltaic Systems," in *Proc. 2016 IEEE ECCE*. Milwaukee, WI, USA: IEEE, Sep. 2016, pp. 1–7.

[57] X. Ai, J. Li, J. Fang, W. Yao, H. Xie, R. Cai, and J. Wen, "Multi-Time-Scale Coordinated Ramp-Rate Control for Photovoltaic Plants and Battery Energy Storage," *IET Renew. Power Gener.*, vol. 12, no. 12, pp. 1390–1397, Aug. 2018.

[58] A. Sangwongwanich, Y. Yang, F. Blaabjerg, and D. Sera, "Delta Power Control Strategy for Multistring Grid-Connected PV Inverters," *IEEE Trans. Ind. Appl.*, vol. 53, no. 4, pp. 3862–3870, Jul. 2017.

[59] P. Rodríguez, C. Citro, J. I. Candela, J. Rocabert, and A. Luna, "Flexible Grid Connection and Islanding of SPC-Based PV Power Converters," *IEEE Trans. Ind. Appl.*, vol. 54, no. 3, pp. 2690–2702, May 2018.

[60] R. K. Sarojini, K. Palanisamy, P. Sanjeevikumar, and J. B.-H. Nielsen, "Inertia Emulation Control Technique Based Frequency Control of Grid-Connected Single-Phase Rooftop Photovoltaic System with Battery and Supercapacitor," *IET Renew. Power Gener.*, vol. 14, no. 7, pp. 1156–1163, 2020.

[61] C. Verdugo, A. Tarraso, J. I. Candela, J. Rocabert, and P. Rodriguez, "Centralized Synchronous Controller based on Load Angle Regulation for Photovoltaic Power Plants," *IEEE J. Emerg. Sel. Topics Power Electron.*, 2020, early access, doi: 10.1109/JESTPE.2020.2995339.

[62] A. Hoke, E. Muljadi, and D. Maksimovic, "Real-Time Photovoltaic Plant Maximum Power Point Estimation for Use in Grid Frequency Stabilization," in *Proc. IEEE COMPEL*. Vancouver, BC, Canada: IEEE, Jul. 2015, pp. 1–7.

[63] X. Lyu, Z. Xu, J. Zhao, and K. P. Wong, "Advanced Frequency Support Strategy of Photovoltaic System Considering Changing Working Conditions," *IET Gener. Transm. Distrib.*, vol. 12, no. 2, pp. 363–370, Feb. 2018.

[64] X. Chen, Y. Du, H. Wen, L. Jiang, and W. Xiao, "Forecasting-Based Power Ramp-Rate Control Strategies for Utility-Scale PV Systems," *IEEE Trans. Ind. Electron.*, vol. 66, no. 3, pp. 1862–1871, Mar. 2019.

[65] A. F. Hoke, M. Shirazi, S. Chakraborty, E. Muljadi, and D. Maksimovic, "Rapid Active Power Control of Photovoltaic Systems for Grid Frequency Support," *IEEE J. Emerg. Sel. Top. Power Electron.*, vol. 5, no. 3, pp. 1154–1163, Sep. 2017.

[66] B. Crăciun, T. Kerekes, D. Séra, and R. Teodorescu, "Frequency Support Functions in Large PV Power Plants With Active Power Reserves," *IEEE J. Emerg. Sel. Top. Power Electron.*, vol. 2, no. 4, pp. 849–858, Dec. 2014.

[67] C. Loutan, P. Klauer, S. Chowdhury, S. Hall, M. Morjaria, V. Chadliev, N. Milam, C. Milan, and V. Gevorgian, "Demonstration of Essential Reliability Services by a 300-MW Solar Photovoltaic Power Plant," National Renewable Energy Laboratory, Golden, CO, USA, Tech. Rep. NREL/TP-5D00-67799, Mar. 2017.

[68] G. Bao, H. Tan, K. Ding, M. Ma, and N. Wang, "A Novel Photovoltaic Virtual Synchronous Generator Control Technology Without Energy Storage Systems," *Energies*, vol. 12, no. 12, p. 2240, Jun. 2019.

[69] V. Gevorgian, "Highly Accurate Method for Real-Time Active Power Reserve Estimation for Utility-Scale Photovoltaic Power Plants," National Renewable Energy Laboratory, Golden, CO, USA, Tech. Rep. NREL/TP-5D00-73207, Feb. 2019.

[70] S. I. Nanou, A. G. Papakonstantinou, and S. A. Papathanassiou, "A Generic Model of Two-Stage Grid-Connected PV Systems with Primary Frequency Response and Inertia Emulation," *Electr. Power Syst. Res.*, vol. 127, pp. 186–196, Oct. 2015.

[71] E. I. Batzelis, G. E. Kampitsis, and S. A. Papathanassiou, "Power Reserves Control for PV Systems With Real-Time MPP Estimation via Curve Fitting," *IEEE Trans. Sustain. Energy*, vol. 8, no. 3, pp. 1269–1280, Jul. 2017.

[72] C. Zhong, Y. Zhou, and G. Yan, "Power Reserve Control with Real-Time Iterative Estimation for PV System Participation in Frequency Regulation," *Int. J. Elect. Power Energy Syst*, vol. 124, p. 106367, Jan. 2021.

[73] Q. Li and M. E. Baran, "A Novel Frequency Support Control Method for PV Plants Using Tracking LQR," *IEEE Trans. Sustain. Energy*, vol. 11, no. 4, pp. 2263–2273, Oct. 2020.

[74] A. Sangwongwanich, Y. Yang, and F. Blaabjerg, "A Sensorless Power Reserve Control Strategy for Two-Stage Grid-Connected PV Systems," *IEEE Trans. Power Electron.*, vol. 32, no. 11, pp. 8559–8569, Nov. 2017.

[75] E. I. Batzelis, G. Anagnostou, I. R. Cole, T. R. Betts, and B. C. Pal, "A State-Space Dynamic Model for Photovoltaic Systems With Full Ancillary Services Support," *IEEE Trans. Sustain. Energy*, vol. 10, no. 3, pp. 1399–1409, Jul. 2019.

[76] Y. Yan, X. Yuan, and J. Hu, "Stationary-Frame Modeling of VSC Based on Current-Balancing Driven Internal Voltage Motion for Current Control Timescale Dynamic Analysis," *Energies*, vol. 11, no. 2, p. 374, 2018.

[77] N. Femia, G. Petrone, G. Spagnuolo, and M. Vitelli, *Power Electronics and Control Techniques for Maximum Energy Harvesting in Photovoltaic Systems*, 1st ed. CRC Press, Jul. 2017.

[78] H. Pang and X. Wei, "Research on Key Technology and Equipment for Zhangbei 500kV DC Grid," in *Proc. IPEC-Niigata 2018 -ECCE Asia*, May 2018, pp. 2343–2351.

[79] Y. Yang, F. Blaabjerg, and H. Wang, "Low-Voltage Ride-Through of Single-Phase Transformerless Photovoltaic Inverters," *IEEE Trans. Ind. Appl.*, vol. 50, no. 3, pp. 1942–1952, May 2014.

[80] S. Cole, J. Beerten, and R. Belmans, "Generalized Dynamic VSC MTDC Model for Power System Stability Studies," *IEEE Trans. Power Syst.*, vol. 25, no. 3, pp. 1655–1662, Aug. 2010.

[81] X. Lu, W. Xiang, W. Lin, and J. Wen, "Small-Signal Modeling of MMC Based DC Grid and Analysis of the Impact of DC Reactors on the Small-Signal Stability," *International Journal of Electrical Power & Energy Systems*, vol. 101, pp. 25–37, Oct. 2018.

[82] B. K. Poolla, S. Bolognani, and F. Dörfler, "Optimal Placement of Virtual Inertia in Power Grids," *IEEE Trans. Autom. Control*, vol. 62, no. 12, pp. 6209–6220, Dec. 2017.

[83] B. K. Poolla, D. Groß, and F. Dörfler, "Placement and Implementation of Grid-Forming and Grid-Following Virtual Inertia and Fast Frequency Response," *IEEE Trans. Power Syst.*, vol. 34, no. 4, pp. 3035–3046, Jul. 2019.

[84] J. Fu, Z. Yuan, Y. Wang, S. Xu, W. Wei, and Y. Luo, "Control Strategy of System Coordination in Nanao Multi-Terminal VSC-HVDC Project for Wind Integration," in *Proc. 2014 IEEE PES General Meeting*, Jul. 2014, pp. 1–5.

[85] T. An, G. Tang, and W. Wang, "Research and Application on Multi-Terminal and DC Grids Based on VSC-HVDC Technology in China," *High Volt.*, vol. 2, no. 1, pp. 1–10, 2017.

[86] P. Rodriguez, J. Pou, J. Bergas, J. I. Candela, R. P. Burgos, and D. Boroyevich, "Decoupled Double Synchronous Reference Frame PLL for Power Converters Control," *IEEE Trans. Power Electron.*, vol. 22, no. 2, pp. 584–592, Mar. 2007.

[87] L. Huang, H. Xin, Z. Wang, K. Wu, H. Wang, J. Hu, and C. Lu, "A Virtual Synchronous Control for Voltage-Source Converters Utilizing Dynamics of DC-Link Capacitor to Realize Self-Synchronization," *IEEE J. Emerg. Sel. Top. Power Electron.*, vol. 5, no. 4, pp. 1565–1577, Dec. 2017.

[88] C. Arghir and F. Dörfler, "The Electronic Realization of Synchronous Machines: Model Matching, Angle Tracking, and Energy Shaping Techniques," *IEEE Trans. Power Electron.*, vol. 35, no. 4, pp. 4398–4410, Apr. 2020.

[89] N. Femia, G. Petrone, G. Spagnuolo, and M. Vitelli, "Optimization of Perturb and Observe Maximum Power Point Tracking Method," *IEEE Trans. Power Electron.*, vol. 20, no. 4, pp. 963–973, Jul. 2005.

[90] U. Bussemas, B. Burger, H. Schmidt, and S. Elies, "How Fast Does an MPP Tracker Really Need To Be?" in *Proc. 24th European Photovoltaic Solar Energy Conference*, Hamburg, Germany, Sep. 2009, pp. 3273–3276.

[91] J. Alipoor, Y. Miura, and T. Ise, "Power System Stabilization Using Virtual Synchronous Generator With Alternating Moment of Inertia," *IEEE J. Emerg. Sel. Top. Power Electron.*, vol. 3, no. 2, pp. 451–458, Jun. 2015.

[92] D. Li, Q. Zhu, S. Lin, and X. Y. Bian, "A Self-Adaptive Inertia and Damping Combination Control of VSG to Support Frequency Stability," *IEEE Trans. Energy Convers.*, vol. 32, no. 1, pp. 397–398, Mar. 2017.

[93] F. Wang, L. Zhang, X. Feng, and H. Guo, "An Adaptive Control Strategy for Virtual Synchronous Generator," *IEEE Trans. Ind. Appl.*, vol. 54, no. 5, pp. 5124–5133, Sep. 2018.

[94] A. S. Mir and N. Senroy, "Self-Tuning Neural Predictive Control Scheme for Ultrabattery to Emulate a Virtual Synchronous Machine in Autonomous Power Systems," *IEEE Trans. Neural Netw. Learning Syst.*, vol. 31, no. 1, pp. 136–147, Jan. 2020.

[95] ENTSO-E, "Network Code on Load-Frequency Control and Reserves," Brussels, Belgium, Tech. Rep., Jun. 2013.

ISSN (online): 2446-1636
ISBN (online): 978-87-7210-825-4 AALBORG UNIVERSITY PRESS